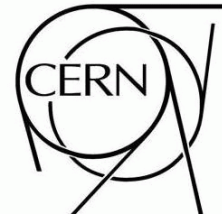




ATLAS NOTE

ATL-INDET-PUB-2008-XXX

April 2, 2008



ATLAS Pixel Detector Electronics and Sensors

The Pixel Collaboration

Abstract

The silicon pixel tracking system for the ATLAS experiment at the Large Hadron Collider is described in this paper. The performance requirements are summarized. The principal design choices for the pixel detector are presented. The design and implementation of the elements of the pixel electronics systems are described in detail. The silicon sensor design and fabrication, as well as the design, assembly and testing of pixel modules is given here. Data obtained with test beams and from cosmic rays are also described.

1 Introduction

This paper describes the pixel detector system for the ATLAS experiment at the Large Hadron Collider (LHC). ATLAS is a general purpose detector for the study of primarily proton-proton collisions at the LHC [1]. The pixel detector system is a critical component of the inner tracking detector of ATLAS [2]. The ATLAS Inner Detector provides highly efficient charged-particle track reconstruction over the pseudorapidity range $|\eta| < 2.5$. The pixel detector, with approximately 80 million channels, is essential to provide pattern recognition capability to meet the track reconstruction requirements of ATLAS at the full luminosity of the LHC of $\mathcal{L} = 10^{34} \text{ cm}^{-2}\text{s}^{-1}$. The pixel detector system is the innermost element of the Inner Detector [3]. It is the most important contributor to the identification and reconstruction of secondary vertices from the decay of, for example, particles containing a b-quark and for b-tagging of jets. In addition, it provides excellent spatial resolution for reconstructing primary vertices in the proton-proton interaction region within ATLAS even in the presence of the many multiple interactions present at the LHC design luminosity.

In the sections below we first present the performance requirements for the pixel detector. This is followed by an overview of the system and its relationship to the Inner Detector. We then describe the principal components of the pixel detector systems—electronics, sensors and modules. Results from test beam studies of the pixel components and the operation of about 10% of the pixel system using cosmic ray tracks are also presented. Mechanical systems and services are described in a separate publication [4].

2 Performance Requirements and Design Choices

The performance requirements for the ATLAS Inner Detector (ID) were formulated in the Inner Detector Technical Design Report (TDR) [2]. The pixel system is an important part of the ID and plays a major role in fulfilling these requirements.

The general performance requirements for the pixel system are:

- coverage of the pseudorapidity range $|\eta| < 2.5$;
- excellent transverse impact parameter resolution;
- good resolution on the longitudinal z -coordinate, allowing primary vertex reconstruction of charged tracks with $\sigma(z) < 1 \text{ mm}$;
- good 3D-vertexing capabilities;
- very good jet b-tagging capabilities both in the high-level trigger and in the offline reconstruction;
- minimal material for all elements of the system in order to reduce multiple scattering and secondary interactions;
- excellent efficiency for all pixel layers; and
- radiation hardness of the pixel detectors elements to operate after a total dose of 500 kGy or $10^{15} \text{ 1 MeV-neq/cm}^2$.

These performance requirements lead to the following major design choices:

- three pixel hits over the full rapidity range. The requirement to have three pixel layers has been confirmed by a detailed study comparing a layout with two pixel hits versus a layout with three pixel hits [5];
- minimal radius of the innermost layer (b-layer), set at 5 cm due to the practical limitations of clearances around the interaction region beam pipe vacuum system;

- the smallest pixel size, which is set to $50 \mu\text{m} \times 400 \mu\text{m}$ by electronics design limitations.

55 The expected dose for the innermost layer is expected to reach 500 kGy after about the first five years of LHC operation. The other layers are expected to reach the 500 kGy dose after 10 or more years of LHC operation (with maximum luminosity of $10^{34} \text{ cm}^{-2}\text{s}^{-1}$).

3 System Overview

In this section we present a brief overview of the pixel system and its relationship to the Inner Detector. 60 The basic parameters of the pixel system are also summarized in this section. The pixel detector is the innermost element of the Inner Detector as shown in Fig. 1. The pixel tracker is designed to provide at least three points on a charged track emanating from the collision region in ATLAS. The pixel detector and the other elements of the Inner Detector span a pseudorapidity range $|\eta| < 2.5$.

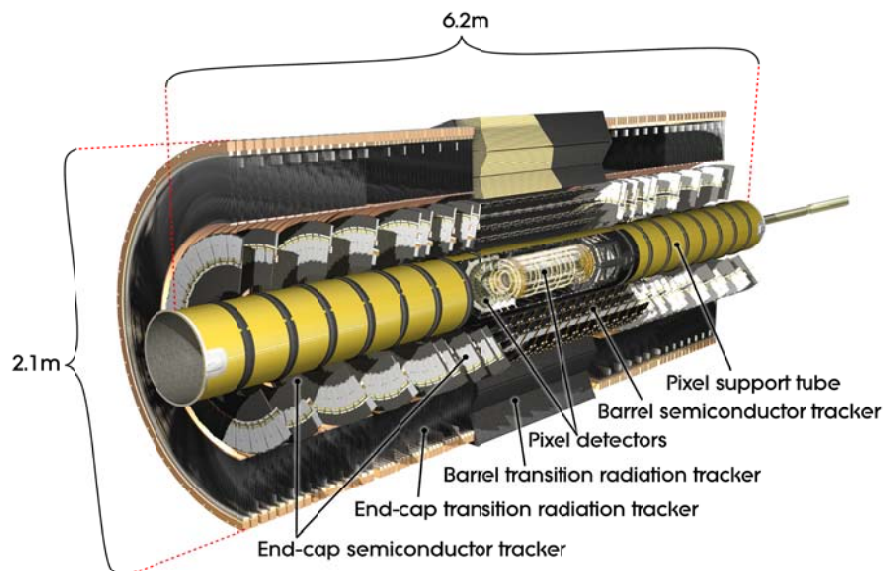


Figure 1: The ATLAS Inner Detector.

The principal components of the pixel tracking system are the following:

- 65 • the active region of the pixel detector, which is composed of three barrel layers and a total of six disk layers, three at each end of the barrel region;
- internal services (power, monitoring and cooling) and their associated mechanical support structures (also supporting the interaction region beam pipe) on both ends of the active detector region;
- 70 • a Pixel Support Tube into which the active part of the pixel detector and the services and related support structures are inserted and located; and
- external services that are connected to the internal services at the end of the Pixel Support Tube.

The active region of the pixel detector is shown in a schematic view in Fig. 2. The active part of the pixel system consists of three barrel layers—Layer 0 (so-called b-layer), Layer 1 and Layer 2—and two identical endcap regions, each with three disk layers.

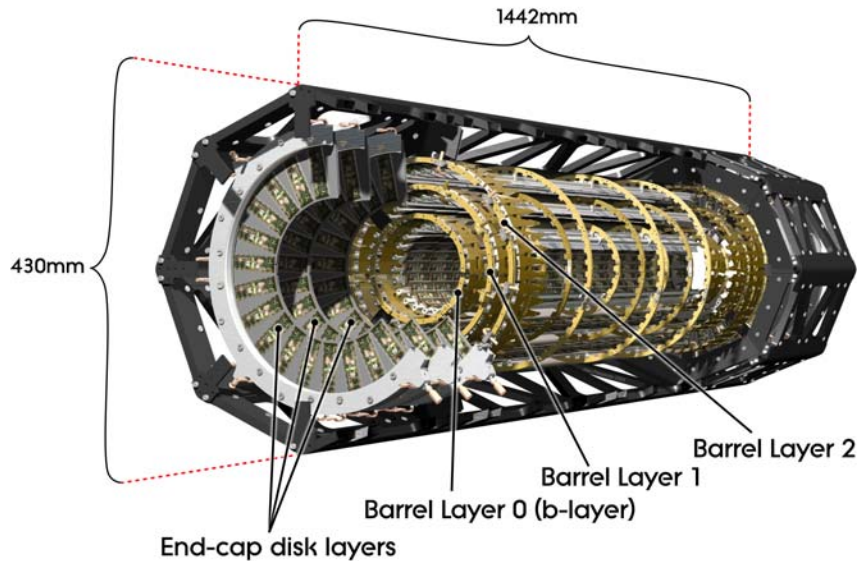


Figure 2: A schematic view of the active region of the pixel detector consisting of barrel and endcap layers.

The basic building block of the active part of the pixel detector is a module (section 6) that is composed of silicon sensors (section 5), front-end electronics and flex hybrids with control circuits (section 4). All modules are functionally identical at the sensor/integrated circuit level but differ somewhat in the interconnection schemes for barrel modules and disk modules. The pixel size is 50 microns in the ϕ direction and 400 microns in z (barrel region, along the beam axis) or r (disk region) apart from a few special pixels in the overlap region between integrated circuits on a module—see sections 5 and 6. There are 46,080 pixel electronics channels in a module.

The essential parameters for the barrel region of the pixel detector system are summarized in Table 1. Modules are mounted on mechanical/cooling supports, called staves, in the barrel region. Thirteen modules are mounted on a stave and the stave layout is identical for all layers. The active length of each barrel stave is about 801 mm. The staves are mounted in half-shells manufactured from a carbon-fiber composite material. Two half-shells are joined to form each barrel layer.

The two endcap regions are identical. Each is composed of three disk layers and each disk layer is identical. The basic parameters of the endcap region are given in Table 2. Modules are mounted on mechanical/cooling supports, called disk sectors. There are eight identical sectors in each disk.

The total number of pixels in the system is approximately 67 million in the barrel and 13 million in the endcaps, giving a total active area of about 1.7 m².

The barrel shells and the endcap disks are supported by a spaceframe also manufactured from a carbon-fiber composite material (see Fig. 2). Electrical, optical and cooling services are connected and routed within service panels (four on each end of the pixel detector) from patch panels (Patch Panel 0–PP0) at the ends of the supporting spaceframe to the end of the Pixel Support Tube. These services are supported by carbon fiber structures that also hold the beryllium vacuum pipe within the Pixel Support

Layer Number	Mean Radius (mm)	Number of Staves	Number of Modules	Number of Pixels	Active Area (m ²)
0	50.5	22	286	13,178,880	0.28
1	88.5	38	494	22,763,520	0.49
2	122.5	52	676	31,150,080	0.67
TOTALS		112	1456	67,092,480	1.45

Table 1: Basic parameters of the barrel region of the ATLAS pixel detector system.

Disk Number	Mean z (mm)	Number of Sectors	Number of Modules	Number of Pixels	Active Area (m ²)
0	495	8	48	2,211,840	0.0475
1	580	8	48	2,211,840	0.0475
2	650	8	48	2,211,840	0.0475
TOTAL ONE ENDCAP		24	144	6,635,520	0.14
TOTAL BOTH ENDCAPS		48	288	13,271,040	0.28

Table 2: Basic parameters of the endcap region of the ATLAS pixel detector system.

Tube. Electrical, optical and cooling connections are made at the end of the Pixel Support Tube at Patch Panel 1 (PP1). Connections and control of external services are made at additional patch panels (PP2, PP3 and PP4) located within the ATLAS detector or near the ATLAS control room complex. The principal sub-elements of the pixel detector — barrels, endcaps, service supports and eight service panels — were assembled in a surface building near the ATLAS underground cavern. The complete pixel detector with its services was tested in part and then installed as a unit into the Inner Detector. The mechanics, services and assembly of the pixel detector are described in detail in Ref. [4].

The contribution of the Pixel Detector to the total Inner Detector material budget as a function of pseudorapidity is shown in Fig. 3 (radiation lengths) and Fig. 4 (interaction lengths). The beam pipe contribution is also presented.

4 Electronics Systems

4.1 Overview

The first comprehensive proposal of the pixel electronic system was described in 1997-98 in the ATLAS Inner Detector and Pixel Detector Technical Design Reports [2, 3]. The complete system underwent several revisions in the subsequent years. The required radiation tolerance is 500 kGy, corresponding to at least 10 years of operation at the design LHC luminosity of $10^{34} \text{ cm}^{-2}\text{s}^{-1}$ for the external layers and three years of operation for the innermost layer (b-layer). The total number of instrumented channels is about 80 million, each containing approximately 1,000 transistors and consuming a maximum power of 100 μW (power for on-detector circuitry only).

4.1.1 System Architecture

A block diagram that illustrates the principal elements of the system architecture is shown in Fig. 5.

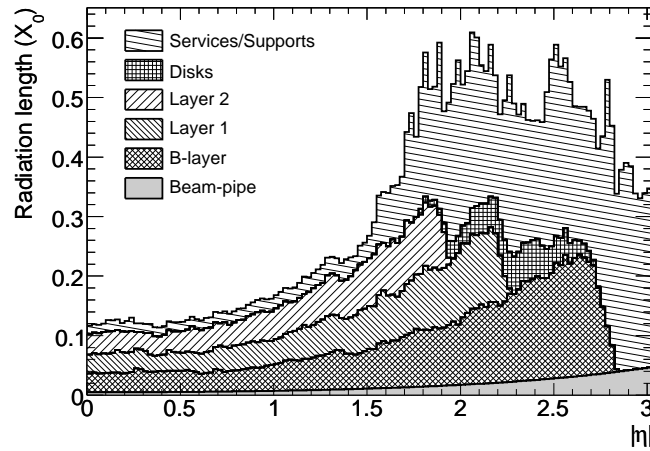


Figure 3: Radiation length of the pixel detector showing the contribution from each layer and from all disks. Layer and disk contributions include services and supports directly in front of and behind of the layer/disk. All remaining services and supports, including services in the region between the barrel and endcap are included in the "Services/Supports" category.

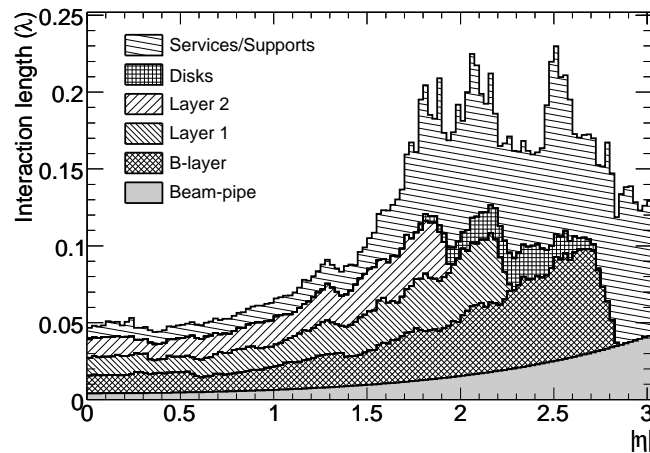


Figure 4: Interaction length of the pixel detector showing the contribution from each layer and from all disks. Layer and disk contributions include services and supports directly in front of and behind of the layer/disk. All remaining services and supports, including services in the region between the barrel and endcap are included in the "Services/Supports" category.

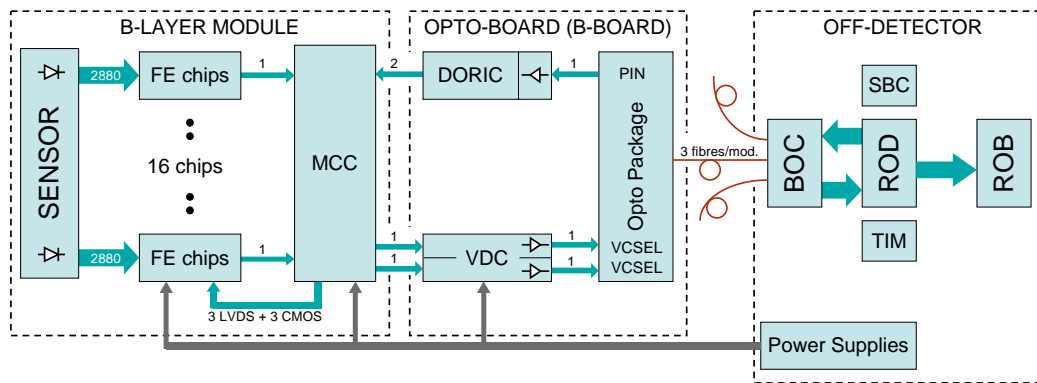


Figure 5: Block diagram of the pixel detector System Architecture.

120 Charge released by ionizing particles in the cells of the sensor array are collected by 16 front-end
 chips (FE) per module, arranged in two rows of eight chips. The 16 FEs are read out by a Module Control
 Chip (MCC). Data are transmitted from the FE to the MCC using Low Voltage Differential Signalling
 (LVDS) serial links, configured in a serial star topology. The serial protocol minimises the number
 125 of lines to be routed, while the star topology maximizes bandwidth and reliability. Each module is then
 connected to the off-detector Read-out Drivers (RODs) through optical-fiber links(opto-links). One down
 link is used to transmit clock, trigger, commands and configuration data, while one or two up-links are
 used for event readout. The b-layer uses two up-links to increase the aggregate bandwidth needed for
 the higher average hit occupancy at the minimum radius. The readout (R/O) architecture is "data-push".
 This means that each component in the chain (FE, MCC) always transmits at the maximum rate and
 130 there is no busy mechanism to stop transmission when buffers are full. Each upstream component in
 the R/O chain (MCC, ROD) constantly monitors the number of events received and compares the results
 with the number of triggers sent. If the difference of the two is bigger than a predefined value, triggers
 downstream are blocked and empty events are generated.

135 The power supply system uses commercial components, adapted to the requirements of the pixel
 detector, for the low (electronics) and high (sensor bias) voltages. The use of deep sub-micron electronics
 and long resistive cables with significant voltage drops, required the use of low-voltage regulator boards,
 approximately 10 meters from the pixel detector. The maximum voltage rating for the pixel electronics is
 4 V. To interface between the electrical and the optical sides of the opto-links, special receiver and driver
 chips (DORIC and VDC) have been implemented. An optical-interface card (Back of Crate or BOC) is
 140 also used for each ROD.

4.2 Front-end Chip

4.2.1 Front-end Chip History

145 Small scale, front-end chips that demonstrated the required analog and digital architecture were first
 developed in the second half of the 1990s ([6], [7], [8,9] and [6,10]). The first radiation-soft functional
 prototypes of full-size chips were submitted in 1998: FE-B and FE-A/C (Pirate). The FE-B chip was
 designed using 0.8 μm CMOS technology and had the same basic readout architecture used for the
 final chips. The FE-B charge amplifier used a direct cascode¹⁾ and source follower, with a feedback
 capacitance of 4 fF. The DC feedback was based on a previous design [8,9]. The discriminator used a
 dual threshold, with a low threshold for precise timing and a high threshold to flag a hit pixel.

¹⁾The cascode is a two-stage amplifier composed of a transconductance amplifier followed by a current buffer.

FE-A was made in $0.8\mu\text{m}$ BiCMOS technology, whereas FE-C was a full CMOS version. The charge amplifier used a folded cascode input stage with feedback capacitance of 3 fF and a new, improved DC feedback. The discriminator was AC coupled, with an input, fully-differential, bipolar pair in the A-version and CMOS in the C-version. The column readout architecture used a shift register to transport the hit address to the bottom of the chip. Hits are associated with the level 1 trigger (L1) by counting the number of clock cycles needed for the hit to reach the bottom of the column. FE-A/B/C demonstrated all the basic ATLAS pixel performance goals in the laboratory and in beam.

The subsequent chip was developed using the basic concept of the amplifier/discriminator from FE-A/C and the column readout architecture from FE-C. The European and US front-end design teams joined forces to combine all of the experience gained with radiation-soft chips into a common layout for the DMILL²⁾- Durci Mixte sur Isolant Logico-Lineaire - technology (known as FE-D). FE-D1 was submitted in July 1999 together with the DORIC and VDC chips (see section 4.4) and a prototype MCC-D0 (see section 4.3). A new production run was submitted in Aug 2000 with two versions of FE-D2: one with dynamic and the other with static memory cells. This run included the full MCC-D2 and new DORIC and VDC chips as well. Yields of both FE and MCC were unacceptable and work with this vendor was terminated. Work in an alternative radiation-hard technology, FE-H, began in Dec 1999 [11]. The chip was almost ready but was never submitted also because of large cost increases. The failure of both traditional radiation-hard vendors left the collaboration with the Deep Sub-micron (DSM) approach, based on commercial process $0.25\mu\text{m}$ CMOS process and a radiation-tolerant layout. A major design effort was initiated in September 2000. Three versions (FE-I1, FE-I2 and FE-I3) were eventually produced. The final chip (FE-I3) became available in late 2003. Table 3 gives a summary of the front-end designs developed for the ATLAS pixel detector.

Chip	Year	Cell size (μm^2)	Col \times Row	Transis- tors	Technology	References
Beer & Pastis	1996	50×436	12×63	–	AMS $0.8\mu\text{m}$ BiCMOS, 2M	[6, 10]
M72b	1997	50×536	12×64	–	HP $0.8\mu\text{m}$ CMOS, 2M	[6]
Marebo	1997	50×397	12×63	0.1 M	DMILL $0.8\mu\text{m}$ BiCMOS, 2M	[8, 9]
FE-B	1998	50×400	18×160	0.8 M	HP $0.8\mu\text{m}$ CMOS, 2M	[11–13]
FE-A/C	1998	50×400	18×160	0.8 M	AMS $0.8\mu\text{m}$ BiCMOS, 2M	[10, 13]
FE-D1	1999	50×400	18×160	0.8 M	DMILL $0.8\mu\text{m}$ BiCMOS, 2M	[13]
FE-D2	2000	50×400	18×160	0.8 M	DMILL $0.8\mu\text{m}$ BiCMOS, 2M	–
FE-I1	2002	50×400	18×160	2.5 M	DSM $0.25\mu\text{m}$ CMOS, 6M	[14]
FE-I2/I2.1	2003	50×400	18×160	3.5 M	DSM $0.25\mu\text{m}$ CMOS, 6M	[15]
FE-I3	2003	50×400	18×160	3.5 M	DSM $0.25\mu\text{m}$ CMOS, 6M	[16–19]

Table 3: Summary of the ATLAS pixel front-end chips as described in the text.

4.2.2 Design

Chip Architecture The readout chip for the ATLAS pixel detector [16, 17], shown in Fig. 6, contains 2880 pixel cells of $50 \times 400\mu\text{m}^2$ size arranged in an 18×160 matrix. Each pixel cell contains an analogue block where the sensor charge signal is amplified and compared to a programmable threshold using a comparator. The digital readout part transfers the hit pixel address, a hit leading edge (LE) timestamp, and a trailing edge (TE) timestamp to the buffers at the chip periphery. In these buffers a Time-over-Threshold (ToT) is calculated by subtracting the TE from the LE timestamp. These hit-buffers monitor the time of each stored hit by inspecting the LE time stamp. When a hit time becomes

²⁾DMILL technology was developed by CEA, France, and then produced under license by TEMIC Matra MHS.

180 longer than the latency of the L1 trigger ($3.2 \mu\text{s}$) and no trigger signal is recorded, the hit information is deleted. Hits marked by trigger signals are selected for readout. Triggered hit data are then transmitted serially out of the chip in the same order as the trigger arrival.

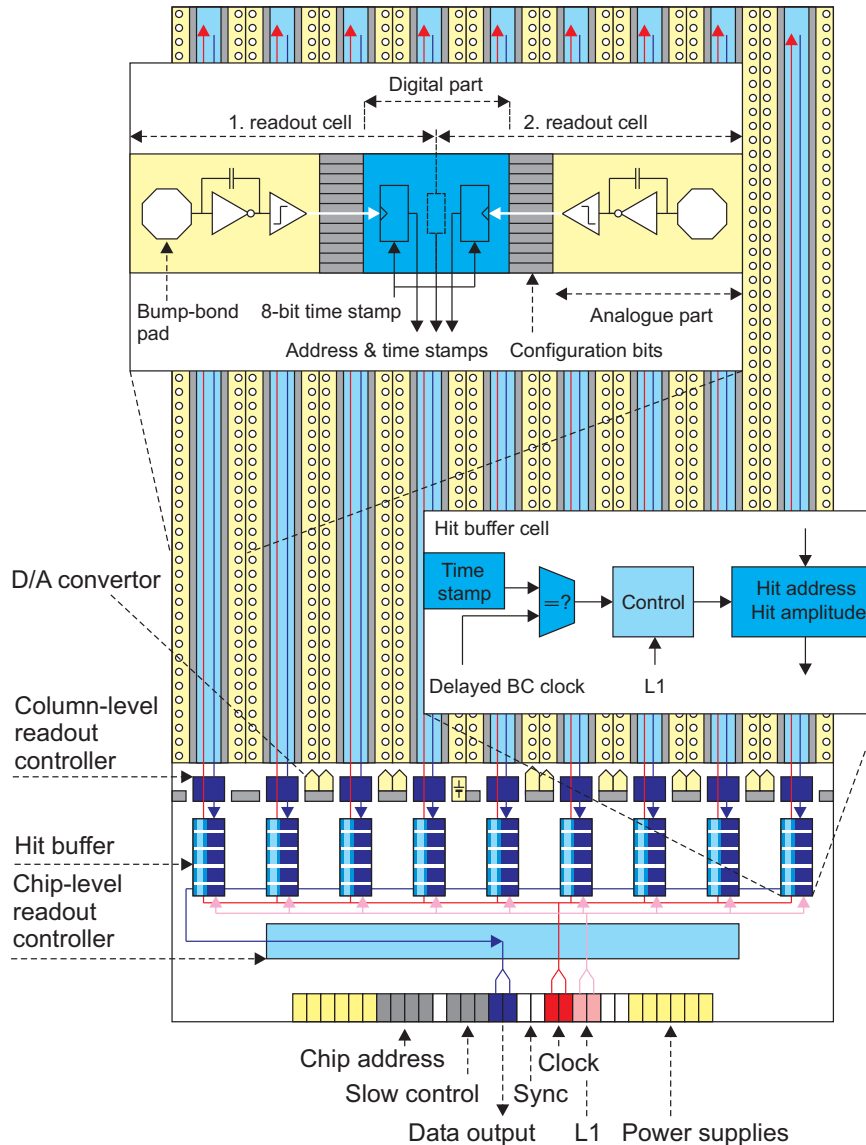


Figure 6: Floor plan of the front-end chip (FE-I3) with main functional elements.

Charge Sensitive Preamplifier The charge-sensitive amplifier uses a single-ended, folded-cascode topology, which is a common choice for low-voltage and high gain amplifiers. The amplifier is optimised for a nominal capacitive load of 400 fF and designed for the negative signals expected from n^+ -on- n -bulk detectors. The design of the charge amplifier was particularly influenced by requirements pertaining to sensor irradiation, which can produce leakage currents up to 100 nA. The preamplifier has a 5 fF DC feedback, a 15 ns risetime and operates at about 8 mA bias. Since the input is DC-coupled, a compensation circuit is implemented that drains the leakage current and prevents it from influencing the bias current of the fast feedback circuit, used to discharge the feedback capacitor. The feedback system,

185

190

shown in Fig. 7, uses two PMOS devices, one (M2) providing leakage current compensation and the other (M1) continuously resetting the feedback capacitor.

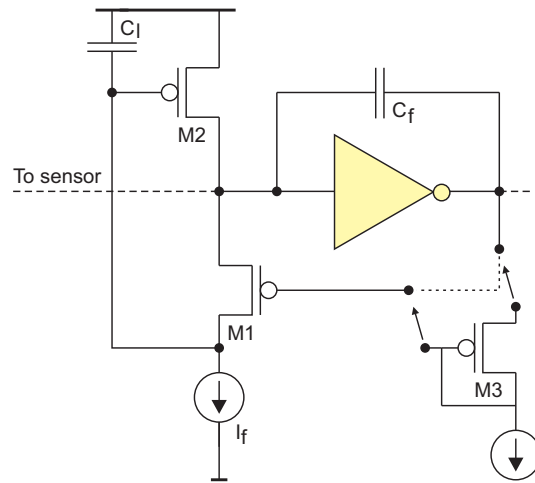


Figure 7: Charge preamplifier feedback circuit.

An important property of this feedback circuit is that the discharge current provided by the reset device saturates for high-output-signal amplitudes. The return to baseline is therefore nearly linear and a pulse width proportional to the input charge is obtained. The width of the discriminator output, Time-over-Threshold, can therefore be used to measure the signal amplitude. The duration of the ToT is measured by counting the cycles of the 40 MHz master chip clock. The feedback current is 4 nA for a 1 μ s return to baseline for a 20,000 electron-equivalent input. The feedback circuit has an additional diode-connected transistor M3, which acts as a level shifter so that the DC-levels of input and output nodes are nearly equal. It also simplifies the DC-coupling between amplifier and the comparator, described below.

Comparator Signal discrimination is made by a two-stage circuit: a fully differential, low-gain amplifier, where threshold control operates by modifying the input offset, and a DC-coupled, differential comparator. The first stage has a bias of about 4 μ A whereas the second uses a current of about 5 μ A. A local threshold generator is integrated in every pixel in order to make the threshold independent of the local digital supply voltage in each pixel and on the amplifier bias current I_f . Seven-bits are used in each pixel to adjust the discriminator threshold.

Pixel Cell Control Logic A complete block diagram of the analogue part with several additional circuit blocks is shown in Fig. 8. Each pixel has several parameters that can be tuned through a 14-bit control register. These bits are:

- *FDAC 0-2*: 3-bits to trim the feedback (I_f) current for tuning the ToT response.
- *TDAC 0-6*: 7-bits to trim the threshold in each pixel.
- *MASK*: the digital output of the analogue part can be switched off locally by setting this bit.
- *EnHitBus*: the digital outputs of all readout channels can be directly observed using a wired OR which is locally enabled with this bit. This bit also controls, through transistor M2b, the summing of a current proportional to the feedback plus leakage current in the preamplifier, allowing for monitoring of the feedback current and of the leakage current from the sensor.

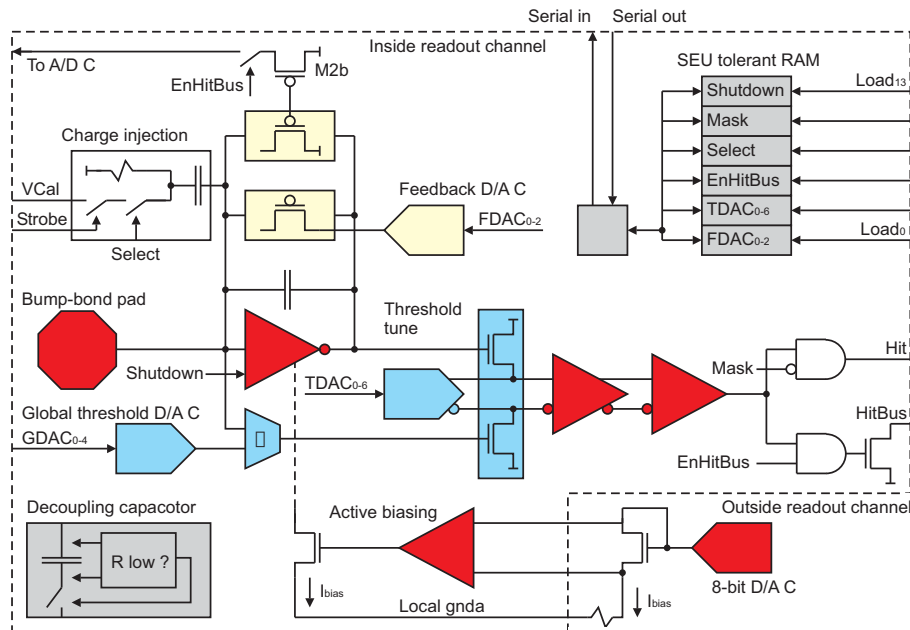


Figure 8: Pixel cell block diagram.

- *Select*: enables the pixel for test charge injection. The amplitude is generated from V_{Cal} (voltage proportional to the injected calibration charge) whereas the timing comes from an external *Strobe* signal.
- *Shutdown*: disables the charge amplifier so that no output is generated from the pixel.

220

Pixel Cell Readout Logic A block diagram of the column-pair readout is shown in Fig. 9. LE and TE timestamps are temporarily stored in local memories before being transferred to the hit-buffers at the chip periphery. A digital circuit generates two short ($1ns$) strobes at the LE and TE comparator edges. These signals are used to store the 8-bit Gray-coded time stamp into two memories. The time stamps, generated at the chip periphery, running at 40 MHz, are distributed differentially in order to decrease the digital crosstalk to analogue circuits and sensor electrodes. The complete hit information is available after the TE of the comparator signal and data transfer start. The time stamp of the LE (8-bits), of the TE (8-bits) and the row number (8-bits) are transferred to the end-of-column (EoC) buffers. Transfer happens by a priority mechanism that selects cells with data starting from the top row. The top most cell with a hit transfers its data to the bus and all the cells below it are inhibited. When the cell is read out, it releases the priority encoder bus and subsequent hits are selected and put on the readout bus. The readout speed is limited by the time the priority logic needs to ripple down. Hits can ripple through at a programmable speed that is obtained from the 40 MHz clock division. The maximum speed to transfer a single hit to the EoC is 20 MHz.

225

230

235

Column Readout Controller The readout is column based, and two columns are read out from the same controller. The first task of the controller is the generation of the readout sequence to transfer hit information: LE and TE timestamps, and the pixel-row address into an EoC buffer. This operation begins when data is complete, which is after the TE discriminator is activated. The transfer of hits from a column pair is synchronized by the Controller end-of-Column Unit (CEU), which operates at a speed of 5, 10, or 20 MHz. A total of 64 hit buffers are available for each double-column. The second task

240

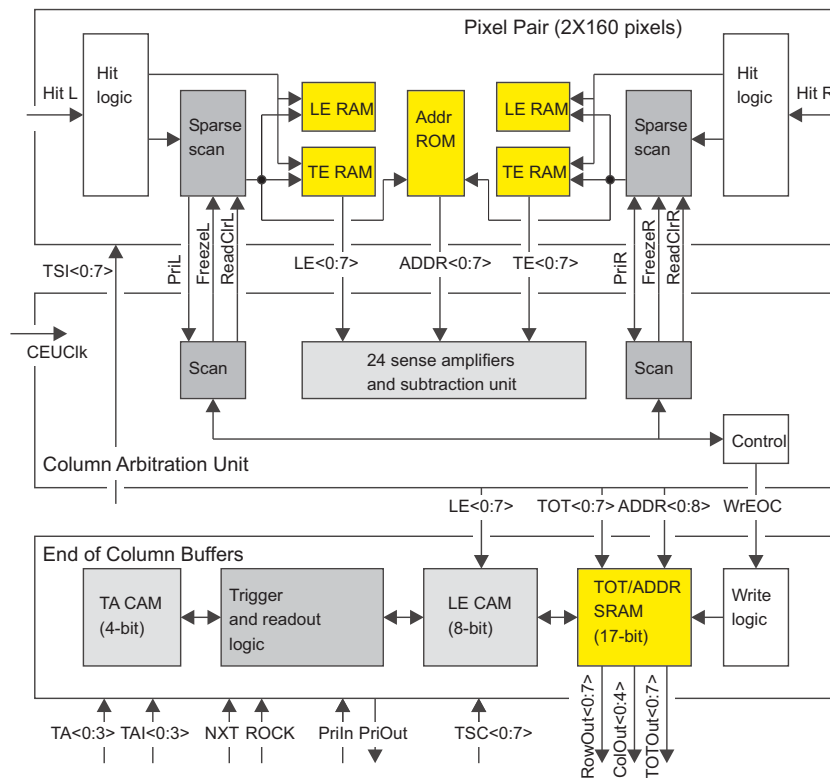


Figure 9: Block diagram of the column-pair readout.

involves digital processing of the hit data. Hit information is formatted by the CEU. Formatting includes the ToT calculation: subtraction of a TE time stamp from a LE timestamp. Optionally, a digital threshold may be applied to the ToT, and a timewalk (time slewing for small charges with respect to high charge) correction may be applied (write a hit twice if below correction threshold, once with LE and once with LE – 1), or both. These operations are pipelined to minimize deadtime, but the EoC writes cannot occur faster than 20 MHz. Hit information is written to the EoC buffer, and waits there for a corresponding L1 trigger. If a trigger arrives at the correct time, and corresponds to the LE time stamp for the hit, the hit is flagged as belonging to a particular 4-bit trigger number. Otherwise, it is reset and the buffer is freed. Once the chip has received L1 triggers, the trigger FIFO will no longer be empty. This initiates a readout sequence in which the EoC buffers are scanned for the presence of hits belonging to a particular trigger number. If hits are found, they are sent to the output serializer block, which encodes and transmits them to the Module Controller Chip (MCC). After all hits for a given trigger number have been sent, an End-of-Event (EoE) word is appended to the data stream. All of these operations occur concurrently and without deadtime, with all column pairs operating independently and in parallel.

Event readout from the EoC buffers happens concurrently with the column readout. When the chip-level readout controller starts processing a particular L1 event, it first broadcasts the corresponding L1 readout address to all buffers. All cells with hits waiting for readout compare their stored L1 address with the request value. The readout of the selected L1 hits is controlled by a priority network, which sorts them in column and row order.

Chip Level Readout Controller The chip-level readout controller collects hit data from the EoC buffers and transmits the results off the chip serially. All hits belonging to the same L1 are grouped

together into a single event, and events are transmitted out of the chip in consecutive trigger order. When a L1 trigger arrives, the current bunch-crossing time and a buffer-overflow bit are stored in a FIFO memory, which has a depth of 16 locations. This allows the chip to keep track of 16 pending L1 signals. The write-pointer of the FIFO is used as the L1 identification, which is sent to the hit buffers. The readout sequence is started as soon as the FIFO receives an L1 trigger. If the L1 priority scan in the hit buffers flags cells with matching trigger numbers, the data of the first cell in the hierarchy is sent to a global data bus, where the information is copied to a shift register. The content of the shift register is then transmitted serially. This is repeated until the priority scan shows no more hits. An End-of-Event data word, which includes error flags, is then added to the event.

Chip Configuration FE-I3 has 231 global configuration bits plus 14 local bits for each of the 2880 readout channels. The global bits are the settings for eleven 8-bit bias-current DACs, for one 10-bit calibration voltage DAC, for the global threshold bits, for the L1 latency, for the ToT filter thresholds, for column-enable bits, as well as for others. The configuration is loaded into the chip using a serial protocol running at 5 MHz. This protocol uses three chip input pads: a data input, a clock and a load. Each write operation begins with a 4-bit address, which permits the 16 chips in a module to receive independent configurations. The address of each chip is encoded with wire bonds during module assembly.

4.2.3 Requirements, Performance and Production

The design requirements for the pixel front-end electronics come from operation at high radiation doses, from the time resolution of 25 ns to separate two contiguous bunch crossings, from noise, from the minimum operation threshold and dispersion and from the overall power budget. The calibration relies on a 7-bit adjustment of individual pixel thresholds (tuning). The untuned (tuned) threshold dispersion σ is 800 (70) electrons equivalent-input charge (e). The noise is 160 e and the typical operating threshold is 4000 e , which results in hits with signals $> 5500 e$ appearing in the correct 25 ns time bucket (described as in-time threshold) [18, 19]. Neither the dispersion nor the noise depends on the choice of threshold. The tuned thresholds have been observed to re-disperse with moderate radiation dose in prototypes, and it is expected that periodic threshold re-tuning will be needed. However, the actual dispersion rate in the real operating environment will need to be measured. A selectable option internally duplicates near-threshold hits in two adjacent time buckets in order to allow recovery of in-time threshold inefficiencies. Measurements made on a few modules irradiated to 600 kGy show a negligible tuned threshold dispersion and a 20% increase in the noise, despite the very high induced sensor leakage current (60 nA for normal pixels). For a configured chip, the typical digital current is 45 mA at 2 V and the analogue current is 75 mA at 1.6 V for a total power of 220 mW.

Chip production was made in batches of 48 wafers. There are 288 chips on each 12-inch wafer. Six production batches were purchased along with the six wafers from an engineering production run. The average wafer-probing yield was about 80%. The ATLAS pixel detector contains a total of 27904 front-end chips.

4.3 Module Control Chip (MCC)

4.3.1 MCC History

The prototype sequence leading up to the Module Controller Chip (MCC) is shown in Table 4. The very first version of the chip, submitted in 1998, was fabricated in a radiation-soft process using 0.8 μm CMOS technology [20]. This chip was extensively used when building radiation-soft modules. The technology was chosen as it was very close to the 0.8 μm BiCMOS DMILL technology which, at the time, was the chosen radiation-hard technology for the ATLAS pixel detector.

Chip	Year	Std.Cells	Transistors	Chip size (mm^2)	Technology
MCC-AMS	Apr 1998	17922	363 000	10.3×6.3	AMS $0.8\mu m$ CMOS, 2M
MCC-D0	Aug 1999	–	–	6.1×3.5	DMILL $0.8\mu m$ BiCMOS 2M
MCC-D2	Aug 2000	13446	328 000	11.9×8.4	DMILL $0.8\mu m$ BiCMOS, 2M
MCC-I1	Nov 2001	33210	650 000	6.38×3.98	DSM $0.25\mu m$ CMOS, 5M
MCC-I2	Feb 2003	67919	880 000	6.84×5.14	DSM $0.25\mu m$ CMOS, 5M
MCC-I2.1	2003	67919	880 000	6.84×5.14	DSM $0.25\mu m$ CMOS, 5M

Table 4: Summary of the ATLAS pixel MCC chips.

305 A first prototype of the rad-hard chip (MCC-D0) was built in 1999. It contained only one Receiver, but all the remaining circuitry was implemented thereby providing a good test of the DMILL technology. The final version of the chip (MCC-D2) was submitted in Aug 2000. The chip worked fine but had an unacceptably low yield, for both MCC-D2 and FE-D2. Consequently, this technology was abandoned.

310 At this point in time, the MCC was ported to the DSM $0.25\mu m$ CMOS technology, and the MCC-I1 chip was submitted in November 2001. A new version of the chip, MCC-I2, was made in 2003 in order to provide better Single Event Upset (SEU) hardening to the chip. It turned out that this chip had a small error that could be corrected by modifying only one metal line. Six additional wafers, containing the correction in the layout, were produced in 2003 leading to the final MCC-I2.1 chip.

4.3.2 Design

315 This section briefly describes the actual implementation of the production MCC chip, labeled MCC-I2.1. A simplified block diagram of the MCC internal architecture is shown in Fig. 10. The MCC has three main system tasks: (1) loading parameter and configuration data into the FEs and into the MCC itself; (2) distributing timing signals such as bunch-crossing, L1 trigger and resets; and (3) reading out the FE chip and event building.

320 **System Configuration** The FE chips and the MCC must be configured after power-up or before starting a data-taking run. It is possible to write and read to all the MCC registers and FIFOs. This is used to configure, to read status information or to test the functionality of the chip. For this last function we provide a special set of commands that allows one to write simulated events into the FIFOs and to run the Event Builder with the stored values in order to check the complete functionality of the chip. Once the
325 MCC is embedded in the pixel detector, it will be important to test whether the event building works with known simulated events. Global FE chip registers and parameters in each of the pixel cells are written and read back through the MCC.

Trigger, Reset and Timing The second task of the MCC is the distribution of L1 triggers, resets and calibration/timing signals for the FE chips. In *Data Taking* mode, each time a L1 trigger command is
330 received by the MCC, the Trigger, Timing & Control (TTC) logic issues a trigger to the FEs, as long as there are less than 16 events still to be processed. In case of an overflow, the L1 trigger is not generated by the MCC and the corresponding event is lost. The information is sent to the ROD together with the number of missing events in order to keep up with event synchronisation. In addition to the triggers, the TTC logic generates a hierarchy of reset signals that can be applied either to the MCC or to one or more
335 FE's. The last function of the TTC logic is the ability to issue calibration strobes to the FEs. This is used to calibrate the FE analogue cells on a pixel-by-pixel basis.

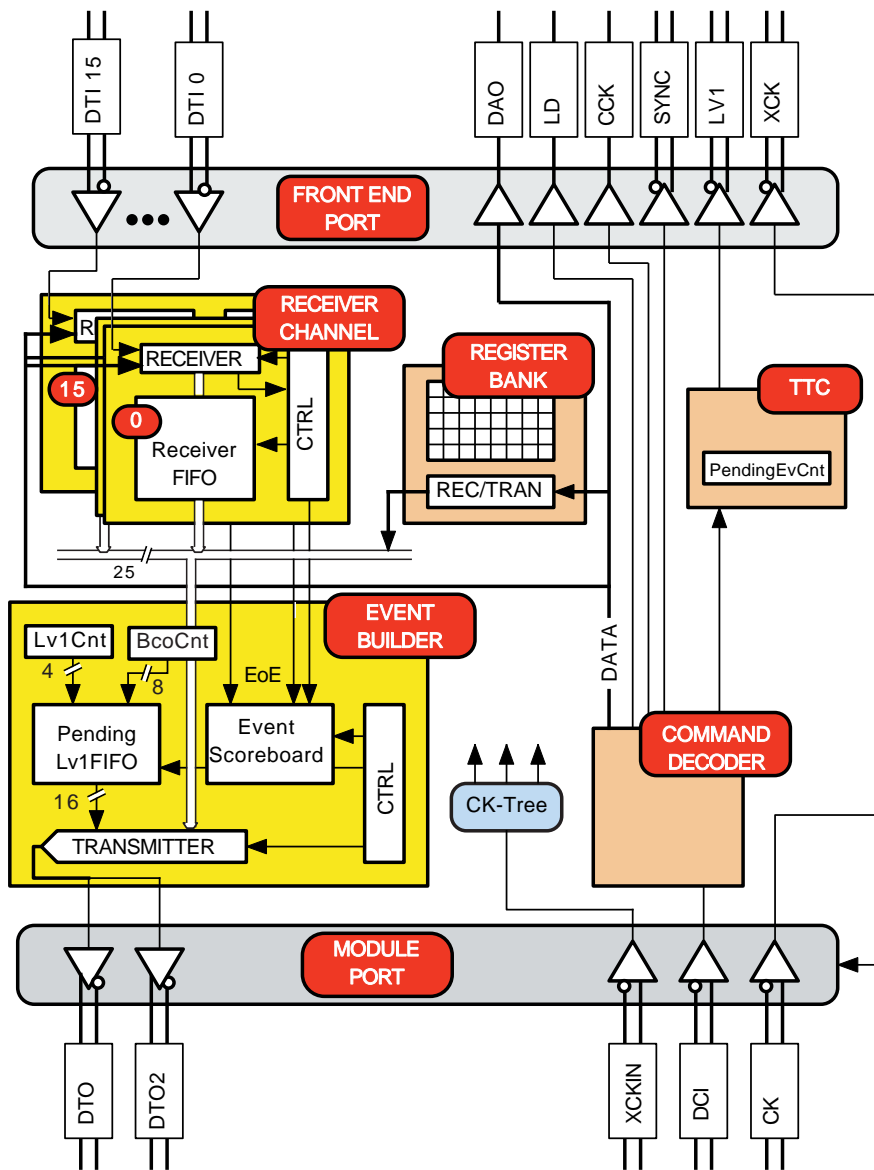


Figure 10: Module Control Chip block diagram.

Event building The read-out logic that was chosen for the pixel detector is a data-push architecture with two levels of buffering: EoC buffers in the FE chips and 16 individual 128×27 -bit deep FIFOs (ReceiverFIFO) at the MCC inputs.

340 Event readout and building is by far the most complicated task and it occupies most of the chip area. Data received from the FEs, in response to a L1 trigger, are deserialised and buffered in 16 FIFOs, one FIFO for each receiving FE line. These FIFOs are used to derandomise the 16 data flows from the FEs and are used by the event builder to extract ordered hits and to prepare them for transmission out of the pixel module. Event building is performed by two concurrent processes running in the MCC. The
345 first (Receiver) deals with filling the 16 input FIFOs with data received from the corresponding FE chip, while the second (Event Builder) extracts data from the FIFOs and builds up the event. Each FE sends data as soon as they are available with two constraints. Event hits must be ordered by event number and for each event an end-of-event (EoE) word is generated. The EoE is also sent for the case of an empty event to maintain the event synchronisation.

350 The event transmitted to the ROD is organized by the Event Builder process on an event-by-event basis, instead of a hit-by-hit basis. If the FIFO becomes full while storing incoming hits, all subsequent hits are discarded and only the EoE word is written into the FIFO. In this case, a truncated event flag will be stored in the ReceiverFIFO and then recorded to the MCC output data stream. The mechanism ensures that reconstructed events are not corrupted by FIFO overflows.

355 As soon as the Event Builder finds that an event is completely received from all of the 16 FEs, it starts building up and transmitting the event. The Event Builder learns from the Scoreboard when the events are complete. The first information written to the output data stream is the bunch crossing identifier (BCID) and the L1 identifier (L1ID). At this point the Event Builder starts fetching data from the ReceiverFIFOs, until it finds an EoE in the data. Once the Event is finished, a Trailer word is sent out to inform the ROD
360 that the Event has ended.

I/O Protocols Several serial protocols were defined for communication to/from the ROD/MCC and the MCC/FE. All protocols that are active during data taking use only LVDS type signals, whereas signals used during configuration use single-ended CMOS to reduce the number of interconnection lines. Communications from the ROD to the MCC use a 40 Mb/s data line (Data Command Input - DCI)
365 validated by the rising edge of the 40 MHz clock (CK).

The MCC to ROD link may use 40, 80 or 160 Mb/s data rates. For the case of 40 Mb/s, a new bit is transmitted at every rising edge of the CK. For the 80 Mb/s, bits are sent at both clock transitions. Finally for 160 Mb/s, both lines and clock edges are used. This can be considered as a 2-bit wide serial link. Only the event readout uses the two higher bit rates. Readout of configuration data is always at 40
370 Mb/s. The robustness of data passing from the MCC to the ROD is improved by providing a bit-flip-safe Header and by adding synchronisation bits after a known numbers of clock cycles.

Communications from the MCC to the FE chips are accomplished using a serial CMOS data bus (Data Address Output - DAO), a CMOS control line (Load - LD) and a 5 MHz validation CMOS clock (Control Clock - CCK). Both configuration and event data from the FE to the MCC are transmitted using
375 16 individual LVDS serial links (Data Input - DTI).

Special care is needed in the implementation of the Data-Taking protocols in order to minimize the effect of possible Single Event Upset events. In particular, while in data taking mode, there are only two possible 5-bit commands: 'trigger' and 'exit data-taking modes'. All permutations of the trigger command, obtained by flipping one single bit, are also interpreted as a trigger command with the correct
380 timing.

4.3.3 Requirements, Performance and Production

The design requirements include operation at high radiation dose, time resolution of 25 ns separating two contiguous bunch crossings, the expected bandwidths at the highest luminosity, the L1 trigger rate of 100 kHz and the number of FE chips that are controlled in a module.

385 The 16 FIFO's in the MCC were designed to handle the expected data rate of the FE chips operating at full luminosity with a L1 trigger rate of 100 kHz. In addition, the circuit were designed to be robust against a Single Event Upset. This problem was addressed using either triple redundancy majority logic or error detection and correction schemes. Several modules were irradiated up to (and in some cases beyond) the full LHC-lifetime dose, continuously reading out the data during irradiation. From these
390 SEU studies, we expect stable operation at the LHC without a significant loss in the configuration data coming from bit-flips in the memory elements.

For a configured chip, the typical digital current is 145 mA at 2.0 V and at a clock frequency of 40 MHz, the total power is 290 mW. All MCC-I2.1 chips were produced in a single batch of six wafers. The number of potentially good chips per wafer is 536. The measured yield was of 83%, providing a
395 total of 2666 good chips. A total of 1744 chips are used in the ATLAS pixel detector.

4.4 Optical Communication

4.4.1 Optical Link Architecture

The communication between the detector modules and the off-detector electronics is via optical links. The opto-links were selected to implement electrical decoupling and to minimize the material budget.
400 The architecture was inherited from the ATLAS SCT [21]. Modifications where made to adapt to the data-rates, modularities and radiation hardness needs of the pixel detector.

A block diagram of the optical-link system architecture is shown in Fig. 11. The two main com-

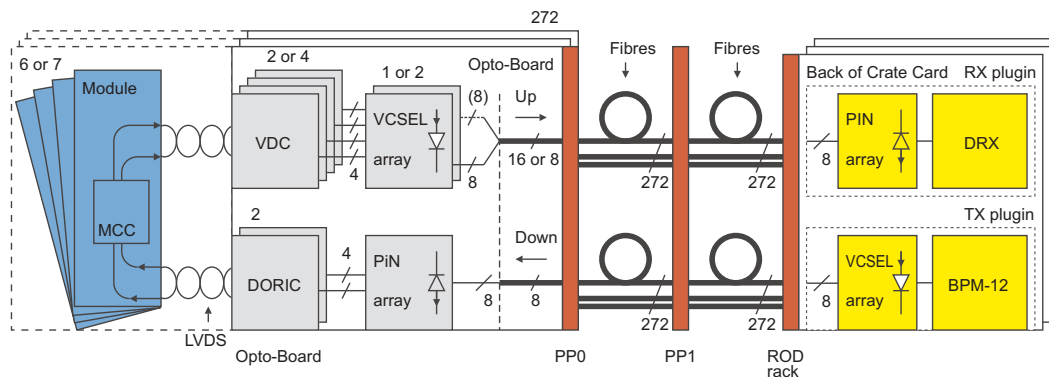


Figure 11: Optical-link system architecture.

ponents in the optical-link system are the opto-board, on the detector side, and the Back of Crate Card (BOC), on the off-detector end. To keep the material budget low, to accommodate fiber routing requirements, to control radiation exposure, and to permit the use of optical arrays, the opto-components and the related receiver/driver IC's were not implemented on the detector modules. The components have
405 been put instead on the opto-boards at Patch Panel 0 (PP0), at a distance of up to about one meter from the modules and at relatively large radius of about 200 mm inside the Pixel Support Tube.

The transmission of the signals from the detector modules to the opto-boards uses LVDS electrical connections. These serial connections link the MCC with the VCSEL Driver Chip (VDC) and the Digital
410

Optical Receiver IC (DORIC) sited on the opto-boards. The DORIC and VDC designs were derived from the SCT project, but have been adapted to survive the higher radiation dose expected in the pixel detector. These chips have been fabricated on the same silicon wafers used to produce the MCC chips.

415 The communication with each detector module uses individual fibres: one for down-link and one or
two for up-links. Trigger, clock, commands and configuration data travel on the down-link, while event
data and configuration read-back data travel on the up-link(s). On the down-link, a bi-phase mark (BPM)
encoding is used to send a 40 Mb/s control stream on the same channel as the 40 MHz Bunch Crossing
(BC) clock. Decoding of the BPM channel within the DORIC recovers both the data stream and the
420 clock signal. The use of individual links for every module permits the adjustment of the timing used to
associate the hit to the bunch crossing. The timing adjustment is accomplished by changing the delay
of the transmitted signal with respect to the phase of the LHC machine reference clock received in the
BOC.

The readout bandwidth required to extract the hits from the detector modules depends on the LHC
instantaneous luminosity, on the L1 rate and on the distance between the module and the interaction
425 point. Simulation of the readout architecture using generated physics events [20] shows that a rate of
40 Mb/s for the Layer-2 modules, 80 Mb/s for the Layer-1 or Disk modules and 160 Mb/s for the b-layer
modules are needed to keep the number of lost hits due to bandwidth saturation sufficiently low. The
data transmitted in the up-links are encoded in non-return-to-zero (NRZ) format. Electrical-to-optical
conversion happens in the opto-boards on the detector side and in the optical-receiver(RX) and optical-
430 transmitter(TX) plug-ins in the BOC.

There are two flavours of opto-boards: Disk/L1/L2-boards (D-board) with eight down-link and eight
up-link channels and b-layer-boards (B-board) with eight down-links and 16 up-links. The B-boards use
two 80 Mb/s channels to obtain the aggregate bandwidth of 160 Mb/s. Because of the modularity of
staves (13 modules) and of sectors (six modules) D-boards use either six channels for the disk-sectors or
435 six or seven channels for the half-staves in Layer-1 and Layer-2.

In the off-detector part of the links, one BOC exists for each ROD. BOCs come with a variety of
hardware options that are implemented by equipping the card with a larger or smaller number of optical-
receiver or optical-transmitter plug-ins. Each plug-in, in principle, can serve up to eight modules, but,
in practice, only six or seven are used due to the modularity of the detector. BOCs come with four TX
440 plug-ins and four RX plug-ins, where the maximum bandwidth requirement is 40 Mb/s, with two TX and
four RX for 80 Mb/s and with one TX and four RX for 160 Mb/s. Two custom chips have been designed
by the SCT collaboration and used in the optical plug-ins: the DRX (12-channels Data Receiver ASIC
in the RX) and the BPM-12 (12-channels Bi-Phase Mark encoder ASIC in the TX). In the BOC there
is also the optical S-Link interface used to send the ROD output to the ATLAS Readout Buffer (ROB)
445 units, which are the next level up in the event readout chain.

4.4.2 Opto-Board

The opto-board is the optical-electrical interface on the detector side. It consists of a beryllium-oxide
(BeO) printed circuit board measuring 2×6.5 cm². As discussed in Section 4.4.1, two types of opto-
boards (D-boards and B-boards) exist and six or seven detector modules are connected to them. The D-
450 boards are equipped with one PiN diode array and one VCSEL(Vertical-Cavity Surface-Emitting Laser)
array, while the B-boards have a second VCSEL array. Each opto-board has two 4-channel DORIC chips,
whereas two and four 4-channel VDC chips are loaded onto the D-board and B-boards, respectively. The
opto-package(opto-pack), which holds the PiN/VCSEL arrays and the connector for the optical fibres, is
custom designed to fulfill requirements of low mass, be non-magnetic and radiation tolerant. The total
455 number of opto-boards in the detector is 288. This is more than the minimum 272 (44 B-boards and 228
D-boards) needed to read out the detector so that spares are available to recover from problems during
integration. Ultimately, only one spare board was used. The remaining spares are mounted on the Patch

Panel 0 elements, but not connected.

PiN Diode Array Arrays of silicon PiN diodes are used to receive the data sent by the VCSELs. Epitaxial silicon PiN diodes are used because their intrinsic layer provides a thin active layer allowing for fast operation at low PiN bias voltage. The active area of each individual PiN diode is circular with a diameter of 130 μm , and the depth of the intrinsic region is 35 μm [21].

DORIC The Digital Optical Receiver Integrated Circuit (DORIC) amplifies the signal detected in the PiN diode and extracts the clock and data from the BPM encoded signal. Data and clock are transmitted in LVDS format to the MCC. Each DORIC chip contains four identical channels. The specification for the current from the PiN diode is in the range of 40 μA to 1 mA. The requirements for the clock are a duty cycle of $(50 \pm 4)\%$ and a time jitter better than 1 ns.

The DORIC has been designed to have a bit error rate of less than 10^{-11} after a lifetime-radiation dose, for a PiN-diode bias current amplitude of 40 μA . The PiN diode current amplifiers use a single-ended scheme [22], avoiding the direct application of the diode bias voltage (10 V), which is much higher than the rating of the DSM technology. The DORIC must withstand up to 170 kGy over the 10 years of ATLAS operation. It is, therefore, implemented in the same (0.25 μm) CMOS technology as used for FE, MCC and VDC.

VDC The VDC converts the LVDS input signal, received from the MCC, into a suitable single-ended signal to drive the VCSELs in a common cathode array configuration. The VDC chips have four channels and drive one half of the VCSEL arrays. An external current used to drive the VCSEL operates up to 20 mA. The nominal current to operate the VCSEL is 10 mA. A standing (dim) current of ~ 1 mA is provided to improve the switching speed in the VCSEL. The dim current is remotely controlled by an external voltage. The requirement for the rise/fall time (20 to 80 %) is in the range of 0.5 to 2.0 ns, where 1.0 ns is nominal. A further requirement, relevant to reducing the pick-up noise, pertains to the constant power consumption of the VDC, that is independent of VCSEL being bright (on) or dim (off). A voltage ($V_{I_{set}}$), remotely controlled, determines the current I_{set} that sets the amplitude of the VCSEL current (bright minus dim current). The chip is designed to have constant current consumption, independent from a VCSEL being bright (on) or dim (off), to avoid generating ripple (noise) on the power supply which is being shared with the two DORICs on an opto-board.

VCSEL Array Vertical-Cavity Surface-Emitting Laser (VCSEL) arrays are used to transmit the data optically. The main advantages of VCSELs are that they provide large optical signals at very low currents and have fast rise and fall times. In order to maintain a low laser threshold current, VCSELs use ion-implants to selectively produce a buried current-blocking layer to funnel current through a small area of the active layer. The VCSELs [21] used in the pixel and SCT systems have an oxide implant to achieve the current confinement, which is becoming the standard VCSEL technology since it produces lower current thresholds at higher bandwidth. VCSELs are produced in arrays of eight diodes. The typical fibre-coupled-power per channel is greater than 1 mW at a drive current of 10 mA. The optical power at 10 mA is sufficient to give a noise immunity of 6.2 dB. Using a slightly higher current is possible, if one adds another 1.8 dB of noise immunity [21]. The down-link, where the current is not a critical issue, can profit from this improved margin corresponding to a higher immunity to SEU and to a lower Bit Error Rate (BER). A PiN current amplitude of 100 μA ensures a BER less than 10^{-9} .

4.4.3 Back of Crate Card (BOC)

Each BOC [21] is connected to one ROD through the crate back-plane. The BOC has two functions:
500 it interfaces between the ROD and opto-links and it controls the distribution of the timing to the on-
and off-detector electronics. Each BOC receives a system clock signal and redistributes it to the pixel
detector modules and ROD. Each detector module needs a precise phase adjustment of its 40 MHz
clock relative to the bunch-crossing time reference. The adjustment of this phase can be done for each
module independently. This is made by an ASIC (PHOS4) that contains four delay channels, which are
505 programmable over the range of 0 to 25 ns. The PHOS4 chip is also used to adjust the sampling clock
that controls data received from the pixel modules. The opto-electrical conversion and the connection
to the fibres is located in two plug-in cards: TX-plug-in and RX-plug-in, respectively, for transmission
and reception of optical data. The TX-plug-in has an 8-channel VCSEL array and a BPM-12 ASIC. The
RX-plug-in has an 8-channel PiN diode array and a DRX ASIC.

510 **DRX** The DRX ASIC amplifies, discriminates and converts the signal from the PiN diode into an
LVDS signal. The comparator is DC coupled and the threshold can be controlled over a current range up
to 255 μA by an external voltage reference generated by a DAC. The DRX chip was originally designed
for the ATLAS SCT detector and contains 12 channels. Only eight channels per chip are used in the pixel
BOC.

515 **BPM-12** The Bi-Phase Mark (BPM-12) ASIC encodes clock and data in the Bi-Phase Mark format
for the fibre optic transmission. This chip was originally designed for the SCT detector and only 8 of
the 12 channels are used for the pixels. A critical specification for this component is to have a short
delay between the input signals and the encoded outputs to minimize the overall L1 trigger delay. The
measured delay value is 60 ns.

520 4.4.4 Opto-fibres

The connection between the BOC and the opto-boards uses optical fibres. Two different kinds of fibres
are used, Stepped Index Multi-Mode fibres (SIMM) and GRaded INdex multi-mode fibres (GRIN).
SIMM fibres have been tested to be radiation tolerant but have lower bandwidth per unit length than
GRIN fibres [23]. To optimise the bandwidth and radiation tolerance, splicing of 12 m long SIMM and
525 70 m long GRIN fibres have been used. The fibres are ribbonised into 8-way ribbons, and eight ribbons
are bundled together to form an optical cable. The 12 m length of the SIMM fibre is terminated
by an MT16 connector at ~ 2.5 m from PP0 (at PP1). A total of 84 cables were installed outside the
Pixel Support Tube. SIMM fiber ribbons were used within the Pixel Support Tube and connected to the
opto-boards mounted at Patch Panel 0 and at PP1.

530 4.4.5 Production and Testing of Opto-Link Components.

The opto-boards were required to pass a stringent quality assurance (QA) procedure, including burn-in
and thermal cycling, at the two production sites. In addition, the boards were required to pass a reception
test at CERN before installation on the service panels. Subsequent tests were also then performed. Each
opto-board was required to produce good optical power, similar to those observed during the production
535 testing of each board, and over a reasonable DAC operating range in the DRX. Three major problems
were encountered during the test and are discussed below [24].

- *Common Serial Resistance (CSR)*. During the reception test it was discovered that some of the VCSELs on the opto-boards produced very little or no optical power on all channels. Moreover

the optical power on one channel was found to also depend on the current from other channels. This could be understood as the development of a common resistance in the array. The voltage drop on the CSR results in an inadequate voltage to drive the VCSELs. The only fault that could be identified in the production process of the opto-pack was that the thickness of the conductive epoxy under each VCSEL array was $\sim 5\mu\text{m}$, as opposed to $\sim 15\mu\text{m}$ as recommended by the manufacturer. A procedure was formulated to estimate the CSR by measuring the current-vs-voltage (IV) characteristics of one VCSEL channel with and without current in the other channels. Opto-boards with $> 2.25\Omega$ of CSR in the VCSELs were rejected, corresponding to $\sim 7\%$ of the total production.

- *Slow Turn On (STO)*. The SCT group discovered that some of their VCSEL arrays took a few microseconds to produce full optical power after a few microseconds of inactivity. A random sample of opto-boards was tested for STO at the production sites and it was found that there was no indication of the problem until the test was performed on a prototype service panel with the production readout chain, including the fibres. It turned out that this subtle STO behaviour depended on the distance between the VCSEL surface and the fiber in a polished, mechanical-transfer (MT) ferrule. The production fiber with the bevelled edges on the MT ferrule allowed the fiber to be pushed closer to the VCSEL, picking up transverse modes that might be time dependent. The exact cause of the slow turn-on behaviour is still under investigation. A new testing procedure was introduced, resulting in the rejection of $\sim 7\%$ of the opto-boards with severe STO VCSELs.
- *Fluctuations in the optical power (noise)*. It was discovered that the optical signal had more noise than was observed during the production testing, because of the long electrical cables. These cables allow noise to enter into the VCSEL bias voltage via the VCSEL current control circuitry in the VDC. A bypass capacitor on the bias voltage was purposely not mounted due to the concern that the capacitor might leak after exposure to radiation, rendering the opto-board inoperable. There was no data to support the above concern but the decision was taken because the opto-boards on the production test system had low noise without the bypass capacitor. Fortunately, the capacitors could be readily retrofitted and this greatly reduced the fluctuation in the optical power.

In addition, another problem was discovered when the prototype service panel was operated with the cooling system. The temperature of the opto-boards at a certain region on the service panel was much lower than anticipated. We required the opto-packs on the opto-boards to produce good power at 10°C as part of the QA requirements. However, a significant fraction of the opto-packs did not produce much optical power at -25°C , another temperature where we collected data as part of the QA procedure. The optical power of these opto-packs was below the specification of $350\mu\text{W}$ on the prototype service panel. To overcome the problem, it was decided to add a remotely-controllable heating element to the opto-boards, giving the possibility to operate at 20°C .

One VCSEL and one PIN channel failed during the detector integration. It is believed that the former was due to electrostatic discharge damage and the latter due to a detached solder (cold solder) on a lead of the opto-pack. In both cases the affected modules were recovering by switching to a spare opto-board in one case and by moving one module to an unused (seventh channel of a board serving only six modules) channel, in the other.

Optical fibres, fabricated and assembled by external companies, have been tested during production by measuring light coupling and attenuation. Two 8-way ribbons in the external optical cables (eight ribbons each) showed failures. Fibres were also tested after installation using a Time Domain Reflectometer and then replaced by spares if they failed the test. Similar tests were performed on the ribbons inside the Pixel Support Tube as they were installed on service panels.

4.4.6 Opto-link Performance

585 The selection and qualification of the components for use in the opto-link system was done by extensive laboratory tests and irradiation campaigns. From the measurements made on single components or parts of the system, one expects a stable performance for the opto-links over 10 year of operation at LHC [22, 23, 25–27]. The measurement of the BER in opto-link ring-loops running at 40 Mb/s (80 Mb/s) gives an upper limit $BER < 1.45 \times 10^{-14}$ ($BER < 3.62 \times 10^{-14}$). In fact no single errors were found 590 during the tests [28]. The method to adjust the timing in the BOC to time the pixel detector with a bunch crossing is reported in [29]. Automatic tuning of the opto-link parameters for the entire detector (the system laser forward currents, PiN-diode photo-current thresholds, etc.) should be achievable in under 10 minutes.

4.5 Data Acquisition System

595 The pixel detector Data Acquisition System (DAQ) has been designed following the specifications of the ATLAS global DAQ architecture [30].

4.5.1 Architecture Overview

The off-detector readout architecture of ATLAS consists of two parts: a sub-detector specific part, where the Readout Buffers (ROD) are the main building blocks, and an ATLAS common design that is referred 600 to as the Read Out System (ROS) [31].

The pixel ROD [32] is a 9U-VME module. The ROD handles the data transfer from the on-detector electronics on one side to the ROS system on the other side. Data from the detector arrive at the RODs through the BOCs. Data passes through the RODs and is then received at the ROS by custom designed interface modules. The ROS is a PC-based system. These PCs temporarily store readout events into their 605 memory and transfer only those accepted by the L2 trigger to the next level up in the readout chain.

ROD modules are plugged into ROD crates. There are nine crates with up to 16 ROD modules per crate. In total, there are 44 modules or three crates for the b-layer, 38 modules for Layer-1 plus 28 modules for Layer-2 or four crates and 24 modules or two crates for the disks. A Trigger, Timing & Control Interface Module (TIM) [33–35] and a Single Board Computer (SBC) [36] complete the ROD 610 crate. The TIM is the interface to the trigger system. The DAQ software running in the SBCs controls the modules in the ROD crate. There is no event traffic on the ROD VME-bus during normal data-taking; data are routed directly from the ROD to the ROS PCs [31] via fast optical links (S-Links). The VME-bus is, however, heavily used during calibration of the pixel detector. RODs are controlled, via the VME-bus, by the SBC which also acts as interface to the global DAQ system.

615 Calibration data are treated differently from collision data. The procedure to calibrate the pixel detector consists of a sequence of injections of a known charge into the pixel's front-end amplifiers. The response of each pixel is measured as a function of the injected charge and of other parameters (thresholds, preamplifier feedback currents, trigger delay) that can be varied during the calibration procedure. The typical result of a calibration scan consists of a set of occupancy histograms corresponding to different values of the scanned parameters. In order to achieve maximum precision, it is important to extract 620 data from the FEs at the maximum speed supported by the detector links. This makes it difficult to extract calibration data using the normal data path, as the read-out chain from the ROS to the Event Builder is designed to transfer only L2-trigger accepted events, while the detector links are designed to support the full L1 trigger rate. For this reason, during calibration runs, the ROD decodes the data stream sent by the front-end electronics, fills occupancy histograms and stores them in memory. The histograms are 625 then extracted via the VME-bus by the SBC and sent to an analysis farm for further manipulation and archiving.

Single Board Computer (SBC) The Single Board Computer is a commercial VP-315³⁾ 6U VME card with a Pentium-M⁴⁾, having 1.6 GHz clock and 1 GB memory. The card uses a Universe II⁵⁾ PCI-VME bridge. It has three gigabit-ethernet interfaces, of which two are used, one to connect to the ATLAS control network and the second to the analysis farm, where histograms generated in the ROD are collected. Up to 40 MB of internal RAM memory is used to cache the configuration data needed in the pixel detector modules for a complete crate of RODs. The configuration data, cached in the SBC memory, are stored offline in an Oracle database⁶⁾ server. The memory is also used as a transfer buffer for the histograms moved from the RODs to the analysis farm.

Trigger, Timing & Control Module (TIM) The TIM is the interface between a ROD crate and the ATLAS trigger system. It receives a TTC fibre-link from a Local Trigger Processor (LTP), carrying LHC bunch crossing (BC) and orbit signals, the trigger signals such as the Level 1 Accept (L1A) and the trigger type, and control/synchronisation signals such as the event counter reset (ECR) and the synchronisation (SYN). These signal are distributed to the RODs via a custom backplane installed in the lower part of the VME crate. On the same backplane, the busy signals generated by the RODs pass to the TIM. The TIM makes a collective ROD card Busy and sends a signal to the LTP. The LPT on reception of the Busy signal stops the L1A to the detector electronics, thus allowing the front-end and ROD buffers to be emptied. Several features are implemented in the TIM to operate on the trigger signal. These include programmable delays on distributed triggers, generation of trigger bursts and strobe signals having a fixed delay from a L1A. Moreover, the TIM can be used as a local trigger generator with a programmable rate. This has been very useful for studying ROD and DAQ behaviour for simulated event rates.

Read Out Driver (ROD) The structure of the ROD is outlined in Fig. 12. Three main sections of the design are the control path, data flow path, and the Digital Signal Processing(DSP) Farm. The control path section consists of two Xilinx Field Programmable Gate Arrays (FPGA) and a Texas Instruments Fixed Point Digital Processor (TI 320C6201 operating at 160 MHz with 32 MB SDRAM). The Program Reset Manager (PRM) FPGA functions as a VME slave controller, allowing read and write access to all ROD and BOC registers and a configuration controller for the data path FPGAs. To enable the users to easily upgrade the firmware on the ROD, the PRM FPGA allows VME access to an on-board flash memory chip that stores the configuration data for all of the data-flow-path FPGAs. The Master DSP receives commands and transmits replies to the VME host and coordinates the configuration, calibration and data-taking modes of the ROD. The ROD Controller FPGA is used in the control path as an interface for the Master DSP to the DSP farm, the BOC, and all of the internal ROD registers in the data flow FPGAs. It also controls all of the required, data-flow-path specific, real-time functions on the ROD, including serial transmission of commands to the FE modules (two independent command streams can be sent to two modules or group of modules), calibration mode trigger generation, and transmission of TIM generated triggers and fast commands. In summary, these are the main actions performed by the control path block:

- full control of ROD reset and FPGA configuration;
- receives and executes command from the SBC via VME;
- receives module configurations via VME and stores them in Master DSP memory;

³⁾From Concurrent Technologies Corporation, <http://www.ctc.com>

⁴⁾From Intel Corporation, <http://www.intel.com>

⁵⁾From Tundra Semiconductor Corporation, <http://www.tundra.com>

⁶⁾From Oracle Corporation, <http://www.oracle.com/>

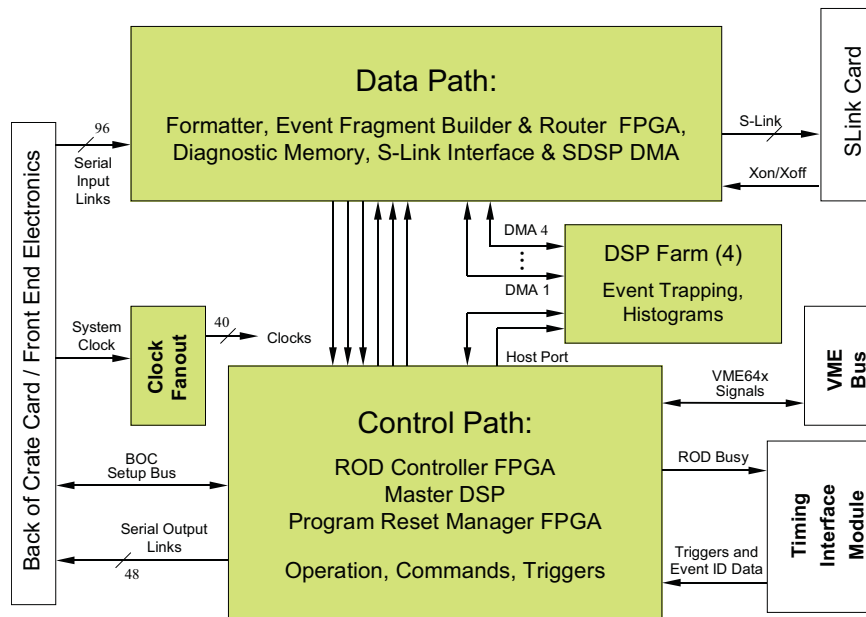


Figure 12: Block diagram of the ROD.

- transmits configuration data to the modules;
- control of calibration procedures, transmitting triggers and configuration data to FE modules;
- control of FE module data histograms;
- propagation of trigger commands from the TIM to the FE modules.

670

The structure of the ROD Data Flow Section is outlined in the block diagram of Fig. 13. The data flow section receives serial data from the FE modules, packs the individual module fragments into a single ROD fragment and sends it to the ROS via a custom designed optical link called the S-Link. Four blocks can be identified: the Input Link Interface, the Formatter, the Event Builder and the Router. Normal event data flows through the ROD via the Input Link Interface, which leaves the data unchanged. It can, however, trap the serial data stream in FIFOs (used in module configuration or to trap an event for diagnostics). The FIFOs can also be loaded with events for analysis by the ROD for diagnostics. After the Input Link Interface, the event data enters the Formatters. The Formatters convert the serial data streams to parallel format, and fill the derandomising buffers used to queue events for transmission to the Event Fragment Builder (EFB) FPGA. An event is transmitted from the Formatters to the Event Fragment Builder after the Controller FPGA sends a command notifying that a Level 1 Accept has been sent to the modules. The ROD Event Fragment is constructed in the EFB using the ATLAS Event ID data that was transmitted from the controller FPGA. In normal data taking, the primary source of the ATLAS Event ID data is the TIM with the ROD providing some additional information. After the header and mode information is sent to the EFB, the ROD Controller FPGA issues one token to the Formatters, and event data is pushed to the EFB. The EFB checks L1ID and BCID values and records errors. It also records any errors that were decoded or flagged by the Formatters. The event data is then stored in 16K derandomising FIFOs (two each). There are two identical engines in the EFB transferring data at up to 40 MHz (total bandwidth 80 MHz). When an event is ready (header, data body and trailer in the FIFOs), it is transmitted to the Router. The Router has two main functions. The first one, which is for the main physics data path, is to transmit 32 bit data words to the S-Link at 40 MHz. If the S-Link is

680

690

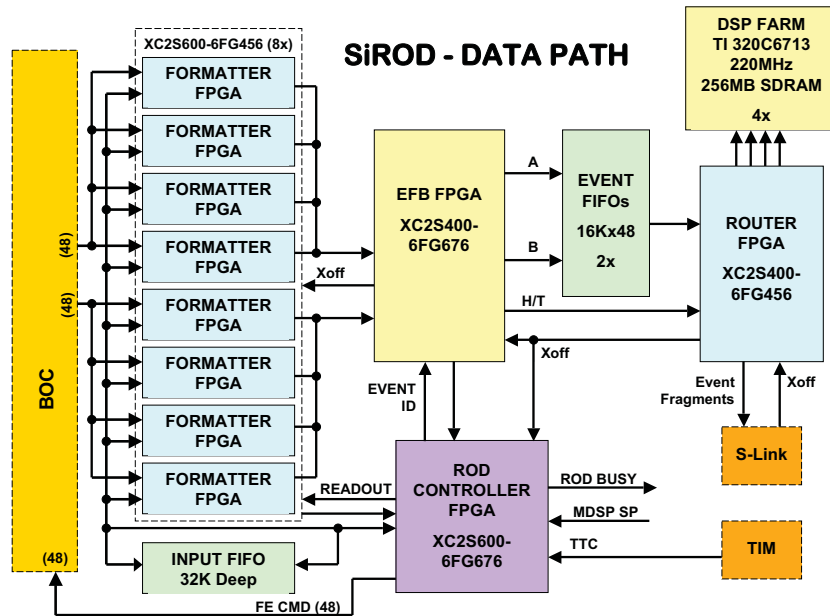


Figure 13: Block diagram of the ROD data flow section.

receiving data faster than it can transfer to the ROS, the S-Link can assert Xoff to apply back pressure to the ROD data path. When back pressure is applied, read out of data from the EFB FIFO is stopped. When the EFB memories are almost full, back pressure is applied to the Formatters. This will stop event data transmission from the formatter link FIFOs. The second function of the Router is to trap data for the DSPs. This is performed with no effect on the S-Link data during normal running. When the ROD is in calibration mode the DSPs can assert back pressure to pause the ROD data flow.

Finally, the ROD is equipped with four 'Slave' DSP processors (TMS320C671314)) with 256 MB memory each. They are connected to the Router FPGA from which they can sample the produced ROD fragments. Different tasks can run on the DSP processors to analyze captured events: monitoring task, used during normal data taking to compute average occupancy and detect noisy pixels or data transmission errors. Calibration tasks accumulate histograms during the multi-dimensional scan procedure and perform an analysis to reduce the data volume to be transferred to the SBC. During data taking the DSPs spy on the data-flow at the maximum possible rate without introducing dead time or applying back pressure on the data flow path. During calibration, on the other hand, the slave DSPs analyse fragments, so they actually become the most important limiting factor on the data rate. For this reason the code of the calibration task must be optimised to maximum efficiency using the 128 KB internal DSP fast memory to fill the occupancy histograms.

4.5.2 ROD Crate Software and Calibration Analysis Farm

The ROD Crate software is the interface between the ATLAS Run Control and the pixel detector DAQ.

For each ROD in the crate, a ROD Interface thread is created. This gives access to the basic functionalities that an external application can perform on the modules using the ROD. The implemented functions range from very basic commands (like ROD module reset and configuration) to complicated scan procedures. The ROD software interfaces are based on Remote Procedure Calls (RPC). They use a Common Object Request Broker Architecture (COBRA) layer called Interprocessor Communication

(IPC) which is used in most ATLAS DAQ applications. These interfaces can be accessed either locally in the ROD, from another process running in the SBC, or from a process running on a remote CPU. Only one application at the time can be allowed access to a given ROD; for this reason, each SBC runs a Crate Broker. Each process accessing a ROD must first ask the Crate Broker, verify if the requested resource is free and allocate it. Only at this point is access to the ROD Interface granted. The last element of the ROD Crate software is the Run Controller. This process is a local receiver of the commands issued by the central ATLAS Run Control.

During normal data taking, the ROD Crate Run Control allocates all the ROD Interfaces and executes the transitions (INITIALISE, CONFIGURE, START, STOP) as indicated by the global Run Control. During calibrations, the Run Control disconnects the RODs, which are then controlled by a Calibration Console, controlling the calibration procedure. The interface/broker mechanism gives the possibility to run a calibration or a debugging session on a ROD while the others are taking data. Occasionally the amount of data produced during a calibration may be too large to fit in the SBC memory. The histograms are then immediately moved (again using IPC) from the SBC to a remote analysis farm, which takes care of the final data analysis, of generating new configuration sets based on the tuning/calibration procedures, and of archiving the results. Consequently, the memory of the SBC is not saturated, and a new scanning procedure is immediately started, while the analysis farm is analysing the previous data set.

4.6 Detector Control System (DCS), Power Supplies, and Interlock System

The operation of the pixel detector modules and of the on-detector opto-components requires a complex power supply [37,38] and control system [39,40]. The following supplies are required at the module and opto-board level:

- V_{DDA} : analog low-voltage supply for the FE chips;
- V_{DD} : digital low-voltage supply for the FE chips and the MCC;
- V_{DET} : high-voltage supply to bias the sensor;
- V_{VDC} : low-voltage supply for the VDC and DORIC chips;
- V_{PIN} : PiN diode bias voltage;
- V_{ISET} : digital voltage to adjust the VCSEL bias;

Power supply requirements for pixel modules and opto-boards are summarised in Table 5. The adjustment of the operating conditions of the system requires a large modularity. Robust software packages are used to monitor and control the hardware. There is, in addition, an independent interlock system that focuses on safety for the equipment and human operators.

4.6.1 The Hardware of the DCS

The scheme of the powering, control and interlock system is shown in Fig. 14. The main components of the pixel DCS are:

- the power supplies to operate the sensors, the front end chips and the opto-boards;
- the Regulator Stations;
- temperature and humidity sensors plus monitoring devices for their readout;
- multi-channel current measurement units;

Supply Type	Supply Voltage (V)	Supply Current (mA)	Nominal Voltage (V)	Nominal Current (mA)	Nominal Power (mW)	Worst Voltage (V)	Worst Current (mA)	Worst Power (mW)
Module								
V_{DDA}	10	1500	1.6	1100	1760	2.1	1300	2725
V_{DD}	10	1200	2.0	750	1500	2.5	1000	2500
V_{DET}	600	2	1.6	600	1	600	2	1200
<i>Module total</i>					3860			
D-board								
V_{VDC}	10	800	2.0	280	560	2.5	490	1225
V_{PIN}	20	20	5.0	–	–	20	20	400
V_{ISET}	5	20	1.0	–	–	2	20	60
<i>D-board (Disk/Layer-1/Layer-2) total</i>					1685			
B-board								
V_{VDC}	10	800	2.0	420	784	2.5	770	1925
V_{PIN}	20	20	5.0	–	–	20	20	400
V_{ISET}	5	20	1.0	–	–	2	20	60
<i>B-board (B-Layer) total</i>					2385			

Table 5: Specifications for module and opto-board power supplies.

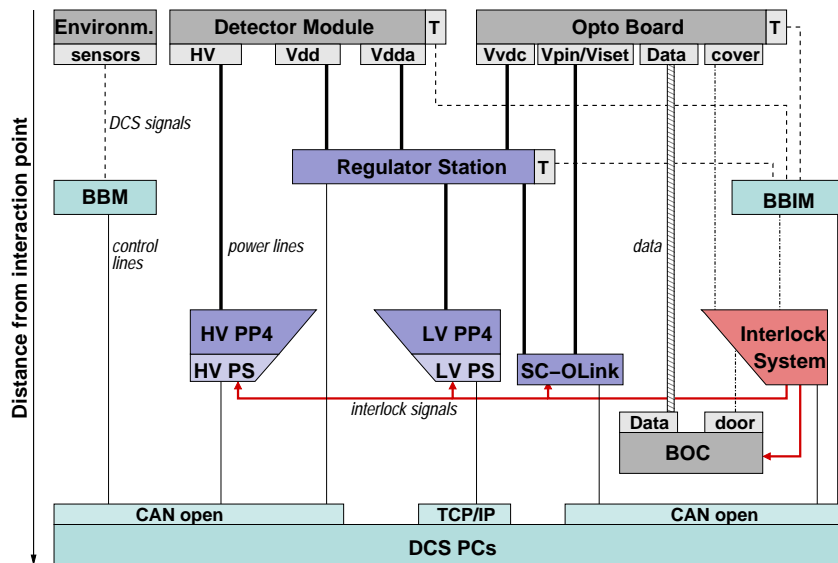


Figure 14: Overview of the hardware of the pixel detector control system.

- the Interlock System;
- the DCS computers to control the hardware.

To comply with the ATLAS grounding scheme, all power supplies and monitoring systems must be floating. Radiation damage during operation of sensors and on-detector electronics requires that all power supplies have adjustable voltage outputs. For operational safety, over-current protection and interlock input signals are available for all the power supplies. The pixel power supply system has five main components: low voltage power supply (LV-PS), high voltage power supply (HV-PS), Regulator Station, Supply and Control for the Opto Link (SC-OLink), and the opto-board heater power supplies. Two low voltages supply the analog (V_{DDA}) and digital part (V_{DD}) of the front-end read out electronics. Both are delivered by the LV-PS, which is a commercial component – the PL512M from WIENER ⁷⁾. To protect the sensitive front end electronics against transients, remotely-programmable Regulator Stations are installed as close as possible (about 10 m) from the detector. These Regulator Stations allow an individual tuning of the power lines through digital trimmers.

The pixel sensors are depleted by the high voltage V_{DET} (up to 700 V) by the HV-PS. The HV-PS is assembled with EHQ-F607n_405-F modules provided by Iseg ⁸⁾. The LV-PS and HV-PS are respectively connected to the low voltage Patch-Panel-4 (LV-PP4) and to the high voltage Patch-Panel-4 (HV-PP4) that are used to distribute the power and monitor the currents of the individual lines.

The SC-OLink, a complex channel consisting of three voltage sources and a control signal, delivers adequate levels for the operation of the on-detector part of the optical link. Monitoring of temperatures and of humidity is performed by the Building Block Monitoring (BBM) and the Building Block Interlock and Monitoring (BBIM) crates. While the first just provides a reading of values, the second additionally creates logical signals, which are fed into the Interlock System. All components of the LV-PS, HV-PS, SC-OLink in addition to the BOC boards are connected to the hardware based Interlock System, that acts as a completely independent system. It consists of several units that guarantee safety for human operators as well as for detector parts. The Interlock System has high modularity; more than a thousand individual interlock signals are distributed. This high modularity has been chosen to maintain a low number of detector modules out-of-service, resulting from some component failure. The Regulator System and parts of the Interlock System, installed inside the ATLAS detector, had to pass requirements pertaining to radiation tolerance; this required extensive qualification for many of the components.

Besides the LV-PS and HV-PS all other components in the system are custom designs, adapted to the pixel specific needs and use the Embedded Local Monitoring Board (ELMB) [41] for monitoring through the DCS. ELMB is the ATLAS standard front end I/O unit for the slow control signals. The Control Area Network (CAN) interface of the ELMB and its CAN-open protocol ensure that the communication is reliable and robust. Different Openness, Productivity, Collaboration (OPC) servers are used to integrate the hardware into the higher level of the software. All together 630 CAN nodes on 43 CAN busses and 48 TCP/IP nodes for the LV power supplies are used to build the pixel control network. In total, more than 44000 variables need to be monitored.

4.6.2 The Software of the DCS

The DCS software establishes the communication to the hardware, to support the operator with all required monitoring and control tools, and provides automatic safety procedures as well as easier operation of the detector for non-DCS experts. Additionally, detector operation requires good coordination between the DAQ and DCS actions. Data relevant to the offline analysis must be recorded and stored in the

⁷⁾WIENER, Plein & Baus GmbH, Burscheid, Germany

⁸⁾Iseg Spezialelektronik GmbH, Rossendorf, Germany

conditions database. The core of the DCS software is the Prozess- Visualisierungs- und SteuerungsSoftware (PVSS), ⁹⁾. These projects run as a distributed system on eight control stations. Since each part of a distributed system has its own control and data managers (processes inside PVSS), an independent development and operation of the different projects is possible. The core of the control software is the Front-end Integration Tools (FIT) which establish the communication with the hardware components. For each hardware component, like the HV-PS, the LV-PS and the different devices using the ELMBs, dedicated FIT exist. Each FIT consists of an integration and a control part. The integration part initialises each given hardware component and creates the data structures required to control it. The control part of the FIT supervises the operation of the same component. The FITs are mainly foreseen for the DCS expert who needs to check the correct behaviour of the hardware. For persons who run shifts in ATLAS, a detector oriented view of the hardware is provided by the System Integration Tool (SIT). The mapping of the read-out channels to the detector devices is done by the SIT. The SIT creates a virtual image of the detector inside the DCS. It combines all information which is relevant to the operation of the detector unit such as a half stave, a disk or even the full detector. Furthermore, the SIT is responsible for storing the data in the conditions database.

The software used to operate on the detector is the Finite State Machine (FSM). This software was developed in common for the four largest LHC experiments [42]. The FSM uses geographical, organised data structures, created by the SIT, and provides the user with a set of commands to act on small or large fractions of the detector simultaneously. The detector status is returned by the FSM. Furthermore, proper settings and special power-on sequences are performed automatically by the FSM. In addition, the FSM builds the link into the ATLAS wide control system. As part of the overall ATLAS control system, the pixel FSM will receive commands from the ATLAS FSM during normal data taking. The communication between DAQ and DCS is provided by DAQ-DCS Communication (DDC), which provides command transfer from the DAQ system to DCS, publishes DCS values to the DAQ and vice versa. For the tuning of the optical links, the DDC is critical.

The DCS hardware and software system has been fully exercised in various configurations during the prototype and construction phases of the pixel detector, namely in test beams, with cosmic ray tests and during the integration of the pixel detector at CERN [43, 44].

5 Sensors

Sensors are the sensitive part of the pixel detector for charged particle detection and function as a solid-state ionization chamber. The sensor must meet exacting geometrical constraints concerning thickness and granularity as well as have a high charge collection efficiency within the sensitive volume, while sustaining a massive amount of ionizing and non-ionizing particle radiation damage. On one hand, this is reflected in the selection of the bulk material and, on the other hand, it impacts the design of the pixel structure itself.

5.1 Design

The ATLAS pixel sensor is an array of bipolar diodes placed on a high resistivity bulk close to the intrinsic charge concentration. The sensor is made by implanting high positive (p^+) and negative (n^+) dose regions on each side of a wafer. An asymmetric depletion region at the p^+-n junction operates in reverse bias and extends over the whole sensor bulk volume. Here one is able to collect and detect all charges in the volume produced by ionizing particles. The sensor concept guarantees single pixel isolation, minimizes leakage current and makes the sensor testable as well as tolerant to radiation damage.

⁹⁾PVSS is made by ETM, Eisenstadt, Austria

The pixel sensor consists of a $250\ \mu\text{m}$ thick n-bulk with n^+ implants of size $400 \times 50\ \mu\text{m}^2$ on the read-out side and the p-n junction on the back side. For each sensor tile, the 47232 pixel implantations are arranged in 144 columns and 328 rows. In 128 columns (41984 or 88.9 %) pixels have a size of $400 \times 50\ \mu\text{m}^2$ and in 16 columns (5248 or 11.1 %) pixels have a size of $600 \times 50\ \mu\text{m}^2$. In each column eight pairs of pixel implantations near the center lines are ganged to a common read-out, resulting in 320 independent read-out rows or 46080 pixel read-out channels. This arrangement was chosen to allow the connection of the sensor tile to 16 electronic front-end chips, see section(4). Aside from increased leakage current, radiation damage will invert the sensor bulk and then gradually increase the depletion voltage. For unirradiated sensors, the depletion starts at the back (p) side where the pixels are not isolated from each other until full depletion of the bulk. Irradiation of the bulk leads to a change in the effective doping concentration N_{eff} : first N_{eff} drops off and then runs through type inversion after which N_{eff} increases [45]. At type inversion, the junction moves to the front (n) side, isolating the pixels and enabling operation even if the bulk cannot be fully depleted. Maximum achievable depletion is desirable to maximize the signal. The advantage of the depletion zone for the n^+ -in-n design is shown in Fig. 15.

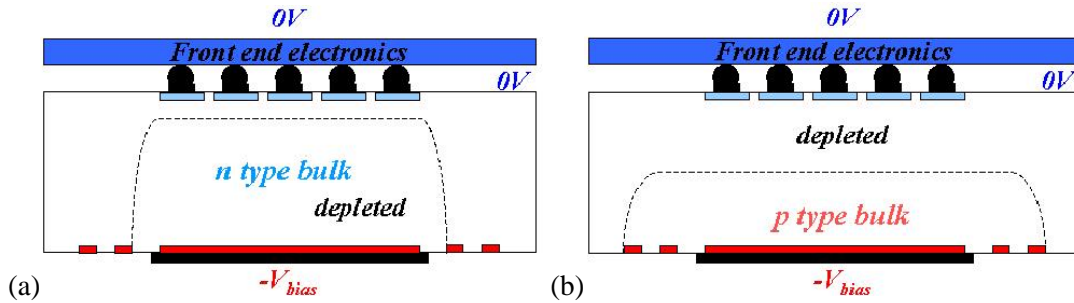


Figure 15: Comparison of depletion zones in n^+ -in-n pixel sensors before (a) and after (b) type inversion. Before type inversion the electrical field grows from the backside and reaches the pixel implants (full depletion). After type inversion the depletion zone grows from the pixel side and allows operation even if the bulk is not fully depleted.

Oxygen impurities in the bulk ensure high tolerance of the silicon against bulk damage caused by charged hadrons [46, 47]. A comparison of the evolution of charge densities in standard and oxygenated silicon during irradiation with hadrons is shown in Fig. 16a. In addition to the continuous irradiation of the sensors affecting the induced doping concentration, N_{eff} also evolves due to thermal effects. On short time scales, N_{eff} drops off (beneficial annealing), runs then through a minimum of constant damage and finally increases again on longer time scales (reverse annealing). See Fig. 16b.

While the beneficial annealing is not altered in oxygenated silicon, the constant radiation damage (N_C) is reduced, and the reverse annealing (N_Y , see Fig. 16b) is significantly slowed down [46, 47], producing a lower overall effective charge density in similarly irradiated samples undergoing identical annealing scenarios. Sensors built from such material exhibit deeper depletion zones at the same bias voltage and full depletion at a lower bias voltage.

By choosing an appropriate temperature profile (i.e. operation at 0°C , short periods of $+20^\circ\text{C}$ during detector access, and cooling down to -20°C during longer operational breaks in the experiment), one tries to keep sensors near the lowest possible N_{eff} and avoid reverse annealing to derive benefit from the lowest possible depletion voltage. Model calculations (Fig. 17) of the combined effects of bulk irradiation and annealing have been performed [48]. The increase of the intrinsic charge carrier concentration due to radiation exposure leads to higher leakage currents and also contributes to noise. Cooling of the sensors to values well below room temperature helps reduce these effects.

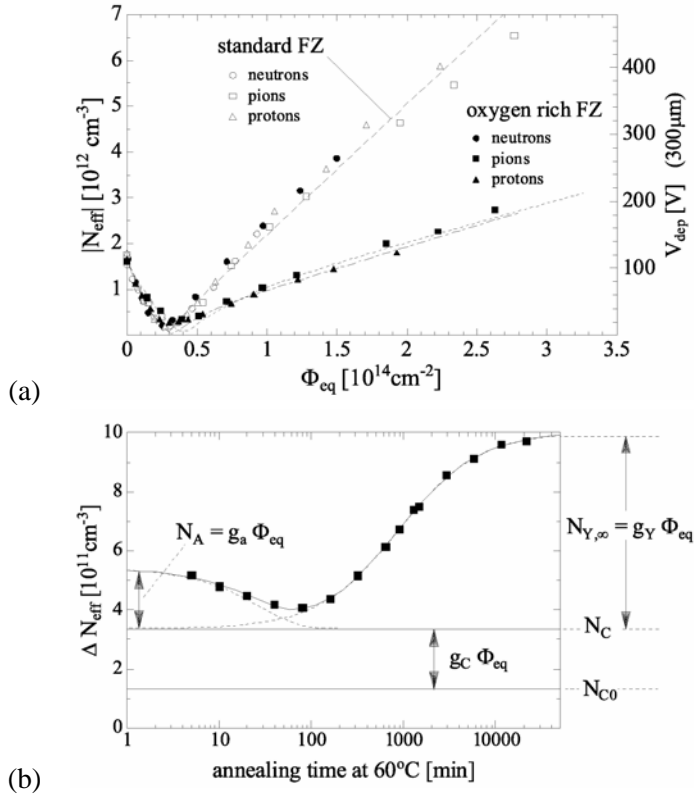


Figure 16: (a) Evolution of effective charge densities and full depletion voltage in standard and oxygenated silicon during irradiation with various hadrons. In oxygenated silicon the increase after type inversion induced by charged particles (pions, protons) is significantly lower. (b) Evolution of the effective doping concentration due to annealing and reverse annealing effects. The parameterization of this evolution is the so-called ‘‘Hamburg model’’ and represents an important input to the ATLAS pixel sensors, which will operate near the point of minimal depletion voltages. In oxygenated silicon, both N_C and N_Y are reduced [46, 47].

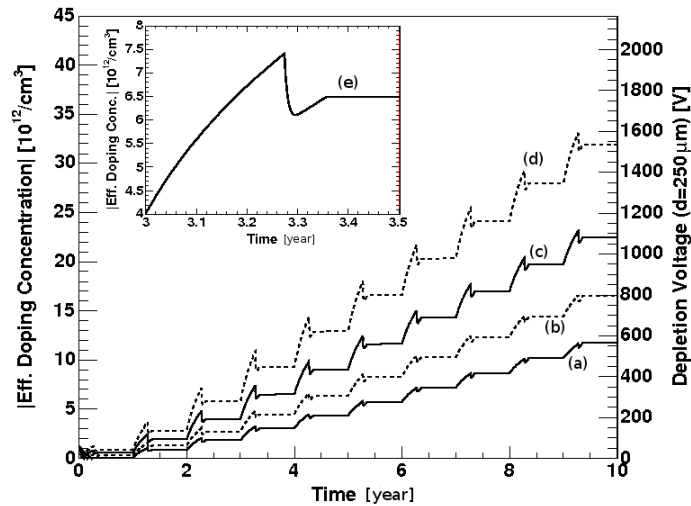


Figure 17: Change of the effective doping concentration (left scale) and the voltage necessary for full depletion (right scale) of oxygenated sensors according to irradiation and annealing effects under the Hamburg model for the two inner pixel detector layers in a standard (solid) and elevated (dashed) radiation scenario. (a) Layer 1 at 8.85 cm radial distance from interaction point with a standard fluence of $0.9 \times 10^{14} \text{ cm}^{-2} \text{ year}^{-1}$ (the 3rd year of operation), (b) the same as (a) with a 50% elevated fluence, (c) b-layer at 5.05 cm radial distance from the interaction point with a standard fluence of $2.4 \times 10^{14} \text{ cm}^{-2} \text{ year}^{-1}$, (d) the same as (c) with a 50% elevated fluence. The enlarged detail (e) shows the evolution of the sensor characteristics during one year of assumed detector operation: 100 days of beam operation with irradiation at an operation temperature of 0°C , a period of about 30 days at $+20^\circ\text{C}$ during detector access, and cooling down to -20°C during the rest of the year.

870 The positive and the negative implanted sensor wafer sides are both structured by mask processes for implantation, metallisation and deposition of silicon-oxide and silicon-nitride. This double sided processing demands precise mask steps and incorporates front-to-back mask alignment of a few micrometers. However, this allows for a segmented n^+ implantation used for the definition of pixel cells and a guard ring structure on the p^+ implanted wafer side, locating the main voltage drop on the sensor surface opposite to the bump connections [49, 50]. The 250 μm thick high resistivity silicon bulk of 2 to 3 $\text{k}\Omega/\text{cm}$ can be fully depleted before type inversion with bias voltages below 100 V. After type inversion the depletion zone grows primarily from the segmented n^+ implantation when the region of highest electric field in the bulk now converts to p-type.

880 On the sensor front side, pixel structures are arranged and isolated by moderated p-spray [50, 51] implantations which have proven to be radiation tolerant with respect to surface damages induced by ionising charged particles for doses up to 500 kGy in silicon. The principal layout is shown in Fig. 18a. The dose of implant ions leading to the moderated p-spray isolation is regulated with a help of a nitride layer which is opened during an additional mask step, creating a deeper high dose p-spray region in the center of the inter-pixel gap and a shallower low dose layer everywhere else. This isolation technique
885 avoids high field regions in the interface between the pixel isolation and bulk and ensures radiation tolerance of the design [52, 53]

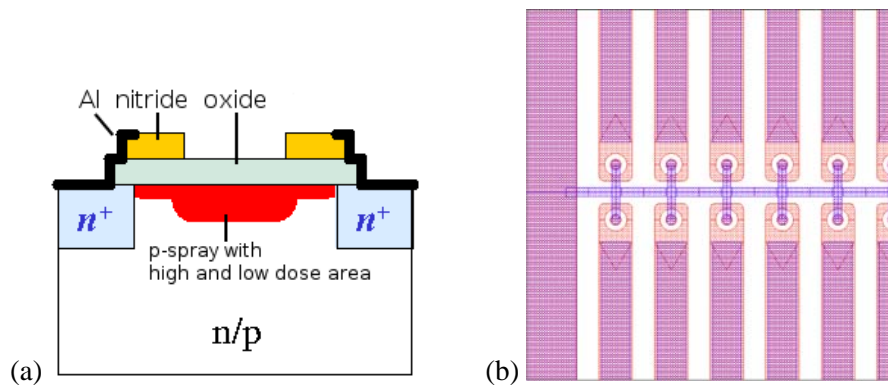


Figure 18: (a) Principal layout of the moderated p-spray isolation which consist of high and low dose areas between the n^+ pixel implantations in the n bulk. Compared to other isolation profiles like p-stop [54] and p-spray [51] high field regions are avoided in the transition regions between pixel and bulk. (b) Layout detail of the bias grid [50] visible in the production mask for a pixel double row.

All 46080 read-out channels of a sensor tile are connected to a common bias grid structure [50] (Fig. 18b) by employing a punch-through connection technique to each channel. The method biases the entire sensor without requiring individual connections, but still ensures isolation between pixels.
890 This bias grid has been used for quality assurance measurements prior to the read-out electronics being connected to the sensors. An opening for each pixel in the passivation layer of the sensor allows for a connection to each channel using a bump-bond technique (see section 6) to front-end electronics (see section 4), which is DC-coupled and provides biasing for each individual pixel.

5.2 Prototyping and Tests

895 Bulk and surface design features of the sensors have been extensively tested during the prototype phase [53] and a dedicated pixel sensor quality assurance plan was developed [55]. The sensor layout has been designed on four-inch-diameter, double-sided wafers, which include three sensor tiles of about

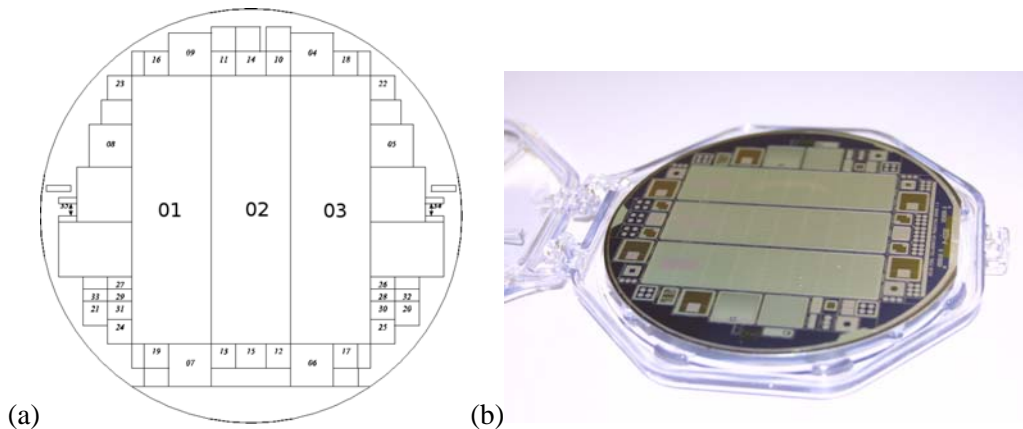


Figure 19: (a) Geometrical layout of the sensor wafer. Central large structures 01, 02 and 03 are the sensor tiles carrying 46080 read-out channels employed in the ATLAS pixel sensor modules; structures 04 to 35 are dedicated test structures to monitor the quality of prototyping and production. (b) A pictorial view of the 4-inch diameter ATLAS pixel sensor wafer (p-side view).

18 mm × 62 mm each. During the prototype phase, dedicated test structures were developed. The test structures were placed on the ATLAS pixel sensor wafer surrounding the sensor tiles to allow for dedicated electrical tests of various design features for the sensor (Fig. 19).

The sensor quality control included mechanical as well as electrical inspections and tests. Examples of visual and mechanics tests include unique wafer identification with the help of scratched serial numbers, visual inspection of the surface quality, a check of the mask alignments, and planarity as well as thickness measurements of wafers. Electrical tests included measurement of the leakage current and the capacitance of diodes using the guard ring structure. Leakage currents were monitored on sensor tiles, and on test structures. Current and capacitance measurements were performed on oxide structures.

As an example of the bulk characteristics, the dark current on sensor tiles was monitored. The breakdown voltage was required to be well above 150 V. Fig. 20 shows an example of measurements performed during the prototype phase. The two blue curves are examples of nearly perfect diodes, the black curve shows a breakdown between 150 and 200 V and the red curve shows a very steep breakdown behaviour near the typical depletion voltage indicating a defect on the n-side of the sensor.

Since the moderated p-spray dose is one of the critical steps in the sensor design, the measurement of the p-spray dose is an important quality control test. Here, a dedicated punch-through structure as well as an oxide structure is needed to determine the oxide capacitance. An example of a punch through measurement is shown in Fig. 21. The idea of this measurement is to determine the current I between an individual pixel and the bias grid (Fig. 21a) as a function of the potential difference ΔV , while the sensor bulk is biased at -150 V. The resulting current (Fig. 21b) increases for good isolations at $\Delta V > 1$ V. This together with the oxide measurement (not shown) leads to the p-spray dose [55]. This example demonstrates the need for advanced quality control measurements to assure the radiation hardness of production sensors. A few sensors were rejected during the production process.

One important aspect of the present ATLAS pixel sensor is the operation under irradiation, especially near the end of the sensor's lifetime. Here, the main limitation of the sensor is the trapping of charge carriers in the silicon bulk, which leads to decreasing values for the collected charge during the operation time of the detector. Trapping times have been determined in test beams [56], and laboratory set-ups [57]. Based on the operation model (see Fig. 17) of the ATLAS pixel sensor, the expected collected charge for minimum ionizing particles passing through the $250\mu\text{m}$ thick bulk is predicted to be between 15

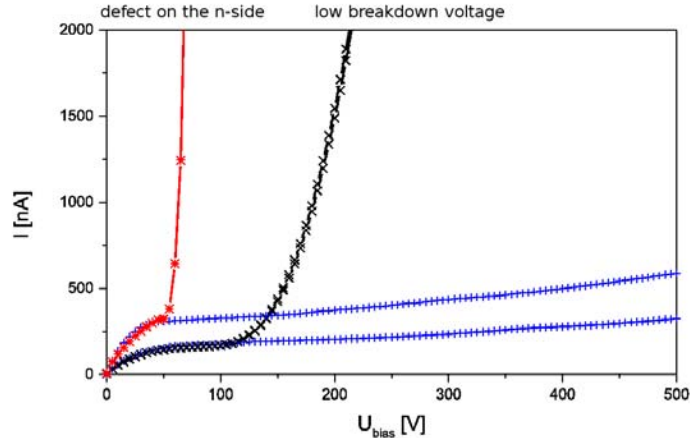


Figure 20: Examples of dark current vs. bias voltage curves on pre-series sensors tiles. While the two blue curves are examples of nearly perfect diodes, the black curve shows a break down between 150 and 200 V, and the red curve shows a very steep break down behaviour near the typical depletion voltage, indicated a defect on the n-side of the sensor.

and 19 ke after irradiation fluxes of $8-12 \times 10^{14} \text{ cm}^{-2}$ [58]. These values are expected after 10 years of operations for sensors in Layer 1 of the ATLAS pixel detector. The values agree nicely with those derived from test beam results performed using production-like sensors [59]. Further performance features, including those for the sensors, were extracted under test beam conditions, the results of which are summarized in section 7.

5.3 Production and Quality Assurance

Sensor tiles have been produced by two independent vendors, who went through the prototype phase and qualification process. Based on the experience during prototype development, specialized quality assurance procedures were employed for the series production of sensors [60,61] and were carried out as a collaborative effort at four different pixel sensor institutes. Extensive cross calibration of mechanical and electrical measurements was performed during these processes.

The rate of production of ATLAS pixel sensors is shown in Fig. 22. More than 2200 sensors successfully passed through the quality assurance process and were available for hybridisation [62] to the front-end electronics.

6 Modules

6.1 Overview

The sensitive area of $\sim 1.7 \text{ m}^2$ of the ATLAS pixel detector is covered with 1744 identical modules, independent of their spatial position, with a small exception (see below). Each module has an active surface of $6.08 \times 1.86 \text{ cm}^2$. A module is assembled from the following parts

- the sensor tile containing 47232 pixels as described in section 5;
- sixteen front end electronics chips (FE) each containing 2880 pixel cells with amplifying circuitry, connected to the sensor by means of fine-pitch bump bonding (see section 6.2);

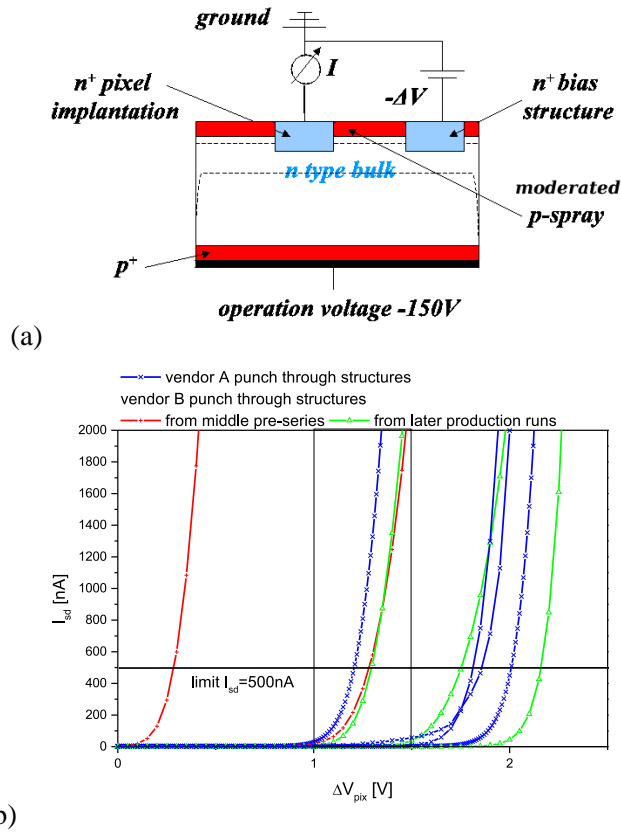


Figure 21: (a) Electrical set-up to monitor the bias dot current vs. the potential difference test on a depleted substrate. (b) Example of punch-through current measurements on several prototype structures at the nominal bias voltage of 150 V. The left red curve is an example of a below specification low potential difference, which occurred during early prototyping, compared to later production, which fulfilled the isolation criteria of more than 1 V.

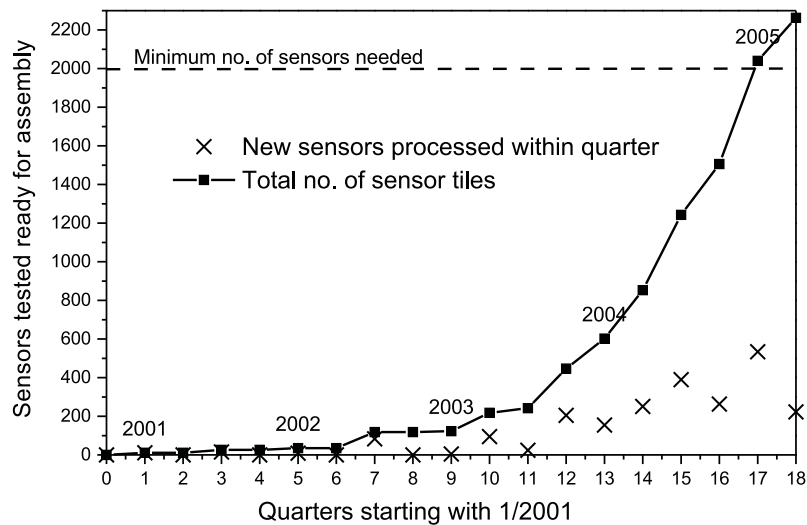


Figure 22: Tested sensor tile output in total and per quarter during the production process.

970 A complete module draws 1.2 A at 1.6 V from the analog supply and 0.8 A at 2 V from the digital supply or about 3.5 W per module. This value is expected to increase to about 5 W after an accumulated dose of 500 kGy.

The bump bonding and flip-chip operation results in a so-called bare module. The sixteen chips of an assembled bare module are first tested on a probe station to detect defects such that rework on a module
975 can be done at this point of the assembly sequence.

Region in between Chips

The sensor pixels have dimensions of $50\ \mu\text{m} \times 400\ \mu\text{m}$, except for about 11% which have a size of $50\ \mu\text{m} \times 600\ \mu\text{m}$, to allow for a contiguous sensitive area between chip boundaries in the long pixel direction. In the perpendicular direction, 2×4 pixels under each of the two adjacent chips cannot be
980 covered by active pixel circuitry. These off-side sensor pixels are connected through metal lines on the sensor to $4 + 4$ neighboring electronics pixels at the top of the columns in addition to the cells which lie directly underneath as is illustrated in Fig. 24. The resulting hit ambiguity is resolved by the off-line pattern recognition software. These special pixels - (inter-ganged pixels), the $600\ \mu\text{m}$ size (long pixels), the pairs connected to a single readout channel (ganged pixels) and the ones below the metal line connecting
985 two ganged cells - have slightly degraded electrical performance due to the increased sensor capacitance (see section 6.6).

6.2 Bump Bonding

Bump bonding is extensively used in the electronics industry for the attachment of integrated circuit die to printed circuit boards or other substrates. Two different bump bonding techniques have been used
990 for ATLAS: electroplated-solder(PbSn) bumping [63, 65] and evaporative-indium bumping [66]. Both bump deposition processes are done at the wafer level. The principle of a bumped sensor – electronics pixel element is sketched in Fig. 25. The substantial demands on the handling require that the wafers get bumped with their original thickness ($\sim 700\ \mu\text{m}$ for the 20 cm integrated circuit wafers). Wafer thinning is done after bump deposition by covering the bumps with a photoresist layer and a UV releasing tape for
995 bump protection and for handling. The integrated circuit wafers are then thinned by backside grinding to about $190\ \mu\text{m}$. They are diced immediately afterwards and then the die are tested again on a probe station to assure that they are still functional and ready for the flip-chip process.

6.2.1 The Solder Bumping and Bonding Process

In eutectic PbSn solder bumping [63, 65], the solder is deposited through electroplating. Under bump
1000 metallization (UBM), which consists of several metal layers is deposited on the contact pads. A PbSn cylinder is galvanically grown and melted to a sphere on the integrated circuit wafer, while the sensor wafer receives only the UBM [64, 67]. The parts are mated by flip-chip assembly with reflow which provides self-alignment. The process flow is described in [70]. The distance between chip and sensor is about $20 - 25\ \mu\text{m}$, thus minimizing the cross-talk between the electronics and sensor. The connection
1005 resistance is smaller than $1\ \Omega$ and the ultimate shear stress is $\approx 50\ \text{MPa}$. A picture of PbSn bumps after reflow on an ATLAS FE-chip are shown in Fig. 26b.

6.2.2 The Indium Bump Bonding Process

In the case of indium bonding, the bumps are grown by depositing evaporated indium on both mating parts [68]. The bump pitch is also $50\ \mu\text{m}$, but the bump height is limited to $10\ \mu\text{m}$ due to the use of
1010 a lift-off process for the removal of the polyimide evaporation mask. Bumps are deposited both on the

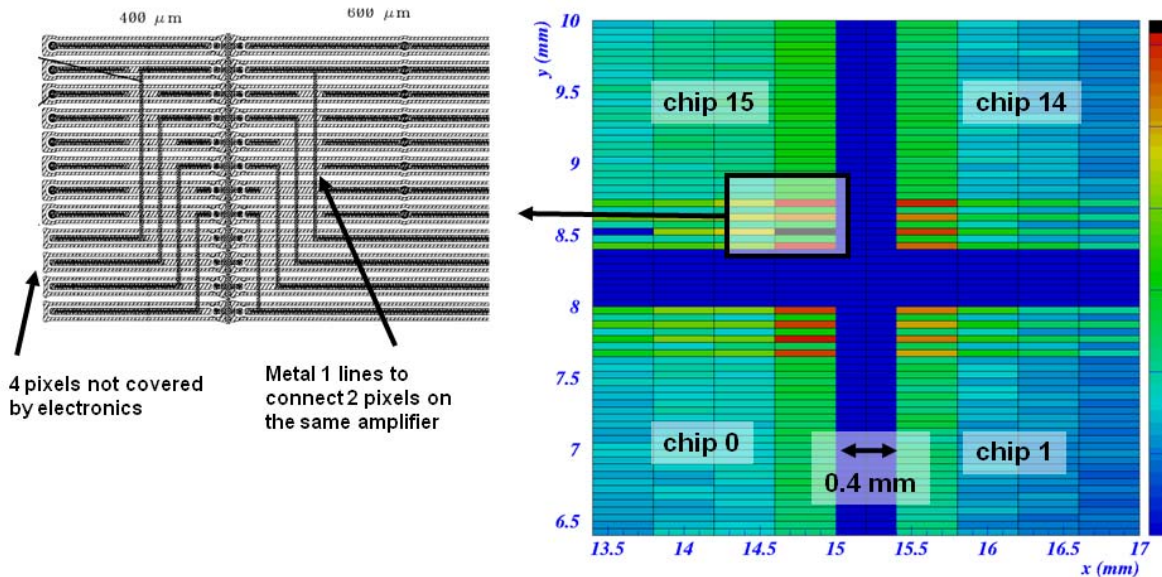


Figure 24: End-region of the pixel detector at the edge of four FE-chips. The area of the sensor covered by the chip edges is marked in grey. The pixels in between the chips (white rectangles) are connected through metal lines to another pixel underneath the chips.

sensor and on the electronics wafers. Mating is obtained by In-In thermocompression. The process flow is described in [70]. Fig. 27 shows a micrograph of $50\ \mu\text{m}$ pitch indium bumps deposited on two glass samples and then flip-chipped together [66] at a temperature of $\sim 100^\circ\text{C}$ applying a pressure of about $20\ \text{N}/\text{cm}^2$ per chip. The distance between chip and sensor after bonding is $\approx 10\ \mu\text{m}$.

1015 6.3 Quality Control of Bump Bonded Assemblies

Inspections before and after flip-chip assembly were crucial to obtain the highest yield for functional pixel modules. Automated inspection of bumped wafers with the combined use of a television camera and laser interferometry allowed the manufacturer to find missing bumps, merged bumps, deformed bumps or other defects as well as to measure bump heights on wafers. Inspection with high resolution
 1020 ($2\ \mu\text{m}$) X-ray machines allowed one to detect misalignment or merged/bridged bumps previously not detected or caused by the flip-chip process. Both solder and indium bump bonding have been used to produce pixel modules with bump defect rates of $\approx 10^{-5}$ – 10^{-4} at the wafer level and $\approx 10^{-4}$ – 10^{-3} after the flip-chip process.

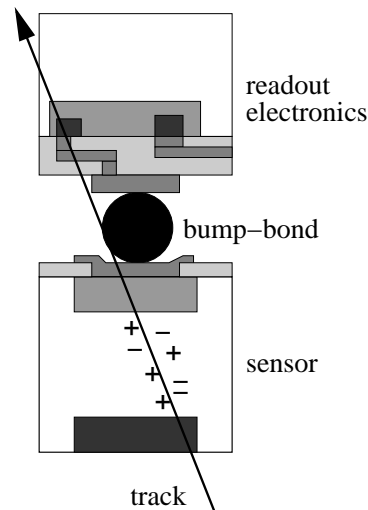


Figure 25: Blow-up sketch (not to scale) of the cross section of a hybrid pixel detector, showing one connection between a sensor and an electronics pixel cell. A particle track releases ionisation in the sensor volume.

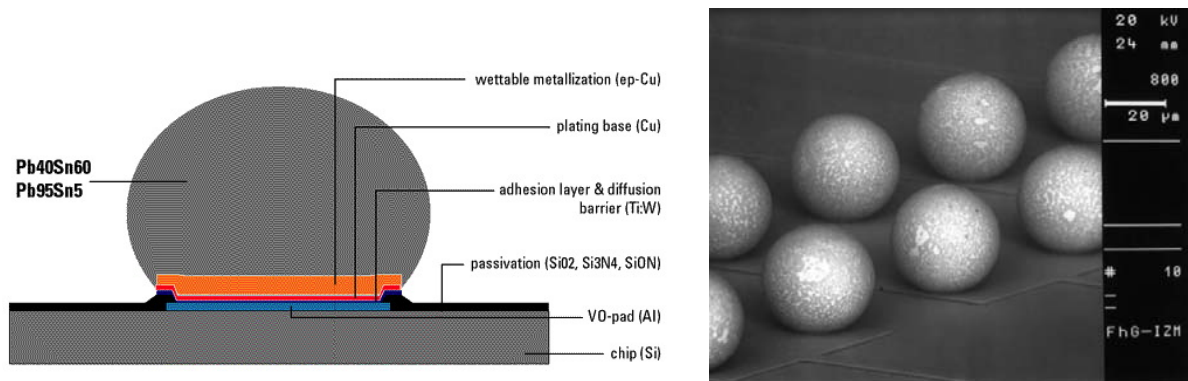


Figure 26: a) Schematic description of a eutectic PbSn solder bump [63, 65], (b) rows of a PbSn bumps (courtesy IZM-Berlin).

6.4 Reworking of Bump Bonded Assemblies

1025 All modules were built with known good die (KGD) i.e. all die were tested prior to flip-chip and only the good ones are used. This is a crucial requirement as the module yield goes with the n^{th} power of the electronics chip yield, n being the number of chips-per-module.

All front-end chips were also electrically tested after bump bonding in order to check for damage to the front-end electronics and to assess if the quality of the electrical contact was adequate.

1030 Both solder and indium bump bonded modules have been successfully reworked [67, 69] with a success probability of more than 95%. In both cases, the operation requires heating and application of a force to remove the integrated circuit, while leaving some metal on the bond pads. Afterwards, a new IC is flipped to the sensor. The probability to properly connect all pixels in the second flipping is near 100%.

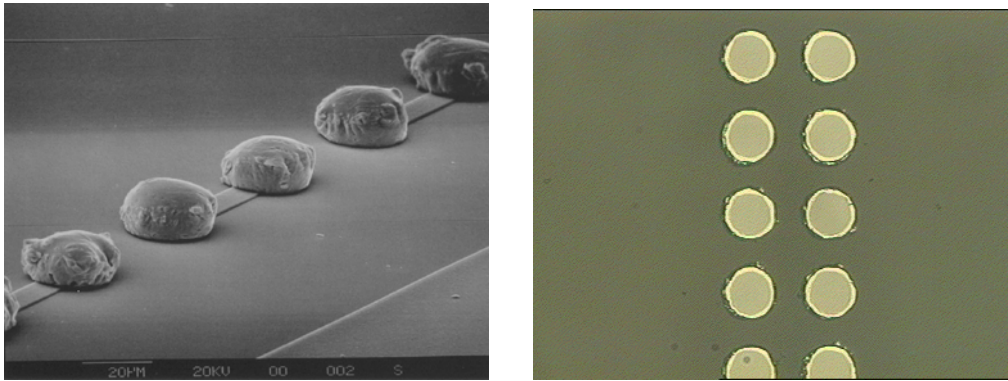


Figure 27: Micrograph of a Indium bump deposition on silicon at $50\ \mu\text{m}$ pitch (left) and of a flip-chip assembly of two $50\ \mu\text{m}$ pitch bump arrays (right) on glass substrates (courtesy SELEX Sistemi Integrati, Rome) [66].

1035 6.5 Module assembly

Once a bare module has passed the acceptance test, it is equipped with a flex-hybrid to provide the connections between the Module Controller Chip and the front-end electronics and from the Module Controller Chip to a microcable. A photograph of a barrel module is shown in Fig. 28.

1040 The flex-hybrid is a double-sided, flexible printed circuit with a $50\ \mu\text{m}$ substrate thickness and $25\ \mu\text{m}$ thick copper lines¹⁰⁾. It has been specifically designed to cope with the maximum 600 V depletion voltage applied to the sensor. It also includes passive components for local decoupling and an NTC for monitoring the module temperature.

1045 To facilitate testing of flex hybrids, they were attached to custom-made printed circuit boards (flex support card or FSC), which were used for handling of the flex-hybrids themselves and after attaching the hybrid to a module. A module is cut out from the FSC just prior to loading on a local mechanical support [4].

1050 Flex-hybrids for barrel and disk modules are identical. A difference appears only when the connection to the services is made. For barrel modules, an additional flex circuit (pigtail) is glued on top of the flex hybrid and electrically connected by wire bonding. It has a zero-insertion-force connector which is fixed to the back side of the barrel-region local mechanical support(stave) and used for attachment of the low-mass microcables. Disk modules instead use thin copper wires for the microcables, which are soldered directly to the flex hybrid [4].

1055 There is a significant difference in the coefficient of thermal expansion between kapton and silicon. The glue used for attachment of the flex hybrid to the bare modules needs to be distributed to avoid any excessive mechanical coupling between the two. On the other hand, a strong connection is required in the places where wire bonds are needed. Therefore, the glue is deposited along the pads lines used for the interconnection between the flex hybrids and the front-end electronics, below the MCC, near the high voltage bonding pad and, for barrel modules, below the pigtail attachment point.¹¹⁾

6.6 Testing and Selection Procedures

1060 After loading on a FSC, a module can be connected to a test setup using cables. The test setup in the laboratory used LVDS signals. The readout chain and control software was the same as that used for the

¹⁰⁾Manufactured by Dyconex AG Bassersdorf, Switzerland.

¹¹⁾Dow Corning SE4445.

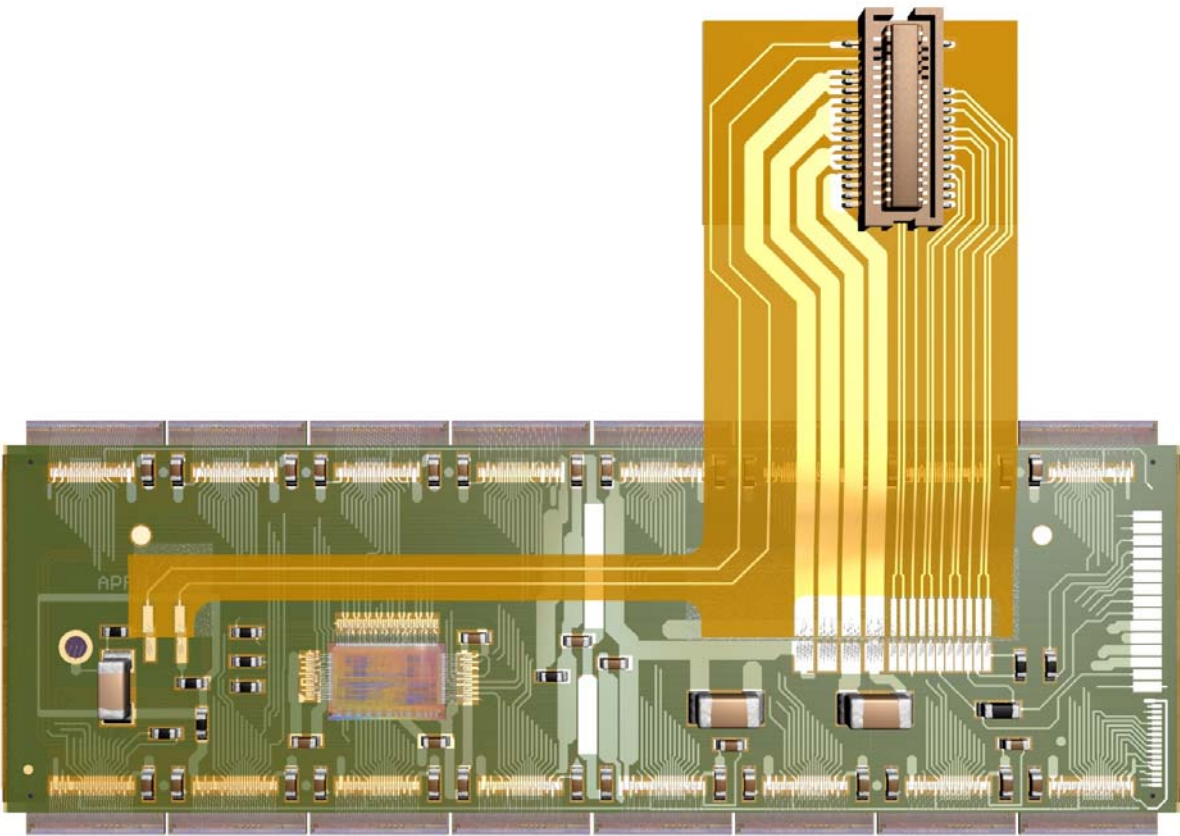


Figure 28: Picture of an ATLAS pixel barrel module.

front-end electronics and bare module testing, except now configured to communicate via the MCC and used the microcable instead of probe needles for communication with the integrated circuits.

1065 The characterisation procedure [71, 72] aims to certify if a module is acceptable for operation, both electrically and mechanically. A ranking value is determined such that better modules can be selected for the most critical parts of the detector. In particular, a module must satisfy the following conditions:

- the electronics should be tunable and have enough operation range to guarantee there will be tuning capability to operate even after radiation damage;
- the bump bonding has not been damaged by the assembly procedure;
- 1070 • the wire bonding of MCC and FE is done correctly.

The testing sequence proceeds as follows:

- a basic series of electronics tests is performed at room temperature after module assembly;
- modules undergo a mechanical stress test, being cycled 10 times between room temperature and -30 °C, with a cycle length of about 2 hours;
- 1075 • electronics tests at room temperature are repeated after thermal cycling and compared to the initial tests;
- a complete module characterization is performed at about -10 °C, which is the expected operating temperature.

1080 The last test is the most relevant for the definition of module quality and selection for usage in the detector. Reduced electronics test are also performed after loading of modules into the local supports, to monitor possible damage after loading, which may trigger the repair or replacement of a module.

The room temperature tests consist of:

1. a basic functionality test: the module is configured, the readout chain is tested by the digital injection and the amplifier cells by the analog injection;
- 1085 2. a test of module tunability: thresholds are equalized to about 4000 e;
3. a threshold scan without depletion voltage applied to the sensor.

The first test is mainly a check of the wire bonding or for electrostatic discharge damage to the electronics. In the second test, pixels can usually be tuned to the target threshold with a dispersion of 60 e, and a noise which ranges between 120 e for standard pixels to 300 e for long and ganged pixels (see Fig. 29).

1090 The second and third tests are also sensitive to bump bonding properties. Pixels that fail the tuning usually correspond to a cluster of merged bumps. In this case, several cell amplifiers are shorted together, resulting in reduced sensitivity to the injected pulse. In the case of an undepleted sensor, instead, normal pixels are affected by the large parasitic capacitance of the sensor, but pixels not connected to the detector stand out because the noise level remains low, independent of the bias voltage applied to the sensor side.
1095 An example of a module with such defects is shown in Fig. 30.

The testing of modules before and after the thermal cycles has been of importance. A problem in the potting¹²⁾ of wire bonds on the MCC was found, which resulted in unreliability of the wire bonds, which was corrected during the production. The comparison of bump damage between the initial assembly and

¹²⁾Dymax 9001 V3.1.

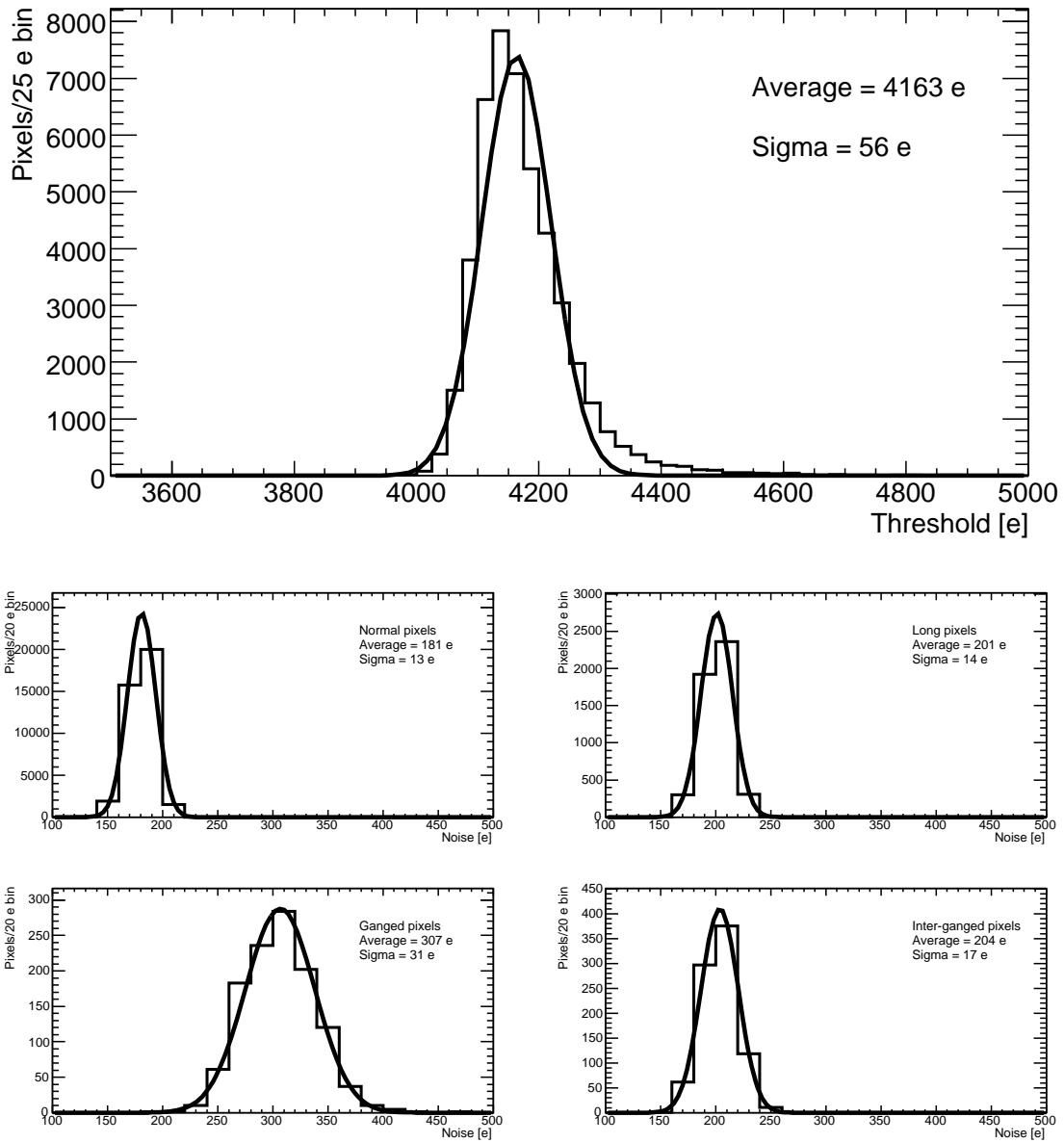


Figure 29: Threshold (top) and four noise (bottom) distributions - for different locations and types/sizes of pixels - of a typical module (normal, long, ganged, inter-ganged). The thresholds are uniform for the entire module.

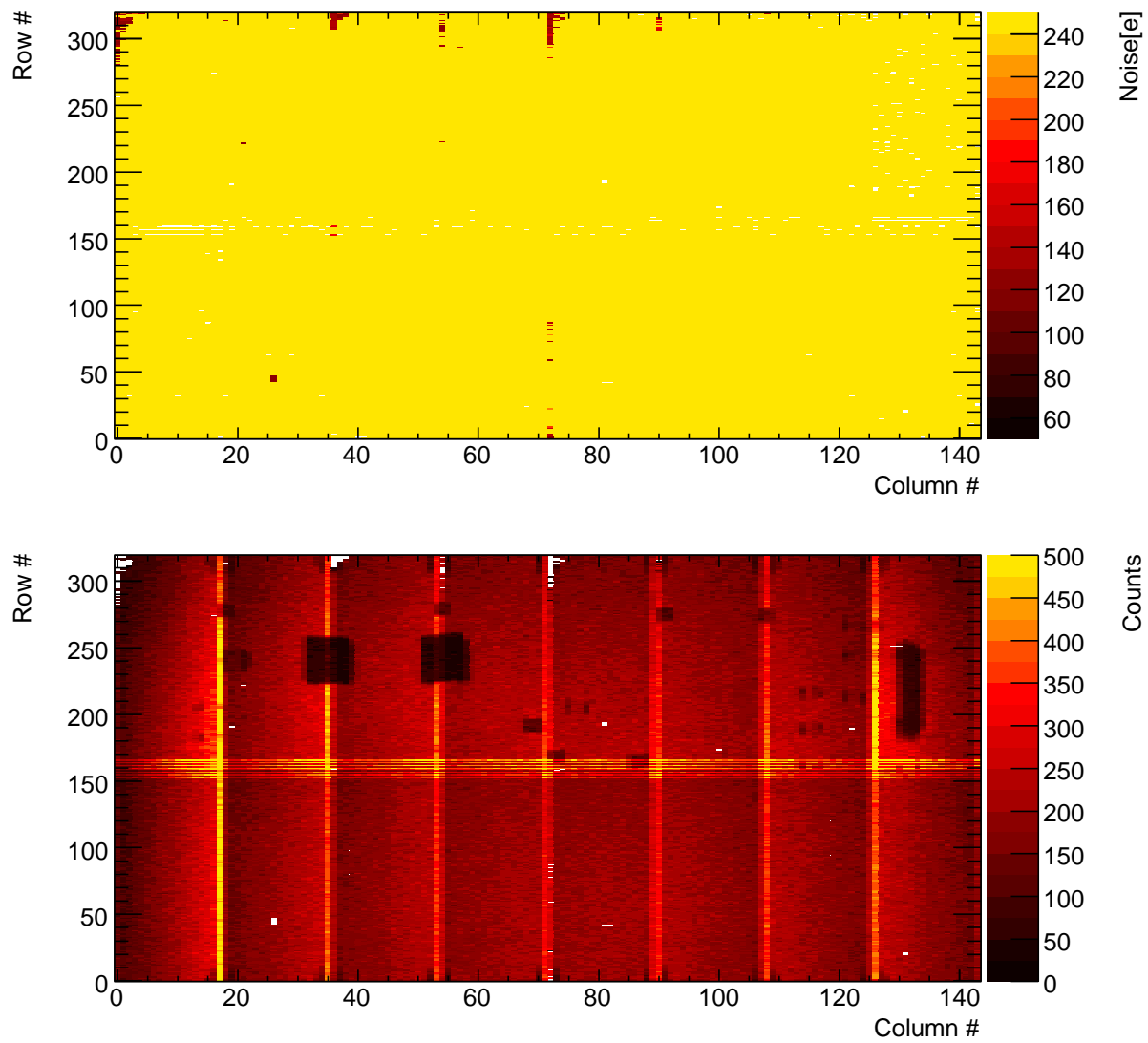


Figure 30: Noise distribution for an indium-bumped module without sensor bias (top). Disconnected regions are visible as low noise spots. For comparison below is a hitmap obtained with an ^{241}Am source.

1100 after thermal cycling, allows one to disentangle damage due to bad handling during the assembly, and
1101 damage due to weak bump bonds, for which there is a steady increase of disconnected bumps with time.
The full characterisation at the nominal operational temperature of -10°C included additional checks of
tunability and operational range:

- the MCC operation was checked between 1.6 and 2.5 V, showing a typical turn-on at 1.8 V;
- front-end IC operation was tested within wide ranges of analog and digital low voltage supply
1105 values (VDDA in the range 1.5-2.0 V, VDDD in the range 1.9-2.3 V);
- The amplifier feedback current was tuned so that the average ToT response to a minimum ionising
particle corresponded to 30 clock cycles: with the LVL1 trigger latency expected during operation,
this setting provided 99.5% efficiency in a test beam(see section 7);
- Timing measurements have been performed to check the timewalk performance of the FE elec-
1110 tronics when attached to the sensor. The overdrive needed to assign a signal to the correct beam
crossing is about 1000 e;
- A measurement with the 60 keV x-ray from an ^{241}Am source checked the sensors's response(see
Fig. 30).

The source measurement is especially relevant in assessing module quality, since, being self-triggering,
1115 it is very sensitive to noisy channels. The duration of the measurement is chosen to reach an expected
occupancy of at least 10 hits in every pixel channel. Therefore it is also very effective in uncovering
inefficient cells, due to merged or disconnected bumps.

The number of dead channels determined by the source test is the first entry in a ranking function
which has been chosen in order to evaluate module quality. Besides defective channels this function
1120 includes:

- a χ^2 -like term, describing how the analog performance of a module differs from the average one;
- penalties for anomalous values of the leakage current or module bowing, which may give problems
during operation;
- penalties for any repair operation performed on the modules.

1125 This ranking function was used for module selection for further assembly. The distribution of the ranking
function is displayed in Fig. 31. The bump in the ranking distribution around 300 corresponds to the set
of modules that needed a full rebonding of the MCC, because of the potting problem mentioned above.
The b-layer has been built using modules with ranking values lower than 60, corresponding to a channel
inefficiency better than 0.13%. Modules with ranking values higher than 1000 were not accepted for
1130 assembly.

Analysis of the ranking showed an overall equivalence of all the assembly sites, while pointing out a
clear difference between the two bump vendors. The main reason for the difference is the higher number
of disconnected bumps in the In-bumped modules. As stated before, a clustered set of disconnected
bumps may be the seed for a widening of a disconnected region. Because of this, a ranking penalty was
1135 added for each FE chip containing more than 30 disconnected bumps. In hindsight this penalty has been
found to be quite conservative, but it is the main reason for the tails in Fig. 31.

During the final phase of module production, when it was clear that there were a sufficient number
of spare bare modules, only the ones with clusters of less than four disconnected bumps were selected
for module assembly, resulting in an improvement of the module ranking.

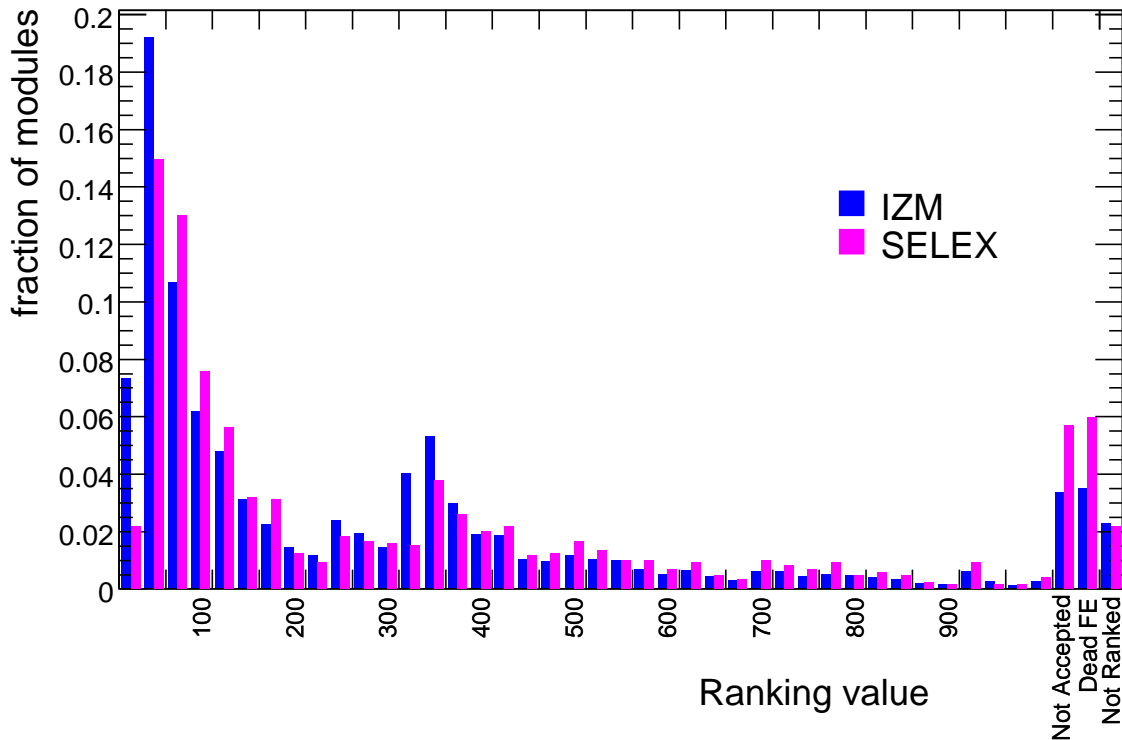


Figure 31: Module ranking distribution as described in the text.

1140 6.7 Production Yield

The production yield of bare modules is summarized in Table 6. Most losses were due to sensor damage, bad bumping and front-end IC damage.

Sensor damage usually is detected by an early breakdown voltage in the sensor tiles previously passing the sensor quality cuts. This loss rate was similar for both bump vendors and results in about 3% of the modules being rejected.

Bad bump bonding and FE damage were repairable according to the reworking procedures outlined previously. The failure rate and the possibility of reworking differed between the two bump vendors. In the case of bump problems, the solder-bump vendor often performed internal reworking after the in-house X-ray inspection, reprocessing the bumps. For indium bumps, there was no possibility to reprocess the bump deposition. In this case, if the damage was too widespread, the module was not submitted for reworking. This resulted in an overall higher failure rate for indium bumping.

FE damage was due to silicon shards trapped between the sensor and the FE chip, which, during flip-chip break the surface of the FE chips, resulting in shorts between the metal layers. The problem was more severe for indium-bumps, given the smaller bump height. Replacement of the FE chip usually resolved the problem, but manually removing the shards from the detector surface was needed to reach a good rework efficiency. The production yield of assembled modules is summarized in Table 7.

Modules that failed during the testing process were rejected due to mechanical damage observed after the assembly procedure, either induced by handling or because of weak parts which had passed the previous quality control steps.

Modules containing one or more FE which could not be operated were also discarded from the production path. A loss of about 1% was due to defects in the path from the MCC to the FE through the flex hybrid. For In-bumped modules, the additional yield loss is due to shorts on the FE, similar

	Indium		PbSn		Total	
	modules	yield	modules	yield	modules	yield
Assembled	1468		1157		2625	
Rejected	172	11.7%	35	3.0%	207	7.9%
Accepted	1296	88.3%	1122	97.0%	2418	92.1%
as delivered	1101	75.0%	1035	89.5%	2136	81.4%
after reworking	195	13.3%	87	7.5%	282	10.7%

Table 6: Bare module production yield.

	Indium		PbSn		Total	
	Modules	Yield	Modules	Yield	Modules	Yield
Assembled	1190		1122		2312	
Accepted	1025	86.1%	1075	95.8%	2100	90.8%
B-Layer quality	281	23.6%	445	39.7%	726	31.4%
not B-layer quality	744	62.5%	630	56.1%	1374	59.4%
Not accepted	165	13.9%	47	4.2%	212	9.2%
Ranking > 1000	68	5.7%	10	0.9%	78	3.4%
at least one dead FE	71	6.0%	10	0.9%	81	3.5%
could not complete testing	26	2.2%	27	2.4%	53	2.3%

Table 7: Assembled module production yield.

to the behavior observed on bare modules. These defects were concentrated on reworked modules and modules that underwent multiple shipments. They can be assumed to be the same defect of shards as seen on bare modules, which is not present after the initial bonding, but is finally produced by the additional mechanical stress in the module assembly. The difference in the ranking distribution between the Indium and solder bump modules is mainly due to regions of disconnected bumps, discussed in section 6.6. Overall the yield for module production exceeded the target, which was 90%, for each step in the bare module assembly, and subsequently for the full module assembly and characterisation.

7 Test Beam Studies

The performance of the pixel detector modules has been measured systematically in beam tests throughout their development. Initially, sensor properties were studied with single chip assemblies, namely reduced size sensors, which were read out by a single front-end chip. Later, full pixel modules were analysed in test beams. Results from test beams can be found in [53, 59, 73–82]. In this section we summarise beam measurements performed using the ATLAS pixel modules during final stages of development and qualification.

7.1 The Test Beam Setup

Test beam measurements were performed at the H8 beamline of the Super Proton Synchrotron (SPS) at CERN, using a beam of 180 GeV charged pions. A beam telescope [83] was used to track beam particles independently of the devices under test. The telescope consisted of four planes of double-sided silicon strip detectors, with perpendicular strips at 50 μm pitch, that provided a reference track with an extrapolation uncertainty of about 6 μm . Pixel assemblies under test were placed between the second

and third strip planes. Irradiated modules were inserted into a thermally insulated box, which maintained a temperature of about -7°C , as foreseen in ATLAS.

1185 A trigger was provided by the coincidence of three fast scintillators. For each event, a TDC measured the difference in time between the particle passage and the edge of a 40 MHz clock, seen by the pixel electronics. For each trigger, data from eight consecutive cycles were read out in order to study the pixel signal behaviour in a 200 ns window.

1190 For a fraction of the data taking, a high intensity beam was provided by the CERN SPS in order to study the efficiency of the readout architecture when the particle rate was comparable to that expected for the b-layer at the design luminosity of the LHC, namely $10^{34}\text{ cm}^{-2}\text{s}^{-1}$. In the beam center, the flux reached approximately $10^8\text{ particles/cm}^2/\text{s}$. At this particle flux, both the scintillator system and the microstrip telescope were inoperable. Data were instead collected with a random trigger and particle trajectories were reconstructed using four pixel modules.

1195 7.2 Irradiation of Tested Assemblies

A major design concern for the pixel detector is radiation tolerance during the lifetime of the experiment at the LHC. Single chip assemblies and modules were systematically irradiated before operation at the test beam with 24 GeV/c protons at the proton irradiation facility at the CERN Proton Synchrotron (PS) accelerator. The proton fluence was $2 \times 10^{15}\text{ cm}^{-2}$, corresponding to a 1 MeV neutron equivalent fluence of $1 \times 10^{15}\text{ n}_{\text{eq}}\text{cm}^{-2}$ and a dose of about 500 kGy. This corresponds to the expected dose resulting from 1200 five years of LHC operation at $10^{34}\text{ cm}^{-2}\text{s}^{-1}$ luminosity at the B-layer position. Throughout the irradiation, subsequent storage and test-beam operation, the modules were kept at about -7°C . Unless otherwise specified, the irradiated modules were operated at 600 V in the test beam, while the unirradiated ones were operated at 150 V.

1205 7.3 Event Reconstruction and Analysis

Tracks were reconstructed using information from the telescope microstrip detectors only (except during the high rate tests), in order to have an unbiased extrapolation of the tracks through the pixel detectors under test. Events were selected [84] with one and only one track reconstructed by the silicon microstrip telescope. Tracks were required to extrapolate to a fiducial region inside the pixel sensors (at least $40\text{ }\mu\text{m}$ 1210 from the edges of the detector). In addition, only events with a track fitting probability greater than 0.02 were kept. For each event selected, the intersection of the trajectory of the beam particle with the pixel detector was calculated.

1215 Neighboring pixel cell hits were clustered together. The bunch crossing identifier of the earliest pixel hit in the cluster was assigned to the whole cluster. The cluster position was typically reconstructed as the geometric mean position of the pixel cell centres. However, for the measurement of spatial resolution, the cluster position was reconstructed with a charge interpolation algorithm.

7.4 Measurements of Detection Efficiency

1220 The efficiency was computed requiring a pixel cluster near the intersection of the trajectory of the beam particle with the pixel detector and in the expected bunch crossing. The width of the window used to associate a cluster to a track was $\pm 0.2\text{ mm}$ along the short pixel side direction and $\pm 0.4\text{ mm}$ along the long pixel side direction.

1225 The efficiency was computed as a function of the time $t = t_0 + n \times 25\text{ ns}$ where t_0 is the TDC phase between the trigger and the edge of the clock operating the modules, and n is the bunch crossing ID of the cluster. Efficiency curves at perpendicular beam incidence are shown in Fig. 32a for an unirradiated module and in Fig. 32b for a module irradiated to $10^{15}\text{ n}_{\text{eq}}\text{cm}^{-2}$.

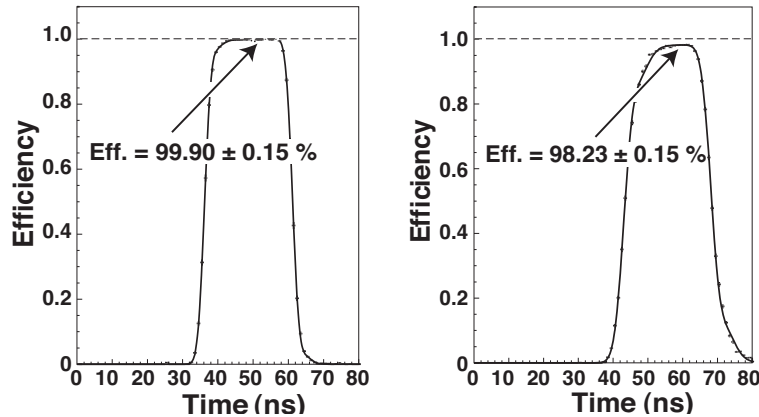


Figure 32: Detection efficiency at perpendicular beam incidence as a function of particle arrival time for an unirradiated module (a) and for a module irradiated to $10^{15} \text{ n}_{\text{eq}} \text{ cm}^{-2}$ (b).

At the LHC, only hits with a time stamp associated with a level 1 trigger are readout, i.e. only hits for which the leading edge rises in the 25 ns window corresponding to the clock cycle associated to the trigger are recorded. The position of this window can be tuned by setting the delay of the clock edge with respect to the bunch crossing time. The timewalk, i.e. the delay between the particle crossing and the leading edge of the signal passing the discriminator threshold, results in a spread in the time when hits are generated. It is therefore important to find the delay of the clock edge that maximises the number of hits collected within one clock cycle. Moreover, the performance should be stable for small variations of this delay and therefore a plateau in the relationship between efficiency and time delay is required.

A good detector should have a high efficiency for a significant range of clock phases. For the unirradiated detector of Fig. 32a, the plateau efficiency was 99.90% and this value was maintained for about 14 ns (plateau width). For the irradiated detector of Fig. 32b, the efficiency decreased to 98.23% but was still well above the ATLAS pixel module specifications for efficiency ($\geq 97\%$). The timing characteristics were affected by irradiation, resulting in slower rising and falling edges, leading to a narrower efficiency plateau. However, the rise time was only slightly degraded by irradiation and a large plateau was still obtained, with a width of about 9 ns.

A summary of measurements performed on several pixel production modules is given in Table 8, for data collected at normal incidence. The detection efficiency was 99.9% for an unirradiated module, while for the irradiated modules it varied from a minimum of 96.4% to a maximum of 98.4%, with an average and r.m.s of 97.8% and 0.7%, respectively. All irradiated modules had similar timing constants. The width of the efficiency plateau for the irradiated detectors was (9.7 ± 1.1) ns. No statistically significant difference was observed between the two sensor producers or the two bump-bonding techniques.

For each module, the efficiency losses were reported separately when due to missing hits (0-hits) or due to timing losses (out-of-time or late hits, i.e. hits recorded in subsequent bunch crossings). These hits cannot be assigned to the track and thus are a source of inefficiency. Two thirds of the efficiency losses, $(1.5 \pm 0.4)\%$, were typically in the 0-hits class and the rest $(0.7 \pm 0.3)\%$ in the timing loss class. Missing hits were due to various reasons: pixels not giving a signal at all (in turn due to detached bumps), noisy pixels masked at the readout (see below) and pixels collecting a signal lower than threshold. This last cause of efficiency loss as well as timing losses in irradiated detectors were related to regions of poor charge collection located near the bias grid described in section 5 [53].

module	510332	510337	510689	510704	510823	510852	510910	510929
irradiated	YES	YES	YES	YES	YES	YES	YES	NO
sensor producer	ON	CIS	ON	CIS	CIS	CIS	CIS	CIS
bonding	indium	indium	indium	indium	solder	solder	indium	indium
efficiency (%)	97.7	98.4	96.4	98.2	98.4	98.0	97.4	99.9
0 hits (%)	1.4	1.1	2.3	1.3	1.2	1.4	1.6	0.0
late hits (%)	0.9	0.5	1.3	0.5	0.4	0.6	1.0	0.1
plateau (ns)	8.6	9.2	8.5	9.3	10.2	11.4	10.8	13.9
masked (%)	0.0	0.1	0.0	0.0	0.3	0.0	0.0	0.0

Table 8: Summary of the pixel efficiency measurements performed at normal incidence with the standard bias voltage (150 V for modules without irradiation and 600 V for the irradiated modules). The first row provides the module identifier, the second whether it was irradiated before operation at the test beam, the third the producer of the sensor, and the fourth the bump-bonding technique. The subsequent rows report the detection efficiency, the fraction of losses due to undetected particles (0 hits), the time-walk losses (late hits), the width of the efficiency plateau and the fraction of pixels found noisy in the offline analysis (excluded from the efficiency analysis).

1255 7.4.1 Noise

Noisy pixels, identified prior to the test beam, were masked in the front-end chip configuration file. This procedure introduced an inefficiency which contributed to the 0-hit class. In addition, a few noisy pixel cells were also detected and masked during the offline reconstruction [77, 81], using the following procedure. In any given run the level-1 timestamp of pixel hits, correlated with a trigger, had a well defined value l_0 . In order to search for noisy pixel cells, hits with a level-1 either happening before l_0 or far after the most probable value l_0 ($l < l_0 - 1$ or $l > l_0 + 3$) were selected. If a pixel cell contributed either to more than three times to these events or for a fraction larger than 10^{-5} of the total number of events, then it was flagged as noisy and masked.

The track extrapolation was required to be at least $50 \mu\text{m}$ away from the pixel cells masked during the offline reconstruction. Thus the pixel cells masked by the offline reconstruction did not contribute to the inefficiency. The number of noisy cells was, however, very small. With the procedure described above, only two noisy pixels (out of 47232 i.e. 4×10^{-5}) were found in the unirradiated module. For all but one of the irradiated modules, the number of noisy, masked, pixel cells ranged from 0 (for three modules) to 32. One exceptionally noisy module (510704) had 129 noisy pixels, still only a fraction, 0.3% of the total number of pixels.

1265 7.4.2 Timing Studies

In ATLAS the clock phase can be adjusted for each individual pixel detector module, but it is the same for all the pixels of a module. Hence in order to achieve a good efficiency it is important that the timing differences (i.e. the spread of the t_0 values of the efficiency curve) between different pixels of a module is smaller than the width of the efficiency plateau. The timing differences between different types of pixels (ganged, long and standard) and between the 16 front-end chips of a module were found to be smaller than 2 ns (see Table 9). Since this difference is smaller than the width of the efficiency plateau, it should have a negligible effect on the module efficiency at the LHC.

pixel type	standard	long	ganged
ε (%)	98.0	99.1	97.7
t_0 (ns)	11.7	12.4	13.7
plateau (ns)	11.7	10.8	11.3

Table 9: Detection efficiency and timing parameters measured for different types of pixels (standard, long and ganged, see section 5 for their description) for a module irradiated to 10^{15} $1 \text{ MeV n}_{\text{eq}}\text{cm}^{-2}$.

7.4.3 Detection Efficiency and Bias Voltage

1280 The in-time efficiency for an irradiated module is reported in Fig. 33a as a function of operating bias voltage. For low values of bias voltage, the collected charge is small since the detector is not fully depleted. Hence the maximum efficiency is smaller. The effect of time-walk is also evident: when the collected charge is smaller, the hits are detected later and the efficiency curve moves to the right. The lower amount of collected charge affects also the timing characteristics of the module. As much as the
 1285 detector bias voltage decreases, then less charge is collected, the module shows clearly slower rising and falling edges. As a consequence, the efficiency plateau is much narrower. The peak efficiency is reported as a function of the bias voltage in Fig. 33b for two modules irradiated to 10^{15} $\text{n}_{\text{eq}}\text{cm}^{-2}$. In agreement with the results on the collected charge, full efficiency is reached at 500 V when the detector is fully depleted.

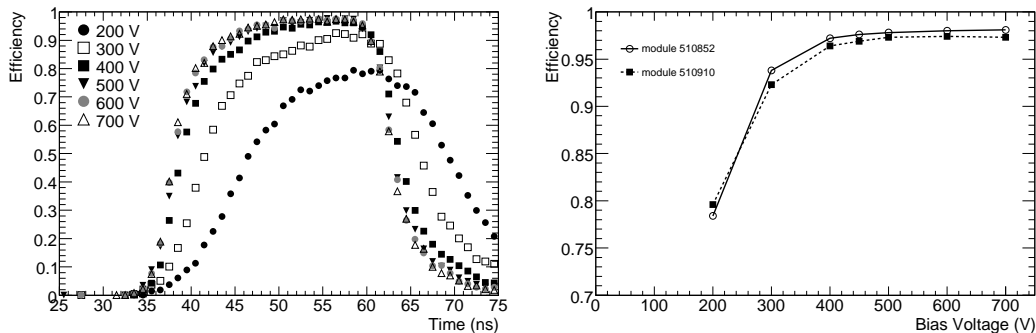


Figure 33: (a) Detection efficiency as a function of time in ATLAS pixel modules irradiated to 10^{15} $\text{n}_{\text{eq}}\text{cm}^{-2}$, for different values of the operating bias voltage. (b) Maximum detection efficiency as a function of operating bias voltage in ATLAS pixel modules irradiated to 10^{15} $\text{n}_{\text{eq}}\text{cm}^{-2}$.

1290 7.4.4 Detection Efficiency and Incidence Angle.

In ATLAS, tracks will not generally be perpendicularly incident to a pixel module plane. Consequentially, the influence of incidence angle on module performance needs to be evaluated. When particles traverse the detector at an angle, the charge released in the sensor is spread over a larger area and is usually divided among more than one pixel cell. This has two competing effects on the detection efficiency.
 1295 Because of charge sharing, each individual pixel has a lower signal. This increases the hit losses due to the time-walk. As discussed above, at normal incidence most of the hit losses occur when the particle transverse the detector in a spatially limited region of the pixel cell. This region is close to the edge between two pixel cell, where the bias grid is located. In this region charge sharing occurs also at normal incidence because of diffusion, and the charge collection efficiency is low. When the particle incidence

1300 angle is in the range of 10° , the charge released in the sensor is spread over a length much larger than the region with poor charge collection, so that the overall charge collection efficiency is higher.

Table 10 presents the detection efficiencies for particles at 0° and 10° for both irradiated and unirradiated modules. The results indicate that the spread of charge over a larger region actually dominates so that the efficiency is larger when the detectors are tilted. The results reported in this paper, which are mostly obtained with measurements at normal incidence, are thus conservative.

module	510852	510910	510929
normal incidence	98.0%	97.4%	99.9%
10°	98.4%	98.5%	>99.93%

Table 10: Detection efficiency measured for the unirradiated module 510929 and the irradiated modules 510852 and 510910, at two values of incidence angles.

1305

7.4.5 Efficiency in a High Intensity Beam

Beam tests of production modules were performed with a high intensity pion beam at various beam intensities, up to the value foreseen for the innermost pixel layer at the design LHC luminosity of $10^{34} \text{ cm}^{-2} \text{ s}^{-1}$, in order to test the readout system in high occupancy conditions. At each intensity, data were taken with different configurations of the front-end chip. There are several mechanisms which can induce hit losses, depending on the rate of particles crossing the detector:

- If additional charge is deposited while the discriminator is above threshold, it is added to the initial one and the second hit is lost;
- After the discriminator goes below threshold, the pixel cell is unable to accept new hits until the sparse scan logic has transferred the hit data to the end of column memory buffers;
- Finally, if all the memory buffers are occupied when the hit is transferred, it is lost due to lack of memory space

The first effect depends on the local occupancy of the pixel cell, i.e. the probability to get a hit in a bunch crossing, and on the average Time over Threshold response for a charged particle.

1320 The other effects are sensitive to the hit rate per column pair, since all pixel cells in a column pair share the same sparse scan logic and memory buffer. Therefore results are quoted as a function of the occupancy per column pair (cp) per bunch crossing (bx). The expected occupancy ¹³⁾ for the innermost layer at the LHC at $10^{34} \text{ cm}^{-2} \text{ s}^{-1}$ is 0.17 hits/cp/bx, which is approximately equivalent to $10^8 \text{ hits/cm}^2/\text{s}$, with an average multiplicity of 1.5 hits per track. At the test beam, the pixel detection efficiency was studied for the entire range of occupancies expected at the LHC and beyond.

1325 A summary of efficiency measurements are reported in Table 11 with an indication of the maximal occupancy per column pair. With the standard front-end electronics settings, the detector efficiency of irradiated detectors remains unchanged and close to 98% up to an occupancy of 0.24 hits per clock cycle per column pair. This value exceeds by about 40% the maximum occupancy foreseen.

1330 At larger occupancies, a small inefficiency arises from saturation of the end-of-column buffers of the front-end electronics chip. This saturation is properly flagged by the FE Buffer Overflow flags. Removing the events with the error flag restores the hit efficiency to its value at a lower intensity. The maximum value of column pair occupancy reached at the test beam was 0.27 hits per clock cycle for

¹³⁾These figures can be obtained rescaling the results documented in Ref. [3] to take into account the increase of the pixel long pitch from $300 \mu\text{m}$ to $400 \mu\text{m}$ and have been confirmed by simulation studies done with the updated layout.

irradiated modules, and 0.30 hits per clock cycle for the module without irradiation. The corresponding efficiencies were about 96% for irradiated modules and 89.8% for the not irradiated module.

Non-standard settings of the front-end electronics were also studied. When the latency is increased from 130 to 250 clock cycles, the intensity at which hit losses are observed is reduced by a corresponding factor. The reduction of the frequency of the column pair readout clock from 40 MHz to 20 MHz results in a sharp efficiency loss when the occupancy exceeds 0.14 hits per clock cycle per column pair, because some pixel hits are not transferred to the end-of-column buffers within the latency of 130 clock cycles. With the usual 40 MHz operation, hit losses due to this mechanism are not expected unless the occupancy is larger than twice this value (0.28 hits per clock cycle per column pair). The efficiency also decreases when the amplifier feedback current is changed, so that the peak of the ToT distribution increases. The effect is due to the passage of a second particle through a pixel cell before the signal produced by the first event has fallen below the discriminator threshold. The efficiency loss is compatible with expectations and it is very small. For an average ToT of 15 clock cycles and the nominal b-layer occupancy, the efficiency loss due to this effect is 0.75%.

The test beam results demonstrate that at the hit rates expected for the b-layer at the design LHC luminosity the pixel detector modules have an efficiency larger than 98%. However, it should be noted that while the testbeam did simulate the high rate of hits in the modules, it did not simulate the high Level-1 rate and data transmission rate that would be expected at LHC, so it is only a partial simulation of operation at the highest luminosities. The effect of possible inefficiencies due to untested parts of the data acquisition chain will, however, appear as a reduction of the global DAQ live-time and not as a specific reduction of the pixel detector efficiency.

Also, the b-layer hit detection efficiency may be reduced by a few per cent if the occupancy significantly exceeds the nominal value. This may occur for several reasons, such as track loopers at low momenta, a pp cross section at the LHC larger than the current estimate, or a machine luminosity exceeding the design value. Very large values of occupancy will also be reached during the heavy ion runs.

Occupancy irradiated [hits/cp/bx]	ϵ 510689	ϵ 510852	ϵ 510910	Occupancy not irr. [hits/cp/bx]	ϵ 510929	ToT [bx]	lat. [bx]	read. [MHz]	hit dupl.
0.030-0.043	0.981	0.984	0.986	0.040	0.988	15	130	40	NO
0.069-0.084	0.981	0.984	0.985	0.082	0.986	15	130	40	NO
0.100-0.124	0.980	0.982	0.983	0.124	0.983	15	130	40	YES
0.199-0.202	0.978	0.982	0.985	0.239	0.984	15	130	40	NO
0.269-0.282	0.964	0.967	0.944	0.306	0.898	15	130	40	YES

Table 11: Measurements of detection efficiency performed with a high intensity beam. The first column reports the average occupancy of the irradiated modules for the column pair on which the beam was most intense. The range corresponds to the fact that due to the different position of each module relative to the beam, the occupancy varies slightly from module-to-module. The second to the fourth columns report the measured detection efficiency of the three modules irradiated to $10^{15} \text{ n}_{\text{eq}} \text{cm}^{-2}$. The fifth and the sixth column report, respectively, the occupancy and the efficiency of the unirradiated module. The last columns report the front-end electronics settings, in this order: the ToT peak tuning value and the latency, the column readout frequency, and whether hit duplication was on.

1360 7.5 Spatial Resolution

We describe here measurements of spatial resolution performed on pixel modules equipped with the final production sensors and the final or nearly final readout electronics (the FE-I family of readout chips - see section 4). Measurements done with older prototypes have been published elsewhere [73–76].

1365 Spatial resolution is mainly determined by the pixel cell size, the choice between analog or digital readout and the degree of charge sharing between adjacent pixels. Charge sharing is affected by intrinsic sensor properties (e.g. inter-pixel capacitance and pixel capacitance to the backplane), operational parameters (such as reverse bias operating voltage and radiation damage, etc.) and by parameters related to electronic readout (threshold, crosstalk, charge resolution, etc.). A substantial role is also played by the incident particle track angle and by the $\vec{E} \times \vec{B}$ effect.

1370 If there is no charge sharing, all of the charge carriers locally generated around the incident particle trajectory are collected on a single pixel (single hit clusters) and the spatial resolution is related to $\sigma = L/\sqrt{12}$, where L is the pixel pitch. If the liberated charge is collected on neighbouring pixels (two or more pixel clusters), charge interpolation becomes possible, which provides for improved resolution. The charge sharing between adjacent pixels was studied using tracks at normal incidence. The width of
 1375 the charge sharing region ranged between approximately ± 3 and $\pm 7 \mu\text{m}$ depending on the threshold, depletion depth and bias voltage (which influence diffusion).

When a particle is incident within the charge sharing region, it may generate two-pixel-clusters. This depends on sensor charge collection efficiency and the electronics threshold. Two different algorithms were used to reconstruct the spatial position of two-pixel-clusters. A *digital* algorithm, which uses the center position between the two pixels, and an *analog* algorithm that corrects the binary position just described using an interpolation of the charge collected by the two pixels. Since it was observed that the ratio of the charge collected on the right-hand side pixel (Q_r) over the total charge collected by the two pixels $\eta = Q_r/(Q_l + Q_r)$ (where Q_r and Q_l are the charges collected by the right-hand side and left-hand side pixels in the cluster, respectively) had a dependence on the position of the passing particle, the following interpolation was adopted [85]:

$$x_{\text{an}} = x_{\text{dig}} + \frac{\Delta}{N_0} \int_0^{\eta} \frac{dN}{d\eta} d\eta \quad (1)$$

where x_{an} and x_{dig} are the spatial positions reconstructed by the analog and digital algorithms respectively. This formula assumes that N_0 particles are spread uniformly over an interval Δ that is the width of the region within which charge sharing occurs.

1380 An equivalent procedure was adopted for multi-pixel clusters. These occur when particles traverse the pixel sensor at an angle. For inclined particles, the charge is collected over a region approximately given by $D \times tg(\alpha)$, where D is the sensor depletion depth, and α is the angle between the particle trajectory and the normal to the sensor surface. Charged particles with large incident angles produce signals on many pixels and the average charge per pixel decreases, despite the longer trajectory in the
 1385 silicon. Since only the signal amplitudes on the edge pixels in the clusters carry information on the position of the passing particle, the digital and the analog algorithms described above were used to reconstruct the coordinate but only taking into account the first and the last pixel in the clusters [74]. Referring to (1), Δ depends on angle, cluster multiplicity and sensor design and is extracted from a fit to data for each configuration.

1390 As the track length under a pixel is geometrically limited by $p/\sin \alpha$ (p being the pixel size), charges on a pixel exceeding $Q_{\text{cut}} = \lambda p/\sin \alpha$ (where λ is the mean number of electrons generated per unit path length) are due to energy loss fluctuations and δ electrons. The impact of these fluctuations on resolution was reduced by setting pulse heights exceeding Q_{cut} to Q_{cut} , when computing η .

1395 In what follows, x describes the short ($50 \mu\text{m}$) and y the long ($400 \mu\text{m}$) pitch dimension of the pixel assembly.

7.5.1 Determination of the Telescope Extrapolation Uncertainty

Spatial resolution was determined by computing the residuals between the coordinate measured by the pixel detector and that predicted by the silicon microstrip telescope. The extrapolation uncertainty depends on many parameters, e.g. the position of the microstrip planes and of the pixel detector under study, the microstrips intrinsic resolution, the amount of material along the beam path etc. Telescope resolution was improved by applying a tighter selection on the track reconstruction χ^2 probability.

The resolution of the telescope can be evaluated using the residuals for both single pixel and double pixel clusters at normal incidence. An example of these distribution is shown in Fig. 34. Single pixel clusters occur when incident particles cross the pixel central region of width $L=p-2*\Delta$. The distribution of their residuals can be parametrised as a uniform distribution of width L , convoluted with a Gaussian distribution that takes into account the resolution of the silicon strip telescope, threshold effects and δ -rays [82]. An alternative method to estimate telescope resolution is a Gaussian fit to the two-pixel cluster analog residuals whose width is expected to be dominated by the telescope uncertainty.

The two methods give values in statistical agreement for the telescope resolution. At 0° , the telescope resolution values between 3 and 6 μm were measured, depending on the different amount of material along the beam line. At higher angles, slightly worse values were measured, due to the projection on the pixel detector plane (which yields a telescope resolution proportional to $1/\cos \alpha$) and the presence of more material along the beam when detectors are tilted.

The quoted values are the standard deviations evaluated by fitting the residual distributions with a Gaussian function. These are less sensitive to statistical fluctuations than the rms and give a reasonably good description of the width of the distributions even when the distributions are not Gaussian (as occurs at angles at which a limited charge sharing is present).

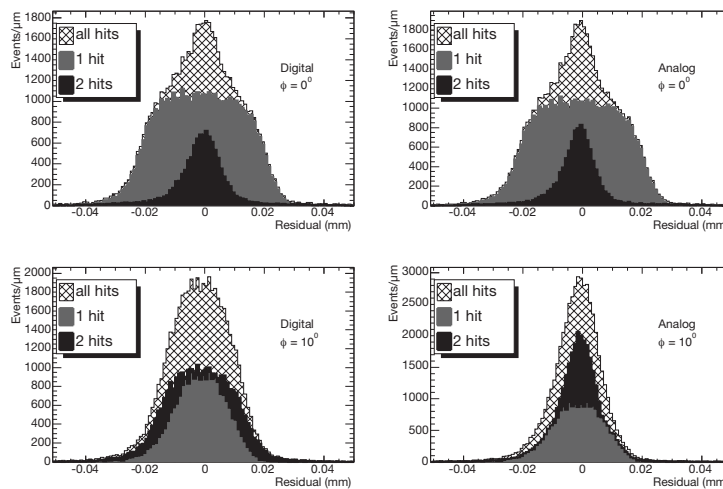


Figure 34: Left: residuals between the position measured by an unirradiated pixel detector (LBL22) using the digital algorithm and by telescope, for two different angles of incidence of the beam (0° upper plots, 10° lower plots). Different colors indicate different size of the pixel clusters. Right: residuals between the position measured by the pixel detector using the analog algorithm and by the telescope. After subtraction of telescope extrapolation uncertainty, r.m.s. are 12.2 and 12.1 μm at 0° , for digital and analog algorithms respectively, 10.1 and 7.2 μm at 10° .

7.5.2 x-Spatial Resolution at Normal Incidence

At normal incidence, mainly single-pixel and double-pixel-clusters occur. The resolution is determined by their relative abundance and is dominated by the single-hit cluster resolution. The combined distribution of single- and double-pixel clusters for the FE-I2 module shown in (Fig. 34, upper plots) has a standard deviation of $12.2 \mu\text{m}$.

Module	Irradiated	1 hits (%)	2 hits (%)	Digital resolution (μm)	Analog resolution (μm)
GE04	NO	76.3	22.2	11.8	11.7
LBL20	NO	77.0	21.5	11.6	11.4
LBL22	NO	77.0	21.1	12.2	12.1
IZMc	YES	70.1	28.8	10.6	10.3
AMS310b	YES	67.8	30.9	10.0	9.6
510929	NO	78.6	19.9	10.7	10.6
510910	YES	76.7	19.2	11.1	10.9
510689	YES	82.5	14.4	11.8	11.7

Table 12: Measurements of spatial resolution performed at normal incidence. The fraction of single and double pixel clusters is also reported. Telescope extrapolation has been subtracted.

The relative weights of single-pixel and double-pixel-clusters are listed in Table 12, where the results for eight FE-I modules are presented. There is not a great difference between analog and digital resolutions or between unirradiated and irradiated modules. Note that the latter were still fully depleted at the operating bias voltage of 600 V (see section 7.6).

7.5.3 x-Spatial Resolution as a Function of the Angle of Incidence

The dependence of the spatial resolution on the angle (α) of the incident particle with respect to the normal to sensor surface was studied. The standard deviations of the all-cluster residual distributions are shown in Fig. 35. The data were not corrected for the silicon microstrip telescope extrapolation uncertainty.

As the tilt angle is increased, the fraction of double-pixel clusters increases, their residual distribution gets wider and the single-pixel cluster distribution narrower. This is a consequence of single-pixel clusters occurring in a more restricted region.

The best digital resolution is obtained when the two distributions are equally populated. At any given angle, about 98 % of clusters are formed from only two multiplicities (1 and 2, 2 and 3 and so on, depending on the angle). When they are equally populated the digital resolution is of the order of $p/2/\sqrt{12} = 25 \mu\text{m}/\sqrt{12}$. When the angle is such that nearly all of the events belong to one multiplicity only, the digital resolution is of the order of $p/\sqrt{12} = 50 \mu\text{m}/\sqrt{12}$. Then the digital resolution as a function of angle (Fig. 35a) oscillates between these two extreme values.¹⁴⁾

The spatial resolution obtained with the analog algorithm (Fig. 35b and Fig. 34, down right) is always better than the corresponding digital resolution once the incidence angles are larger than 0° . The charge interpolation used by the analog algorithm allows one to obtain a dramatic improvement in the spatial resolution for clusters with two or more pixels. The best resolution value occurs when the proportion of single-pixel clusters becomes negligible. This occurred between 10° and 15° . The best resolution for the unirradiated devices was $6.6 \mu\text{m}$ before correction for the telescope resolution. The best resolution for a device irradiated to $10^{15} \text{ neqcm}^{-2}$ was $9.1 \mu\text{m}$ before correction for the telescope resolution. It should

¹⁴⁾The silicon microstrip telescope extrapolation uncertainty was not subtracted.

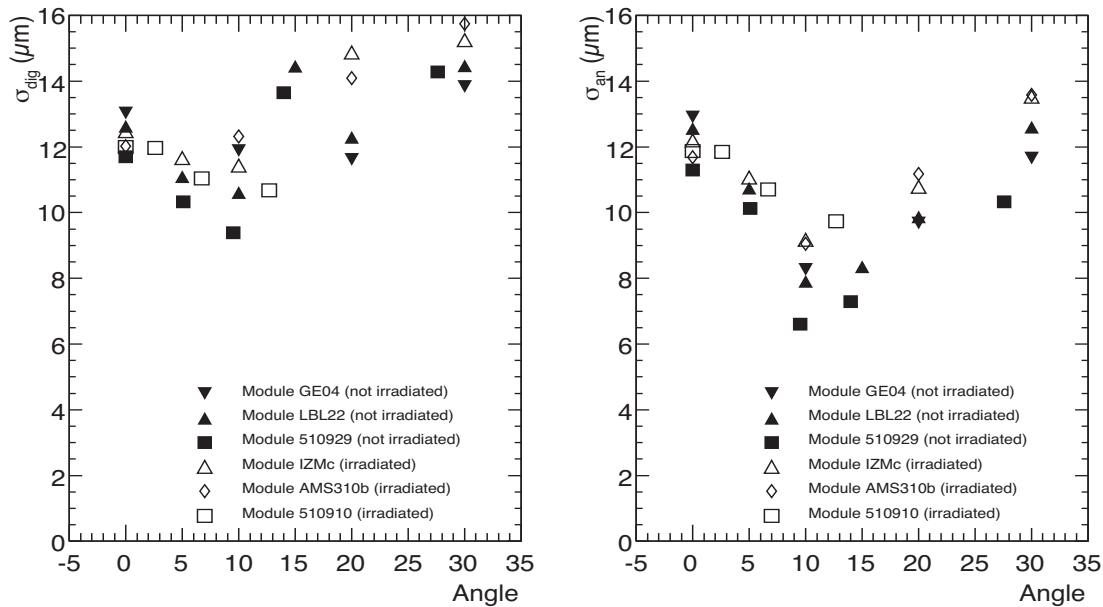


Figure 35: Measured digital (a) and analog (b) resolution as a function of the angle of incidence of the beam, without subtraction of telescope extrapolation uncertainty. The charge interpolation used by the analog algorithm allows to obtain a dramatic improvement in the spatial resolution, except for small incidence angles when single pixel clusters are dominant.

1450 be noted that the spatial resolution is not significantly degraded post-irradiation, showing that there are no inhomogeneities in the sensor after irradiation. The differences in spatial resolution before and after irradiation are completely explained in terms of (a limited) reduced charge collection efficiency. As the angle of incidence increases further, the charge collected by every pixel is reduced and energy loss fluctuations introduce inefficiencies in the first and last pixel in the cluster, thus degrading the resolution.

7.5.4 Lorentz Angle

1455 In the presence of an electric field and a magnetic field, the charge carriers liberated by a passing particle within silicon drift along a direction at an angle Θ_L (Lorentz angle) with respect to the electric field direction, due to the $\vec{E} \times \vec{B}$ effect. This will happen in the barrel of the pixel detector, where the electric and magnetic field are at right angles (but not in the disks where they are parallel).

1460 The Lorentz effect produces a systematic shift between the position of the signal induced on the electrodes and the position of the track. While this shift is in principle absorbed by the alignment correction, the knowledge of the Lorentz angle will help the understanding of the alignment corrections and their time dependence. In addition, the Lorentz effect is expected to change the angular dependence of the spatial resolution. The Lorentz angle was measured using test beam data and a detailed report of these measurements is published elsewhere [73]. A short summary is given here.

1465 The Lorentz angle for irradiated and unirradiated sensors was determined by measuring the minimum of the mean cluster size plotted as a function of the angle of the incident beam particles. The minimum occurs for an incident angle equal to the Lorentz angle. The results of the measurements are reported in Table 13. The measured values are compared to the predictions of a model [73, 76] which computes

the Lorentz angle as a function of the magnetic field and mobility inside the sensor, the latter depending on the temperature and the electric field. A good agreement is found. Irradiated sensors have a lower Lorentz angle because a larger bias voltage is applied on a smaller depletion depth. A discussion of the Lorentz angle values expected for the pixel detector during operation in ATLAS can be found in [86].

Fluence ($n_{\text{eq}}\text{cm}^{-2}$)	0	$0.5 \cdot 10^{15}$	$0.5 \cdot 10^{15}$	10^{15}	10^{15}
Bias voltage (V)	150	150	600	600	600
T (K)	300	264	264	264	264
Magn. field (T)	1.48 ± 0.02	0.95 ± 0.05	0.95 ± 0.05	1.01 ± 0.05	0.74 ± 0.05
Θ_L (meas.) ($^\circ$)	$9.0 \pm 0.4 \pm 0.5$	$5.9 \pm 1.0 \pm 0.3$	$2.6 \pm 0.2 \pm 0.3$	$3.1 \pm 0.4 \pm 0.6$	$2.7 \pm 0.4 \pm 0.4$
Θ_L (th.) ($^\circ$)	9.3 ± 0.4	3.7 ± 0.5	2.7 ± 0.2	2.1 ± 0.2	1.8 ± 0.2

Table 13: Lorentz angle measurement results.

The effect of the Lorentz force on the spatial resolution is expected to be a shift of the angular dependence of the resolution on the incidence angle by an amount equal to the Lorentz angle. This has been verified with the test beam data, namely the spatial resolution as a function of incidence angle in the presence of a magnetic field was indeed similar to that obtained without the magnetic field, once the angular shift was taken into account [73, 76].

7.6 Depletion Depth of Irradiated Sensors

The depletion depth of irradiated sensors is an important parameter, since its value affects detectors performance. It has therefore been studied in detail. The measurement of the depletion depth was performed according to the technique described in [73–75]. Data were taken exposing the pixel assemblies to the beam at an angle of 30° w.r.t. the normal to the pixel plane and then the average depth of charge deposition under each pixel was computed and histogrammed. The depth of charge collection region was extracted from the upper edge of this distribution. In Figure 36 the depletion depth measurements of the irradiated assemblies are shown as a function of the applied bias voltage and for three different annealing protocols¹⁵⁾. In agreement with expectations made using the radiation damage parameters of the ROSE Collaboration [48], at 600 V, 250 μm thick DOFZ silicon detectors are almost fully depleted after the full LHC dose after 10 years of operation and independently of their annealing history.

7.7 Charge Collection in Irradiated Sensors

Charge collection of irradiated sensors is an important characteristic, since its value affects detector performance, both in terms of efficiency and spatial resolution. It has therefore been measured in detail. In Figure 37, the average charge of pixel clusters with a normal incidence beam is shown as a function of operating voltage for irradiated assemblies. It can be noted that maximal efficiency in charge collection is reached at about 400 V by the detector annealed at the minimum value of depletion voltage V_{fd} (expected $V_{fd} = 350$ V) and its charge collection efficiency does not increase at larger operating voltages, i.e. at larger electric fields. This is related to the choice of n-side readout. Since the pixel width is much smaller than the substrate thickness, most of the signal is induced by charges moving near the n-side [87], where the electric field has a maximum and the drift velocity is already saturated (i.e. independent on the electric field) at 400 V. For the detectors annealed at the end of lifetime at LHC, the plateau in charge collection

¹⁵⁾The three annealing scenarios considered in the measurement and reported in the figure are: no significant annealing; the annealing which results in the minimum value of depletion voltage for a given thickness (at the end of the so called beneficial annealing); 25h of annealing at 60°C , roughly corresponding to the total annealing foreseen for the pixel detector sensors during their operating lifetime at the LHC.

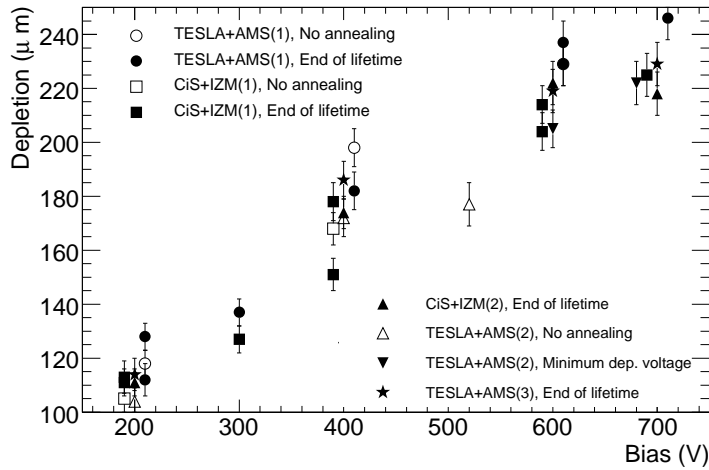


Figure 36: Measured depletion depth as a function of operating voltage for DOFZ silicon pixel detectors after irradiation of $1 \times 10^{15} \text{ n}_{\text{eq}}\text{cm}^{-2}$. The applied annealing protocol is indicated, as well as the sensor manufacturer (CiS and ON) and bump bonding (AMS and IZM) producers. At a bias voltage of 600 V or larger, the sensors are almost completely depleted.

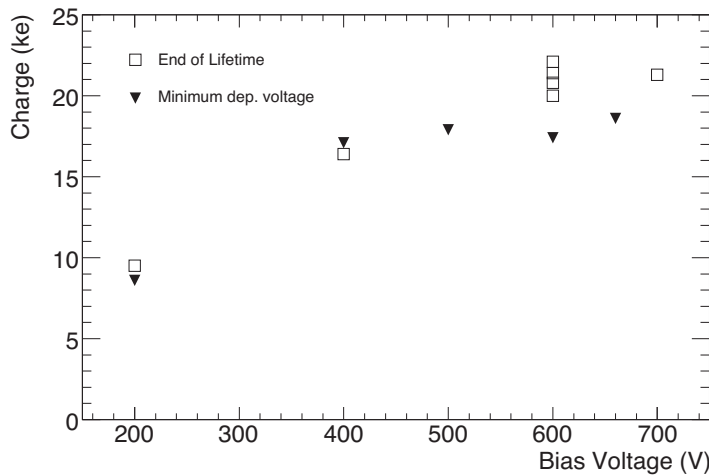


Figure 37: Average collected charge as a function of operating voltage for DOFZ silicon pixel detectors after irradiation of $1 \times 10^{15} \text{ n}_{\text{eq}}\text{cm}^{-2}$. The four end-of-lifetime values shown at 600 V correspond to four different modules.

is reached at 600 V (i.e. at their V_{fd}). One can notice that at the foreseen operating voltage of 600 V, the charge collected by the detectors will be well above the threshold of FE electronics. One should note the different asymptotic values of charge collection efficiency for the two annealing protocols: at 600 V or higher operating voltage, where irradiated sensors were completely depleted, the average Charge Collection Efficiency was $(87 \pm 14) \%$ (w.r.t. the one of unirradiated sensors operating at 150 V) for sensors annealed for 25h at 60° (end of lifetime at LHC) and $(72 \pm 14) \%$ for the sensor annealed to minimum V_{fd} . The errors come from the uncertainty in the charge-ToT calibration. Since detectors

were completely depleted as discussed above (see depletion depth measurements), this inefficiency is completely due to charge trapping.

7.8 Charge Trapping in Irradiated Sensors

Data taken at an angle of 30° between the track and the normal to the sensor surface were also used to measure charge trapping with a new method described in [56, 78]. Because of trapping, the deeper the track segment subtended by a pixel, the lower the charge it collects. In Fig. 38 the charge collected by a pixel is reported as a function of the average track segment depth for an unirradiated and two irradiated detectors. In the unirradiated detector the collected charge is constant as long as the track segment subtended by the pixel is entirely within the sensor. In the two irradiated detectors, charge trapping results in a decrease of charge collection efficiency with the depth. This effect is more severe in the detector annealed to the minimum in V_{fd} than in the four detectors annealed to the end-of-lifetime scenario.

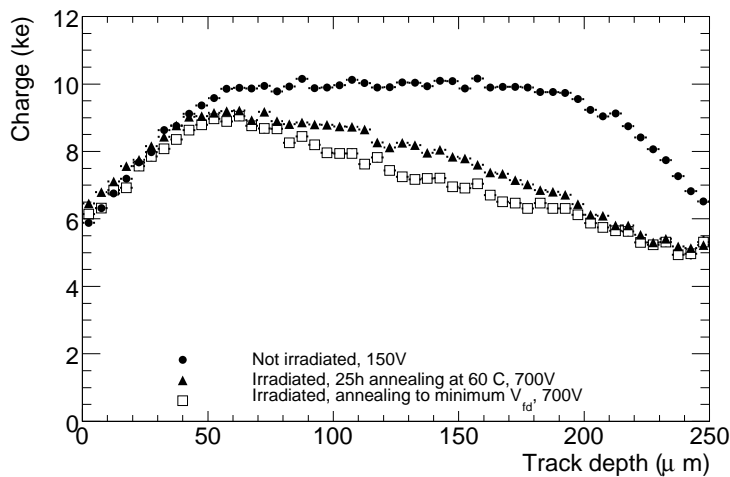


Figure 38: Pixel charge as a function of track depth for three fully depleted DOFZ silicon pixel detectors: one unirradiated operated at 150 V and two irradiated at $1 \times 10^{15} \text{ n}_{\text{eq}}\text{cm}^{-2}$ with two different thermal annealing levels and operated at 700 V.

In order to be independent of the charge scale uncertainty, the charge collection profiles were normalized and only the shape of the distribution was used to investigate trapping effects. In order to extract the charge carrier lifetimes, these experimental charge collection profiles were compared to the output of a numerical simulation [87], where the interactions of charged particles with silicon were simulated using the Geant4 package [88]. The drift of holes and electrons in silicon was described in detail, taking into account diffusion and trapping, and using parametrisations of data for the charge drift properties [89]. The signal on the pixels was computed using the Ramo theorem [90], and taking into account the electronics threshold, noise, and cross-talk.

The resulting values for the charge trapping lifetimes (assuming the same lifetime for holes and electrons) and the radiation-damage parameter $\beta = 1/\tau\Phi$ are reported in Table 14. The measurements were performed at 700 V bias voltage in order to be well above V_{fd} . The second systematic uncertainty on trapping lifetimes is associated with the approximation of a constant electric field inside the sensor that is correlated for different sensors. While it is difficult to precisely evaluate this correlation, there is some evidence of a dependence of the trapping probability on annealing: trapping appears to be less

Sensor	annealing	τ (ns)	$\beta(10^{-16}\text{cm}^2\text{ns}^{-1})$
A	25h at 60°C	$5.5 \pm 0.7 \pm 0.8$	1.7 ± 0.4
B	25h at 60°C	$3.4 \pm 0.4 \pm 0.3$	2.7 ± 0.4
I	25h at 60°C	$4.1 \pm 0.5 \pm 0.3$	2.2 ± 0.3
T3	25h at 60°C	$4.8 \pm 0.6 \pm 1.4$	1.9 ± 0.6
average	25h at 60°C	$4.1 \pm 0.3 \pm 0.6$	2.2 ± 0.4
T2	minimum V_{fd}	$2.3 \pm 0.2 \pm 0.8$	4.0 ± 1.4

Table 14: Measured values of charge trapping lifetime and radiation damage parameter β for five irradiated detectors at 700 V bias voltage, assuming equal lifetime for electrons and holes.

severe after 25h of annealing at 60°C than for sensors annealed to the minimum of V_{fd} . after beneficial annealing only.

7.9 Combined Test Beam

1535 A dedicated effort to understand the combined performance of a complete slice of the ATLAS detector, from the pixel detectors to the outermost stations of the muon chambers, took place in 2004 with the large-scale combined test beam exercise [91]. The setup included six pixel modules, placed inside a 1.4 T magnetic field. The setup integrated hardware and software in as close as possible fashion as they will be in the full ATLAS detector. The combined test beam ran in 2004 and provided an opportunity to
1540 test the software and to study the tracking performance using real data.

The pixel detector performed well in the combined test beam, producing good quality data. Using ATLAS offline software, tracks were successfully reconstructed. Residuals obtained after alignment showed agreement with simulation. The impact parameter and z_0 resolutions were comparable with what is expected in the experiment.

1545 The use of standard ATLAS components in the software chain was successful and the combined test beam was a valuable development test bed for the online and offline software. This effort has led to first sets of calibration and alignment procedures, essential to the initial understanding of the detector performance and to the extraction of the first physics results.

8 System Test and Cosmic Rays Operation

1550 A system test with one endcap (three disks) of the pixel detector has been performed as a realistic test of the detector operation. To achieve this goal, a setup containing about 10% of all detector services has been installed in the CERN SR1 facility. Production or pre-production parts were used to establish the realism of the test.

1555 The system test program included the commissioning of the setup and the detector readout, measurements of the analogue performance of the detector modules and data taking with cosmic rays. The following sections give a brief overview of the most important procedures and results of the system test [93].

8.1 Setup

1560 One endcap of the pixel detector has been operated in a system test setup. The endcap was connected to a prototype service quarter panel, as can be seen in the photography in Fig. 39, and cooled with evaporative C_3F_8 , as expected for final operations. All services connected to the endcap were made from production or pre-production parts to create a realistic copy of the final setup inside ATLAS.

The endcap was oriented vertically for data taking with cosmic rays. Several scintillators were used to generate the trigger. The scintillator arrangement, which is shown in Fig. 39, has been designed to maximise the number of triggers that have tracks passing through the three disks of the endcap and at same time allow also for inclined tracks.

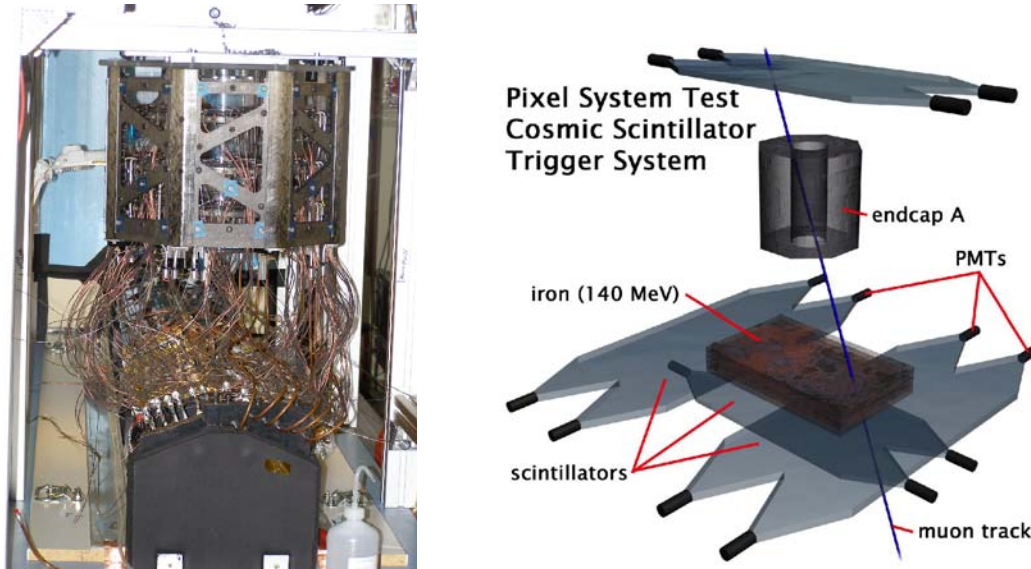


Figure 39: Photograph of the endcap in the system test setup, connected to the prototype service quarter panel, and schematic drawing of the scintillator setup for the cosmic trigger.

8.2 Commissioning of the Setup

8.2.1 Service Tests

As a first step in the commissioning of the setup, a complete test of the electrical services was performed. This was done using a dedicated test setup, which was designed to automatically test all electrical services belonging to one Patch Panel 0. This first application of the services test setup and procedures was essential to develop the final protocol used for services commissioning for the installed detector in ATLAS.

8.2.2 Cooling Operation

Evaporative C_3F_8 -cooling was used for the endcap as will be the case for the full pixel detector during operation in the ATLAS experiment. Temperature measurements at different supply voltages and module configurations were performed to simulate the evolving power consumption expected during the detector lifetime and to assess the cooling performance under these conditions. The module temperature for power off was about $-24^\circ C$ and about $-17^\circ C$ for nominal (non-irradiated) power values and about $-12^\circ C$ (extrapolated) for power values after irradiation to a lifetime dose.

8.2.3 Calibration of the Optical Links

For a reliable communication between the pixel detector modules and the off-detector electronics several parameters of the optical links (section 4.4) have to be calibrated. The algorithms for this tuning procedure were partially developed and refined during the system test as this was the first time a large

1585 number of these links were operated under realistic conditions. Whereas the setting of the parameters for
 the links from the off-detector electronics to the modules is not critical, the tuning of the returning-data
 links requires more care. The first parameter to be adjusted is the light output power of the VCSELs on
 the optoboards. This power is determined with a control current I_{Set} that is common for all VCSELs of
 one optoboard. The power can be measured by means of the current in the pin-diodes at the receiving
 1590 end. The control current has to be set such that all VCSELs of the optoboard are safely above the laser
 threshold.

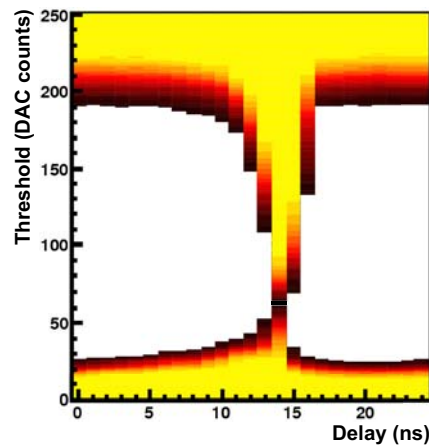


Figure 40: Scan of the receiver parameters for the optical data link. The horizontal axis gives the sampling phase, the vertical axis the sampling threshold. The colour encodes the number of errors for a given set of parameters (white corresponds to no errors in the given bit pattern).

For a given laser power, the threshold and the data delay at the receiving end need to be set. The first parameter determines the discrimination between a logical 0 and a logical 1, the second determines the sampling time within the clock cycle of the 40 MHz clock. Figure 40 shows a two-dimensional plot of the number of bit errors measured during a scan of these two parameters. The horizontal axis corresponds to the sampling time, the vertical axis to the sampling threshold. A region with errors at low thresholds can be seen, which is mainly given by bit flips from 0 to 1 due to a threshold setting near the noise floor, and a region with errors at high thresholds, which is given by bit flips from 1 to 0 due to a too high sampling threshold. The vertical error region is caused by a sampling time which is set on the clock edge where the data is not stable. The operating point of the receiver has to be set in the error free region taking into account that not all boundaries between error-free and error regions are equally stable. It has been found that the noise floor and the trailing edge of the signal are more stable than the upper signal level and the leading edge. The most reliable operating point is therefore not in the centre of the error-free region, but closer to the stable boundaries. A difficulty arises if the spread in the output power between the different lasers of one optoboard is too large. In this case it can be difficult to find a value for I_{Set} such that all channels show a sufficiently large error-free region from which a stable set of operating parameters is chosen. In the system test it was discovered that the power spread increases for lower optoboard temperatures. It was therefore decided to equip the optoboards in the detector with additional heaters to keep them at temperatures up to $\sim 20^{\circ}\text{C}$. [4]

1610 Furthermore, it was discovered during the system test that a few optoboards showed a slow turn-on behaviour, i.e. after turning on the lasers, the output power increased gradually over a time of several microseconds. This problem was addressed by thorough testing of production units, such that optoboards with this behaviour were excluded from the production service quarter panels(see section 4.4.5).

It was also discovered that some of the VCSELs on the opto-boards produced very little or no optical

1615 power on all channels. The optical power on one channel was found to depend on the current on other channels. This can be modeled with a common resistance. The voltage drop on the CSR results in inadequate voltage to drive the VCSELs. A procedure was formulated to estimate the CSR and opto-boards with high CSR in the VCSELs were excluded from the production service quarter panels, corresponding to 7production(also see section 4.4.5).

1620 8.3 Analogue Performance of the Modules

Several measurements of the analogue performance of all modules were performed during the system test. Table 15 shows the average values of threshold, threshold dispersion and noise for all tested modules in endcap A. The thresholds of all modules had been adjusted to $4000e^-$. Both threshold and noise values are comparable to single module measurements without any notable influence of the operation within
1625 a large scale system. Also we see a very good homogeneity between the measured thresholds of all modules, which is necessary for the reliable operation of a large scale pixel detector in the experiment.

Average threshold	$4002 \pm 1.3e^-$
Threshold dispersion	$33 \pm 1e^-$
Average noise	$166 \pm 8.5e^-$

Table 15: Values for threshold, threshold dispersion and noise for all tested modules on endcap A

8.4 Cosmic Ray Operation

The endcap detector was operated with an external trigger generated from a set of scintillators arranged above and below the endcap. The rate of cosmic ray tracks crossing all three disks of the endcap in the sensitive area was about 6 Hz. The detector noise was studied [94] using several runs with different
1630 detector configurations and it was found that the noise signal was uncorrelated with the timing relative to the trigger. Pixel occupancy, i.e. the fraction of pixel hits per readout event, was used to classify “hot” pixels. Pixels with an occupancy of 10^{-5} or greater were defined as “hot” pixels. Approximately 90% of these “hot” pixels were already identified as defective during module characterization. Their total
1635 fraction is below 0.2%. After removal of “hot” pixels, the noise occupancy drops from 10^{-7} to 10^{-10} , as shown in Fig. 41.

Data from cosmic ray operation were used to exercise the full chain of offline reconstruction. Digitization parameters were taken from the characterisation tests performed during module production. The simulation produced with these parameters has been found to be in a good agreement with the data,
1640 providing an important test of the ATLAS pixel detector simulation.

The tracking studies, especially related to tracks passing through the overlap regions between adjacent modules in the same disk, were useful in spotting problems in the detector’s geometrical description. The characteristics of pixel clustering in the data were checked and found to agree well with the Monte Carlo simulation as shown in Fig. 42.

The pixel hit efficiency was measured to be close to 100% by checking how often a pair of hits was found in the overlap region compared to expectations. Approximately 24% of tracks passed through the overlap region, and were used to estimate the relative alignment between adjacent modules with the residuals from overlap hits. Fig. 43 shows the resolution in the short pixel direction before and after the alignment correction. When using the nominal geometry, an initial resolution of $23 \mu m$ was obtained.
1645 After an alignment correction, this improves to $16 \mu m$, which is close to the $14 \mu m$ expected from the Monte Carlo simulation. The relative alignment constants were also crosschecked between the data and
1650

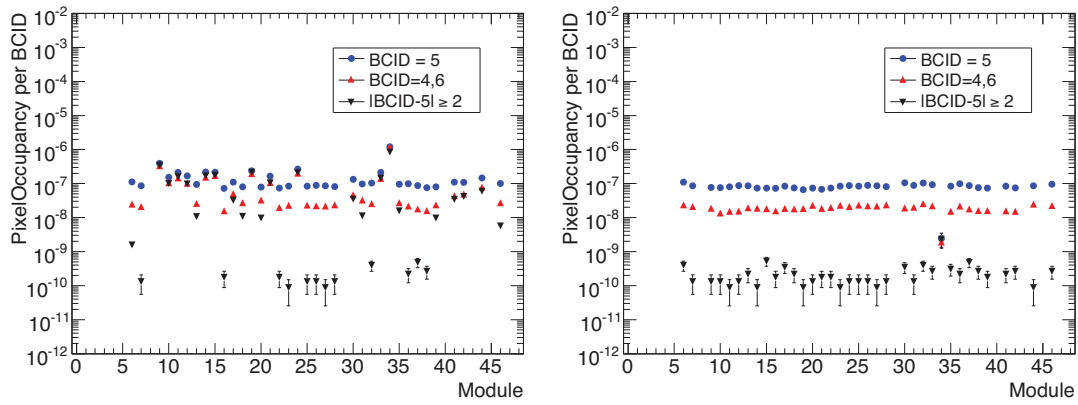


Figure 41: Occupancy per pixel in all modules of one pixel disk before (a) and after (b) masking off hot pixels for bunch crossings (BCID) within and outside the cosmic trigger (BCID=5).

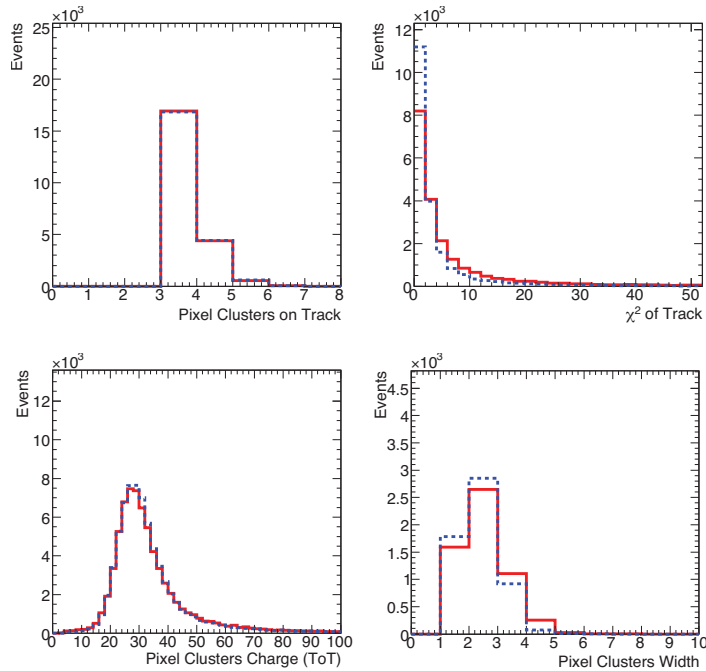


Figure 42: Comparison between cosmic ray data (histogram) and Monte Carlo (dashed) of the number of pixel hits (top left); the fitted track χ^2 (top right); the cluster charge of time over threshold (TOT) (bottom left) and the cluster width of the cosmic tracks (bottom right).

the survey obtained during the detector assembly for the modules with enough overlap hits (≥ 50) in the data. [4] A strong correlation between the two methods indicates that the survey is a reasonable starting point for the final detector alignment.

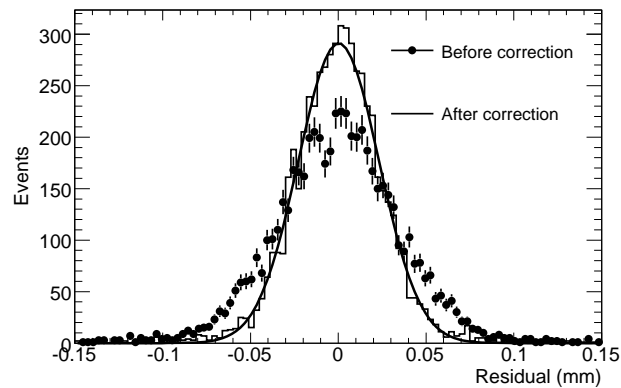


Figure 43: Distribution of overlap residuals before and after alignment corrections.

1655 9 Conclusion

The design and fabrication of the ATLAS pixel detector electronics, sensors and modules have been described in this paper. A brief description of the mechanics and electrical and cooling services has been given and more details on these elements of the pixel detector may be found in Ref. [4]. First operation of the pixel detector in ATLAS and with colliding beams from the Large Hadron Collider will be described in subsequent papers.

1660 10 Acknowledgements

The work described in this paper was supported by the following funding agencies: Czech Republic (Ministry of Industry and Trade, Ministry of Education, Youth and Sports), France, Germany (Federal Ministry of Education and Research, Strategic Research Cluster FSP101), Italy, Taiwan (National Science Council), United States of America (Department of Energy and the National Science Foundation).

We express our grateful appreciation to all students, technicians, workshops, drawing-offices and other support units of all institutes, who have been involved in the development and construction of this pixel detector. Without these many dozens of people, partly working for extended periods on this project, it would not have been possible to build the ATLAS pixel detector.

1670 We gratefully acknowledge the assistance of Dr. Piotr Zyla in the compilation of this paper.

References

- [1] ATLAS Collaboration, The ATLAS Experiment at the CERN Large Hadron Collider, JINST ???(2008) submitted to JINST.
- [2] ATLAS Collaboration, Inner Detector: Technical Design Report, CERN/LHCC/97-016/017(1997).
- 1675 [3] ATLAS Collaboration, Pixel Detector: Technical Design Report, CERN/LHCC/98-013(1998).

- [4] ATLAS Collaboration, The ATLAS Pixel Detector Mechanics and Services, JINST ???(2008) submitted to JINST.
- [5] S. Correard et al., ATLAS Note ATL-PHYS-2004-006 (2003).
- [6] D. Fasching, The ATLAS Pixel Detector, Nucl. Inst. Meth. **A408** (1998) 229–234.
- 1680 [7] CPPM. Unpublished.
- [8] L. Blanquart et al., Pixel Analog Cells Prototypes for ATLAS in DMILL Technology, Nucl. Inst. Meth. **A395**(1997) 313–317.
- [9] L. Blanquart, D. Calvet, and P. Fischer, MAREBO, a Full Radhard Pixel Detector Prototype for ATLAS, 4th Workshop on Electronics for LHC Experiments - LEB 1998, CERN/LHCC/98-036(1998).
- 1685 [10] L. Blanquart et al., Pixel Readout Electronics for LHC and Biomedical Applications, Nucl. Inst. Meth. **A439** (2000) 403–412.
- [11] K. Einsweiler et al., Dead-time Free Pixel Readout Architecture for ATLAS Front-end IC, IEEE Tr. Nucl. Sci **46**(1999) 166–170.
- 1690 [12] K. Einsweiler et al., On the Performance and Limitations of a Dual Threshold Discriminator Pixel Readout Circuit for LHC, IEEE Tr. Nucl. Sci **46**(1999) 792–799.
- [13] J. Richardson, The ATLAS Pixel Front-end Readout Chips, Nucl. Inst. Meth. **A473**(2001) 157–162.
- [14] L. Blanquart et al., Analog Front-end Cell Designed in a Commercial 0.25 μm Process for the ATLAS Pixel Detector at LHC, IEEE Tr. Nucl. Sci **49**(2002) 1778–1782.
- 1695 [15] L. Blanquart et al., FE-I2: A Front-end Readout Chip Designed in a Commercial 0.25 μm Process for the ATLAS Pixel Detector at LHC, IEEE Tr. Nucl. Sci **51** (2004) 1358–1364.
- [16] I. Peric Design and Realisation of Integrated Circuits for the Readout of Pixel Sensors in High-Energy Physics and Biomedical Imaging, PhD thesis, BONN-IR-2004-13, Bonn University(2004).
- [17] I. Peric et al., The FE-I3 Readout Chip for the ATLAS Pixel Detector, Nucl. Inst. Meth. **A565** (2006) 178–187.
- 1700 [18] J. Grosse-Knetter, The ATLAS Pixel Detector, Nucl. Inst. Meth. **A568** (2006)252–257.
- [19] F. Hugging, The ATLAS Pixel Detector. IEEE Tr. Nucl. Sci **53** (2006) 1732–1736.
- [20] R. Beccherle et al., MCC: The Module Controller Chip for the ATLAS Pixel Detector, Nucl. Inst. Meth. **A49** (2002) 117–133.
- 1705 [21] M. L. Chu et al., The Off-detector Opto-electronics for the Optical Links of the ATLAS Semiconductor Tracker and Pixel Detector, Nucl. Inst. Meth. **A530** (2004) 293–310.
- [22] K. E. Arms et al., ATLAS Pixel Opto-electronics, Nucl. Inst. Meth. **A554** (2005) 458–468.
- [23] I. –M. Gregor, Optolinks for The Atlas Pixel Detector, PhD thesis, WUB DIS 2001-03, University of Wuppertal (2001).
- 1710 [24] W. Fernando, Overview and Status of ATLAS Pixel Detector, 8th International Conference on Large Scale Applications and Radiation Hardness of Semiconductor Detectors (RD07)(2007).

- [25] G. Mahout et al., Irradiation Studies of Multimode Optical Fibres for use in ATLAS Front-end Links, *Nucl. Inst. Meth.* **A446** (2000) 426–434.
- [26] K. K. Gan et al., Optical Link of the ATLAS Pixel Detector, *Nucl. Inst. and Meth.* **A570** (2007) 292–294.
- [27] S. Nderitu, Atlas Pixel Opto-Board Production and Optolink Simulation Studies, PhD thesis, WUB-DIS 2007-03, University of Wuppertal (2007).
- [28] T. Flick et al., Optical Readout in a Multi-module System Test for the ATLAS Pixel Detector, *Nucl. Inst. Meth.* **A565** (2006) 85–89.
- [29] T. Flick, P Gerlach, K Reeves, and P Mättig, Atlas Pixel Detector Timing Optimisation with the Back-of-crate Card of the Optical Pixel Readout System, *JINST* **2** (2007) P04003.
- [30] ATLAS Collaboration, High-Level Trigger, Data-Acquisition and Controls Technical Design Report, CERN/LHCC/03-022(2003).
- [31] J. Vermeulen et al., Atlas Dataflow: the Read-out Subsystem, Results from Trigger and Data-Acquisition System Testbed Studies and from Modeling, *IEEE Tr. Nucl. Sci* **53** (2006) 912–917.
- [32] T. Vickey, A Read-out Driver for Silicon Detectors in ATLAS, 12th Workshop on Electronics for LHC and Future Experiments - LECC(2006).
- [33] J. Butterworth et al., Timing, Trigger and Control Interface Module for ATLAS SCT Read Out Electronics, ATLAS Note ATL-INDET-99-018(1999).
- [34] M. Postranecky et al., TIM (TTC Interface Module) for ATLAS SCT & Pixel Read Out Electronics, Proceedings of the Seventh Workshop on Electronics for LHC Experiments - LEB 2001, CERN/LHCC/2001/034(2001).
- [35] M. Warren et al., TTC Interface Module for ATLAS Read Out Electronics: Final Production Version Bbased on Xilinx FPGA Devices, Proceedings of the Tenth Workshop on Electronics for LHC and Future Experiments, Boston, USA(2004)320.
- [36] M. Joos, The VMEbus Processor Hardware and Software Infrastructure in ATLAS., Proceedings of the Eleventh Workshop on Electronics for LHC and Future Experiments - LECC 2005, Heidelberg, Germany,(2005) 331.
- [37] J. Schultes et al., The Power Supply System for the ATLAS Pixel Detector, *IEEE Nucl. Sci. Symposium Conference Record* **3** (2004) 1711–1715.
- [38] T. Henss et al., The Hardware of the ATLAS Pixel Detector Control System, *JINST* **2** (2007) P05006–P05006.
- [39] M. Imhauser et al., The Control System for the ATLAS Pixel Detector, *IEEE Tr. Nucl. Sci* **51** (2004) 502–507.
- [40] C. Bayer et al., Studies for a Detector Control System for the ATLAS Pixel Detector, Proceedings of the Seventh Workshop on Electronics for LHC Experiments - LEB,CERN/LHCC/2001/034 (2001) 396.
- [41] H. Boterenbrood and B. I. Hallgren. The Development of Embedded Local Monitor Board (ELMB). Proceedings of the Ninth Workshop on Electronics for LHC Experiments - LECC 2003,CERN/LHCC/03-055(2003) 331.

- [42] S. Schmeling, Common Tools for Large Experiment Controls—a Common Approach for Deployment, Maintenance, and Support, *IEEE Tr. Nucl. Sci* **53** (2006) 970–973.
- [43] J. Schultes et al., Validation Studies of the ATLAS Pixel Detector Control System, *Nucl. Inst. Meth.* **A565** (2006) 90–96.
- 1755 [44] M. Imhauser et al., First Experiences with the ATLAS Pixel Detector Control System at the Combined Test Beam 2004, *Nucl. Inst. Meth.* **A565** (2006) 97–101.
- [45] G. Lindström et al., Radiation Hard Silicon Detectors Developments by the RD48 (ROSE) Collaboration, *Nucl. Inst. Meth. /bf A466* (2001) 308–326.
- [46] F. Lemeilleur, G. Lindström, and S. Watts, Third RD48 status report (2000) CERN/LHCC/00-009.
- 1760 [47] G. Lindström et al., Developments for Radiation Hard Silicon Detectors by Defect Engineering — Results by the CERN RD48 (ROSE) Collaboration, *Nucl. Instr. Meth.* **A465** (2001) 60–69.
- [48] R. Wunstorf, Radiation Tolerant Sensors for the ATLAS Pixel Detector, *Nucl. Inst. Meth. /bf A466* (2001) 327–334.
- [49] A. Bischoff et al., Breakdown Protection and Long Term Stabilisation for Si detectors, *Nucl. Inst. Meth.* **A326** (1993) 27–37.
- 1765 [50] M. S. Alam et al., The ATLAS Silicon Pixel Sensors, *Nucl. Inst. Meth.* **A456** (2001) 217–232.
- [51] R. H. Richter et al., Strip Detector Design for ATLAS and HERA-B using Two-dimensional Device Simulation, *Nucl. Instr. Meth.* **A377** (1996) 412–421.
- [52] J. Wüstenfeld, Characterisation of Ionisation-induced Surface Effects for the Optimisation of Silicon-Detectors for Particle Physics Applications, PhD thesis, University of Dortmund (2001).
- 1770 [53] I. Gorelov et al., Electrical Characteristics of Silicon Pixel Detectors, *Nucl. Inst. Meth.* **A489** (2002) 202–217.
- [54] J. Matheson et al., Radiation Damage Studies of Field Plate and p-stop n-side Silicon Microstrip Detectors, *Nucl. Inst. Meth.* **A362** (1995) 297–314.
- 1775 [55] J. M. Klaiber-Lodewigs, Pixel Sensor Quality Assurance Plan, ATLAS Note ATL-IP-QA-0001(2004).
- [56] T. Lari, Measurement of Trapping Time Constants in Irradiated DOFZ Silicon with Test Beam Data, *Nucl. Inst. Meth.* **A518** (2004) 349–351.
- [57] O. Krasel et al., Measurement of Trapping Time Constants in Proton-irradiated Silicon Pad Detectors, *IEEE Tr. Nucl. Sci* **51** (2004) 3055–3062.
- 1780 [58] R. Klingenberg et al., Prediction of Charge Collection Efficiency in Hadron-Irradiated Pad and Pixel Silicon Detectors, *Nucl. Inst. Meth.* **A568** (2006) 34–40.
- [59] C. Troncon, Radiation Hardness Performance of ATLAS Pixel Tracker, *Nucl. Inst. Meth.* **A530** (2004) 65–70.
- 1785 [60] J. M. Klaiber-Lodewigs, Evaluation of Testing Strategies for the Radiation Tolerant ATLAS n+-in-n Pixel Sensor, *Nucl. Inst. Meth.* **A512** (2003) 332–340.

- [61] J. M. Klaiber-Lodewigs, The ATLAS Pixel Sensor — Properties, Characterization and Quality Control, PhD thesis, University of Dortmund(2005).
- [62] L. Rossi, Pixel Detectors Hybridisation, Nucl. Inst. Meth. **A501** (2003) 239–244.
- 1790 [63] O. Ehrmann et al., A Bumping Technology for Reduced Pitch, Proceedings of the Second International TAB Symposium, San Jose, USA (1990) 41–48.
- [64] J. Wolf, PbSn60 Solder Bumping by Electroplating, Pixel 2000 Conference, Genova, Italy (2000) – <http://www.ge.infn.it/Pix2000/slides.html>.
- 1795 [65] J. Wolf, G. Chmiel, and H. Reichl, Lead/Tin (95/5 %) Solder Bumps for Flip Chip Applications Based on Ti:W(N)/Au/Cu Underbump Metallization, Proceedings of the Fifth International TAB/Advanced Packaging Symposium ITAP, San Jose, USA (1993) 141–152.
- [66] A.M. Fiorello, ATLAS Bump Bonding Process, Proceedings of the Pixel 2000 Conference, Genoa, Italy (2000).
- [67] T. Fritzsche et al., Experience in Fabrication of Multichip-modules for the ATLAS Pixel Detector, 1800 Nucl. Inst. Meth. **A565** (2006) 309–313.
- [68] G.L. Alimonti et al., Analysis of the Production of ATLAS Indium Bonded Pixel Modules, Nucl. Inst. Meth. **A565** (2006) 296–302.
- [69] G.L. Alimonti et al., Reworking of Indium Bump Bonded Pixel Detectors. Pixel 2002 Conference, Carmel, USA (2002).
- 1805 [70] L. Rossi, P. Fischer, T. Rohe, and N. Wermes, Pixel Detectors: From Fundamentals to Applications, Berlin, Heidelberg : Springer (2006).
- [71] C. Gemme, Production of the ATLAS Pixel Detector Modules, Nucl. Inst. Meth. **A560** (2006) 71–74.
- [72] J. Grosse-Knetter et al., Experience with Module Production and System Tests for the ATLAS Pixel 1810 Detector, Nucl. Inst. Meth **A565** (2006) 79–84.
- [73] I. Gorelov et al., Nucl. Inst. Meth. **A481** (2002) 204.
- [74] C. Troncon, IEEE Tr. Nucl. Sci **47** (2000) 737.
- [75] F. Ragusa, Nucl. Inst. and Meth. **A447** (2000) 184.
- [76] T. Lari, PHD Thesis, University of Milano, (2001).
- 1815 [77] A. Andreazza, Nucl. Inst. Meth. **A535** (2004) 357.
- [78] G. Alimonti et al., A Study of Charge Trapping in Irradiated Silicon with Test Beam Data, ATLAS Note ATL-INDET-2003-014 (2003).
- [79] G. Alimonti et al., Analysis of Testbeam Data of ATLAS Pixel Detector Modules with a High Intensity Pion Beam, ATL-INDET-INT-2005-006, ATL-COM-INDET-2005-012.
- 1820 [80] G. Alimonti et al., Test-beam Measurement of the Detection Efficiency of ATLAS Pixel Production Modules, ATL-INDET-INT-2005-007, ATL-COM-INDET-2005-013.
- [81] A. Matera, CERN-THESIS-2008-025, Thesis, University of Milano, (2005).

- [82] A. Arelli Maffioli, CERN-THESIS-2008-024, Thesis, University of Milano, (2007).
- [83] J. Treis et al., Nucl. Instr. and Meth. **A490** (2002) 112.
- 1825 [84] A. Andreazza et al., H8 ATLAS Pixel Test Beam Analysis Program - User Guide, ATLAS Note ATL-INDET-2003-009(2003).
- [85] E. Belau et al., Nucl. Inst. Meth. **A214** (1983) 253.
- [86] T. Lari, Lorentz Angle Variation with Electric Field for ATLAS Silicon Detectors, ATLAS Note ATL-INDET-2001-004(2001).
- 1830 [87] T. Lari, A GEANT4 Simulation of Not-Irradiated and Irradiated Pixel Detectors ATLAS Note ATL-INDET-2003-015(2003).
- [88] S. Agostinelli et al., Nucl. Inst. Meth. **A506** (2003) 250.
- [89] C. Jacoponi et al., Solid State Electronics **20** (1977) 77.
- [90] V. Radeka, Ann. Rev. Nucl. Part. Sci. **38** (1988) 217.
- 1835 [91] ATLAS Pixel and SCT Collaboration, Alignment of the Pixel and SCT Modules for the 2004 ATLAS Combined Test Beam, ATLAS Note ATL-INDET-PUB-2007-014(2007) and ATL-COM-INDET-2007-019(2007).
- [92] ATLAS Pixel Collaboration, Requirements for the Pixel Detector Services, ATLAS Note ATL-IP-ES-0007(2004).
- 1840 [93] D. Dobos, Commissioning Perspectives for the ATLAS Pixel Detector, PhD thesis, University of Dortmund(2007).
- [94] ATLAS Pixel Collaboration, Pixel Offline Analysis for EndcapA Cosmic Data, ATLAS Note ATL-INDET-PUB-2008-001(2008) and ATL-COM-INDET-2007-018(2007).